Study of Hadron Production in Au+Au Collisions at 10.9 A GeV/c with a new Forward-Angle Spectrometer

Kenta Shigaki

Department of Physics, School of Science
Graduate School
University of Tokyo
7-3-1 Hongo, Bunkyo-ku, Tokyo 113, JAPAN

Doctor Thesis

Submitted in December, 1994
Accepted in February, 1995

Abstract

A new ground is being opened up for relativistic heavy-ion physics, owing to the successful acceleration of the ^{197}Au beam at the Alternating Gradient Synchrotron (AGS) at Brookhaven National Laboratory. Aiming at extending studies of hadron production in relativistic heavy-ion collisions systematically to heavier collision systems with the Au beam, with which more exotic quark-oriented phenomena could be expected to be observed, we have constructed a new forward-angle spectrometer for operation under a high particle-density condition. The first data with the new spectrometer were taken in October, 1993.

With the new spectrometer, production of various hadrons were studied for ^{197}Au+^{197}Au collisions at 11 A GeV/c, with event characterization selecting the centrality of the collisions. Identified single particle spectra were measured and analyzed for charged pions ($\pi^{\pm}$), positively charged kaons (K^{+}), and protons, covering the mid-rapidity region for all these particle species. Measurement of proton spectra in the mid-rapidity region was performed for the first time with the Au beam at the AGS energy.

Experimental results are presented on transverse-mass spectra and rapidity distributions of $\pi^{\pm}$, K^{+}, and protons in Au+Au collisions with a centrality cut. The rapidity distribution of protons in central Au+Au collisions displays a single peak structure around the center of mass. Besides, the proton spectra are deviated from the well-known single-exponential scaling, showing a convex shape.

The dynamics of relativistic heavy-ion collisions are discussed through comparisons of Au+Au collisions with lighter collision systems, and utilizing microscopic cascade models and a hydro-dynamical collective-flow model. Outlines of hadron production is consistent with the cascade picture. The highest baryon density achieved in the collision system is estimated grounded on the cascade models to be 7 – 8 times higher than the normal nucleus density. On the other hand, the slopes of the particle spectra and their shapes in the mid-rapidity region are better described in the hydro-dynamical model, suggesting the importance of radial expansion of the system in the collision dynamics. A collective effect beyond a simple cascade with multiple scattering is implied to exist in the mid-rapidity region of the massive collision system.

Contents

List of Figures

List of Tables

Chapter 1

Introduction

1.1 Relativistic Heavy-Ion Experiment

More than twenty years have passed since relativistic heavy-ion collisions first attracted attention of physicists, as a way to study the nature of a state of matter with high baryon and/or energy densities. According to lattice calculations of the Quantum Chromo Dynamics (QCD) [1] and by analogy with solid state systems, a phase transition is expected to occur from a normal hadronic phase to a new state of matter if the baryon and/or energy densities of matter reach high enough. The new state is called a quark-gluon plasma phase, since quarks and gluons are expected to be deconfined, forming a weakly interacting system [2, 3]. Though it must have existed in the very early universe, relativistic heavy-ion collisions are currently the only possible candidate by which we can reproduce such an extreme condition in a relatively large space-time volume [4, 5].

Following researches using the Bevalac, which was started in 1974 at Lawrence Berkeley Laboratory, experimental studies have been intensively carried out since 1986, in use of the Alternating Gradient Synchrotron (AGS) at Brookhaven National Laboratory (BNL) and the Super Proton Synchrotron (SPS) at CERN, as well as theoretical approaches to the subject. Utilizing the beams up to ^{32}S, some experiments have suggested possible signatures of a quark-gluon plasma phase, such as enhanced production of strange particles [6, 7, 8, 9] including multi-strange baryons and anti-baryons [10], suppression of J/Ψ production [11], and extremely large source size of particle emission [12]. Other proposed signatures include direct photons and lepton pairs from the early stage of the collisions [13].

Mass shift of vector mesons such as ϕ, ω, and ρ has also been proposed as a signature of the chiral symmetry restoration [14, 15]. It should be stated, however, no definite evidence of such a phase transition has been found so far [16, 17].

Nonetheless, the hope is that we have been approaching closer to formation of a quark-gluon plasma phase, or at least to a state of matter where the degrees of freedom of quarks and gluons play more important roles for the observables. The AGS has started acceleration of a ^{197}Au beam at 11 – 12 A GeV/c* since 1992; the SPS also started acceleration of ^{208}Pb at 160 A GeV/c in 1994. With those heavy-ion beams, microscopic cascade calculations of nucleus-nucleus collisions predict baryon densities 5 – 10 times higher than that of normal nucleus to be achieved in the collisions [18, 19]. The models based on hadronic interactions and/or color strings deserve to be respected to a certain degree, because of their successful description of experimental results with the lighter beams [20, 21, 22, 23]. Furthermore, heavy-ion colliders are being planned and constructed aiming at experiments at higher energies, looking for formation of a baryon-free quark-gluon plasma phase with a higher energy density [24].

To observe a quark behavior in the collision systems, proceeding investigation and understanding of the hadron behaviors are required. The production mechanisms of hadrons have to be systematically studied before discussions on candidates of quark-oriented phenomena. In consideration of where the field is and where it is going, systematic studies of hadron production are essential in order to understand what really happens in relativistic heavy-ion collisions, even if reproduction of a quark-gluon plasma phase needs to wait for the next-generation colliders to come on-stage.

An advantage of A+A (or A+B) collisions over p+A collision experiments is selectivity of *central* (head-on) collision events. In the sense of searching for a quark-gluon plasma phase, most participant nucleons in central collisions suffer multiple collisions, and the system is thus expected to approach thermal equilibrium which is required for formation of the new phase in a large space-time volume. Also for studies of hadron production, selectivity of the centrality allows us to investigate the stopping or slowing down process of incident beam nucleons, which is an important factor to determine the baryon density achieved in the

*We use the notation of p A GeV/c in this thesis, to express a nucleus or an ion with the mass number A accelerated to p GeV/c of momentum per nucleon.

system. From this point of view, it has an importance for relativistic heavy-ion physics to proceed to heavier collision systems.

1.2 The AGS-E866 Experiment

In this section, physics goals of the AGS-E866 experiment and the motivation to construct a new forward-angle spectrometer are reviewed.

1.2.1 Motivation

As mentioned in Section 1.1, advanced heavy-ion accelerators are opening up a new ground for relativistic heavy-ion physics. At BNL, a new booster ring has been constructed to inject heavier ion beams to the AGS, and started its operation in 1992. Equipped with the booster, the AGS made the ^{197}Au beam at 11 – 12 A GeV/c available as a pioneer of a new era.

In the era of relativistic ion beams with intermediate mass, *e.g.* ^{28}Si, the AGS-E802/859 experiments at BNL, an American-Japanese collaboration, had been one of the major experiments in the society, presenting systematic data of inclusive and semi-inclusive hadron production [7, 25, 26, 27, 28], transverse-energy emission, [29, 30, 31], two-particle correlation, [32], and collective effects [33, 34] in use of a large aperture single-arm magnetic spectrometer, called the Henry Higgins [35, 36]. Seizing the opportunity of entering the first stage of the new era, we have proposed a new experiment using the ^{197}Au beam, as a next step succeeding the physics goals and ideas of the E802/859 experiments [37].

1.2.2 Physics Goals

The AGS-E866 experiment primarily aims at systematic studies of semi-inclusive spectra of various identified hadrons in conjunction with event characterization. What the E802/859 experiments have carried out using the lighter beams, *i.e.* from protons up to ^{28}Si, is extended by this experiment to heavier collision systems, *e.g.* ^{197}Au+^{197}Au, to provide a systematic view of heavy-ion collisions at the AGS energy of $\sim$ 10 A GeV/c. The general goals of the experiment can be itemized as follows:

1. To measure semi-inclusive spectra of various hadrons emitted from the collision systems, as a function of rapidity and transverse momentum over wide kinematic ranges.

2. To find dependence of these cross sections on the centrality of the collisions.

3. To look for systematic variations of the cross sections across a wide range of beams and targets, so as to investigate the collision dynamics and the mechanisms of particle production.

4. To measure two-particle correlations as a probe of the space-time structure of the collision systems.

5. To seek evidences for formation of a state of matter with high baryon and/or energy densities, and ultimately of a quark-gluon plasma phase.

Let us summarize here what would be gained by proceeding to an experiment with the ^{197}Au beam. It has been observed that the ^{28}Si beam is completely stopped by a sufficiently thick nuclear target such as lead, through measurements of protons in the beam rapidity region [38]. If a target, *e.g.* gold, is thick enough to stop the ^{197}Au beam also, the energy available to heat and compress the system may be expected to increase as the mass of the beam particle. As well as the energy and baryon densities in the central region of the collision system, the volume with a high local energy density, *e.g.* larger than 1 GeV/fm^3, has been predicted to increase by a factor of $2-3$ by a cascade model calculation for central Au+Au collisions over Si+Au [18, 23, 39]. Reflecting the increased size of the collision system and the resulting longer pass-by time, the effective interaction time may also increase and the system may approach thermal equilibrium. The expected enhanced baryon and/or energy densities and space-time volume of the interaction can be much improved conditions for formation of the exotic state of matter with apparent degrees of freedom of quarks and gluons, or even of a quark-gluon plasma phase.

As discussed in Section 1.1, experiments with relativistic heavy-ion beams have found several effects of nuclear matter uniquely associated with heavy-ion reactions. Remaining to be seen is whether they are simply due to the medium effects such as rescattering of secondary hadrons or are manifestations of more exotic effects. In any case, it is important to investigate how the effects develop

with increasing size of the collision system and the total available energy. A goal of the E866 experiment is to ascertain whether the trend from p+A collisions to ^{28}Si-induced reactions continues all the way to reactions with the ^{197}Au beam or saturation is reached, by extending studies of hadron production in heavy-ion collisions in a consistent and systematic way.

1.2.3 Two-Arm Spectrometer System

Proceeding to experiments with heavier ion beams, there comes a lot of experimental and technical difficulties. For the E866 experiment, stepping forward to the ^{197}Au beam from lighter ones up to ^{28}Si, one of the major difficulties has been how to deal with the much higher spatial density of the produced particles compared to that we had been handling. Shown in Figure 1.2.1 are the charged particle densities per solid angle expected based on a string model (FRITIOF [40]) for central collisions of Si+Au at 14.5 A GeV/c and for central Au+Au at 11.5 A GeV/c, as a function of angle in the laboratory frame with respect to the incident beam direction [37]. As seen in the figure, the particle density has been predicted to be about four times higher with the latter collision system.

On the other hand, it has turned out that the E802/859 Henry Higgins spectrometer cannot be operated properly at more forward angles than $\sim$ 7 degrees even with the ^{28}Si beam, since the high particle multiplicity and many background hits in the tracking chambers make it difficult to confidently reconstruct the tracks. Without major improvement of its performance, one can accordingly expect the spectrometer to cover only a region more backward than $\sim$ 20 degrees with the ^{197}Au beam (see Figure 1.2.1). In that case, the kinematic space covered with the spectrometer would be tightly restricted. Figure 1.2.2 shows with the solid lines the expected coverage of the Henry Higgins spectrometer in the rapidity and transverse-momentum space for pions, kaons, and protons, in an experiment with the ^{197}Au beam. With a symmetric collision system such as Au+Au, a particle spectrum taken at a given rapidity y in the center-of-mass frame is the same as taken at a rapidity $-y$; the regions covered with the kinematic reflection are also shown in the same figure with the broken lines.

Directly from the figure, it can be concluded that the Henry Higgins spectrometer cannot provide us with a sufficient kinematic coverage by itself; as far as pions are concerned, particles with transverse momenta larger than 300 MeV/c

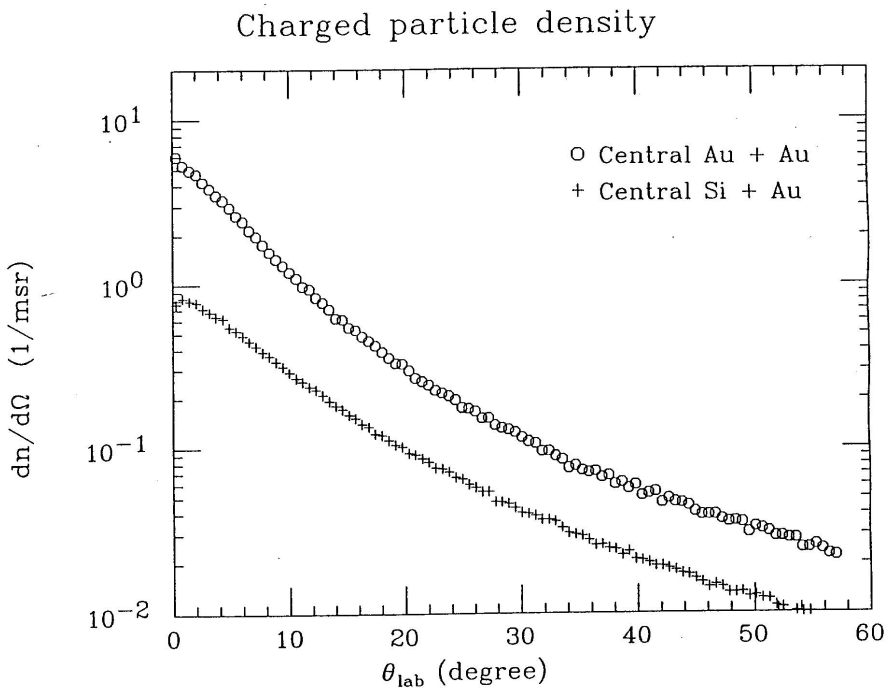

Figure 1.2.1: Spatial densities of produces charged particles expected by a string model [37]; for central Si+Au collisions at 14.5 A GeV/c (crosses) and for central Au+Au at 11.5 A GeV/c (circles).

can be observed at the mid-rapidity, but the lower limit is as high as 1 GeV/c for kaons and no proton data at all are available around the center of mass. Considering the physics goals, it is thus clear that we cannot help losing much information from the mid-rapidity region, in which we are very interested at the AGS energy, without covering the more forward angles. We have accordingly planned and constructed a new forward-angle spectrometer for operation under a high particle-density condition, which aims at covering the forward angles down to 6 degrees in the laboratory frame. The kinematic coverage of the Forward Spectrometer is shown in Figure 1.2.2 with dotted broken lines, and its reflection with dotted lines. A schematic view of the two-arm spectrometer system of the E866 experiment is shown in Figure 1.2.3; detailed descriptions of the experimental devices are given in Chapter 2. A wide coverage in the kinematic space, which is essentially important for systematic studies of particle production, is achieved by linking the regions covered with the two spectrometer arms.

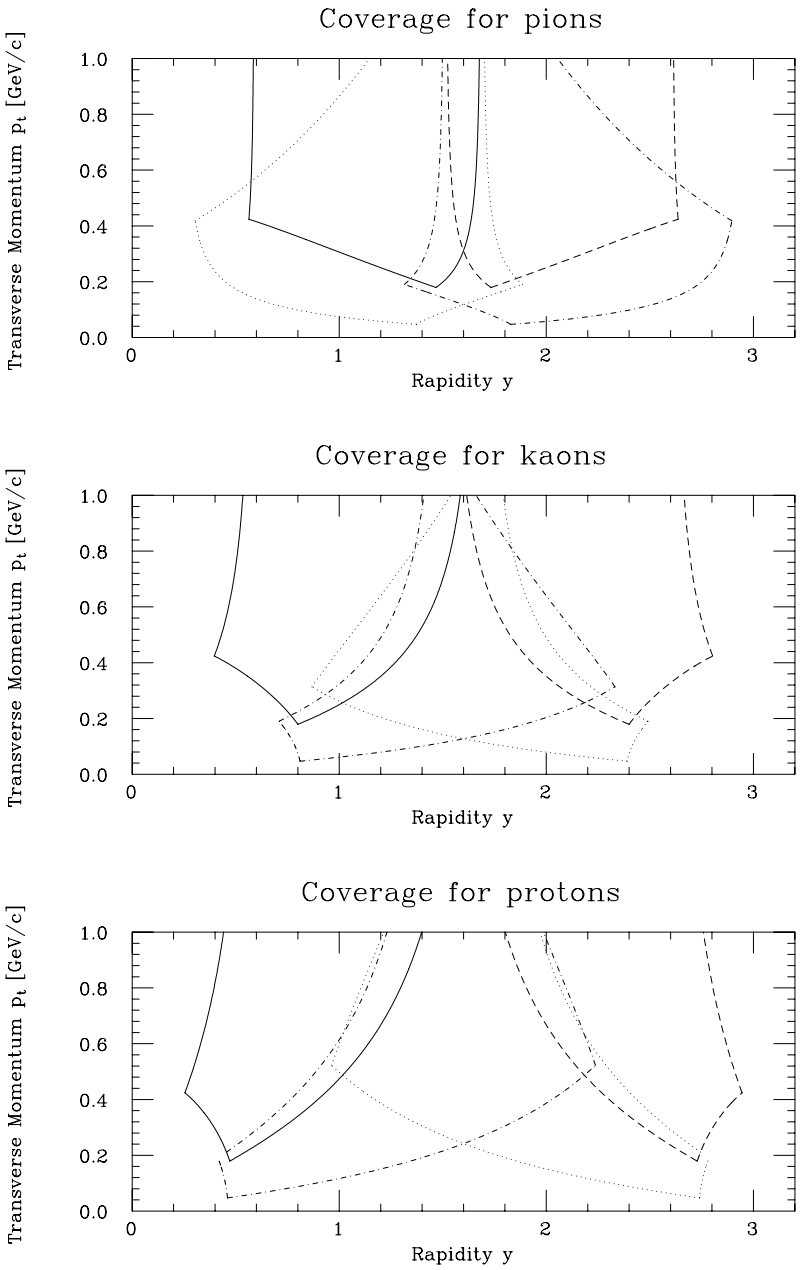

Figure 1.2.2: The coverages in the rapidity and transverse-momentum space of the two arms of the spectrometer; for pions (top), kaons (middle), and protons (bottom). Solid lines: the Henry Higgins spectrometer. Broken lines: the kinematic reflection of the coverage of the Henry Higgins spectrometer. Dotted broken lines: the Forward Spectrometer. Dotted lines: the kinematic reflection of the coverage of the Forward Spectrometer.

Figure 1.2.3: A schematic view of the experimental setup of the AGS-E866 experiment. The spectrometer arm shown in the lower half of the figure is the Forward Spectrometer, and the upper one is the Henry Higgins. For descriptions of the devices, see Chapter 2.

1.3 Thesis Objectives

The author has taken part in the E866 experiment, especially in the Forward Spectrometer project. His main contribution on the hardware were design work and construction of time projection chambers, the main tracking devices of the Forward Spectrometer arm (see Section 2.5). Two time projection chambers were developed and constructed in Japan*, and were shipped to the United States and installed in the Forward Spectrometer in 1993. The author was also involved in development of the analysis software for the spectrometer system. His main contribution was development of track reconstruction and particle identification codes, as well as organizing the group efforts, geometry adjustment of the tracking chambers, and calibration of the time projection chambers.

In this thesis, we present the first results from the E866 Forward Spectrometer. The measurement performed with the new spectrometer in 1993 kinematically covered the mid-rapidity region for protons, as well as for lighter particles such as pions and kaons. Event characterization was performed utilizing the forward (zero-degree) calorimeter. Particle spectra are shown for selected centrality, of charged pions, positively charged kaons, and protons.

Based on the experimental results, we try to investigate the mechanisms of relativistic heavy-ion collisions, comparing the data with those from lighter collision systems and calculations of microscopic cascade models, and utilizing a hydro-dynamical collective-flow model. A particular interest is in the spectra of protons in the mid-rapidity region, which were measured for the first time with such massive collision systems as Au+Au at the AGS energy. The nuclear stopping power is discussed based on the rapidity distribution of protons, and an estimate of the highest baryon density achieved in the collision system is given grounded on the cascade models. Also discussed are the shape of the proton spectra and the slopes of the spectra of various hadrons, which may be associated with collective effects in the massive collision system. Finally, we present a possible picture to describe Au+Au collisions at the AGS energy.

*The chambers were developed by a joint group of the Department of Physics, the University of Tokyo, Institute for Nuclear Study, the University of Tokyo, and the University of Tsukuba.

Chapter 2

Experimental Setup

2.1 Overview

The experimental setup of the AGS-E866 experiment, whose schematic view is shown in Figure 1.2.3, is presented in this chapter. A survey of the accelerator facility is first given in Section 2.2. In the following sections, each subsystem of the experiment is described; Section 2.3 is on the target arrangement, and Section 2.4 is on the trigger devices. A particular stress is placed upon the Forward Spectrometer, the most important subsystem for the analysis in this thesis. The detector components in the spectrometer are described in Section 2.5, as well as its conceptual design. The other arm of the spectrometer is only briefly introduced in Section 2.6, since it was not used in the analysis though results from the spectrometer were utilized for discussions. Section 2.7 describes an event characterization device, which was used to define the centrality of the collisions. Finally, Section 2.8 gives an account of the data acquisition system.

2.2 Accelerator Facility

The experiment was performed at the Tandem-Booster-AGS accelerator complex at Brookhaven National Laboratory [41, 42]. Figure 2.2.1 shows the layout of the heavy-ion accelerator facility [24]. Ions of ^{197}Au were first accelerated in the Tandem Van de Graaff accelerator up to 1.00 MeV per nucleon with a charge state of 13+. The ions were then transferred to the booster ring and were accelerated up to 192 MeV per nucleon with a charge state of 33+. The AGS brought up

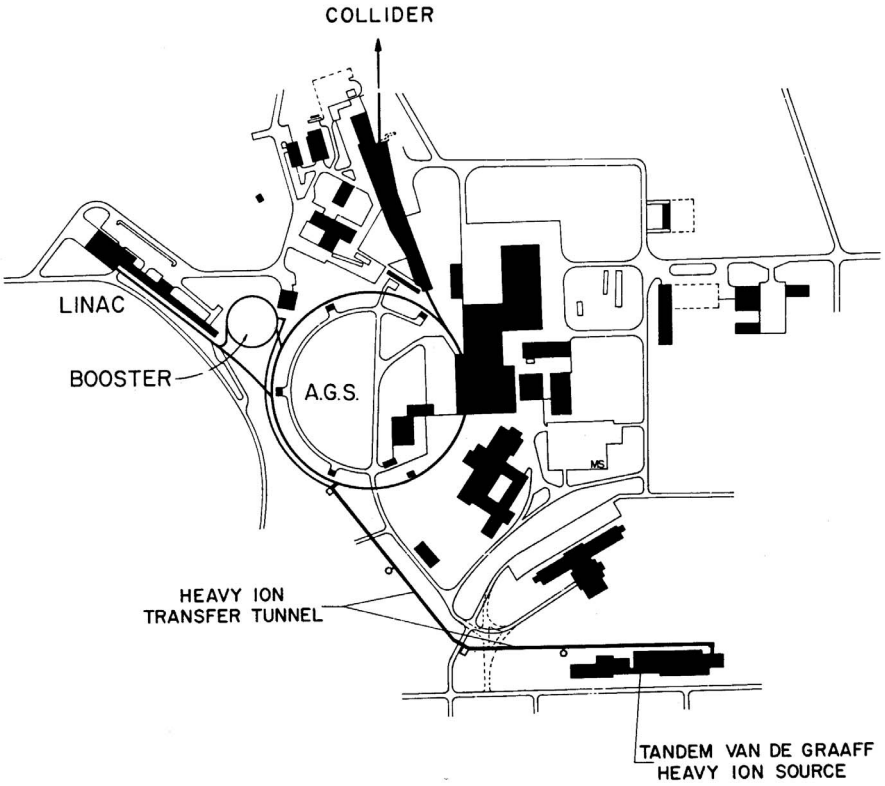

Figure 2.2.1: The heavy-ion accelerator facility at Brookhaven National Laboratory [24].

the beam to its final momentum of 11.1 A GeV/c in the form of $^{197}Au^{77+}$ ions, *i.e.* with two remaining electrons. The slow-extracted primary heavy-ion beam was fully stripped and was lead to the B1 beam line which our experimental apparatus sat on. At the experimental area, the beam momentum was slightly below 11 A GeV/c*. Typical beam intensity on the target was $3 - 7 \times 10^4$ particles per spill; the beam had a repetition cycle of ~ 4 sec, and a flat top of ~ 1 sec per spill.

2.3 Target Arrangement

The target assembly was made of aluminum and was connected with the beam pipe which stretched about 11 m long downstream of the target. The entire vessel

*The AGS-E877 group measured the beam momentum at their experimental area in 1993 runs, and got a result of 10.78±0.03 A GeV/c [43].

was kept in vacuum to restrain the Au beam from interactions with air. Up to six different targets could be held in the assembly, and they were placed on or retracted out of the beam by a remote control system. The target of ^{197}Au (see Section 3.2 for its specifications) was mounted in one of the six target holders; another holder was always kept open and was used as an empty target to study the background contribution as described in Section 5.2.

2.4 Trigger Devices

Two trigger devices are introduced in this section. One is beam counters placed upstream of the target to define the incoming beam particles, and the other is a counter to detect interactions by means of charge measurement of the beam particles downstream of the target.

2.4.1 Beam Counter System

A couple of beamline counters were used to count the beam particles and to veto the beam halo. The beam was defined with a Čerenkov counter, called BTOT, with a quartz radiator of 51 mm high, 76 mm wide, and 200 μm thick. It was placed 171 cm upstream of the target, and was read out with two 2-inch photo-multiplier tubes of Hamamatsu model R2083 on its both sides, through quartz windows of the vessel for the vacuum. A scintillation counter was placed at 145 cm upstream from the target; it had the same height and width as BTOT, but with a circular hole with 10 mm diameter at its center, and thickness of 3 mm. The counter, called HOLE, was in the trigger logic as an anti-coincidence, so that only particles passing through its hole were regarded as valid beam particles. Specifications of the counters are summarized in Table 2.4.1.

2.4.2 Bull's Eye Counter

To detect an interaction of a beam particle with a target nucleus, a Čerenkov counter was placed 11 m downstream from the target. The counter, called the Bull's Eye, measured the charge of beam particles just in front of the zero-degree calorimeter (ZCAL; see Section 2.7). Measured charge smaller than that of the incident beam particle provided the minimum bias interaction trigger.

Counter		BTOT	HOLE
Distance from the Target	[cm]	-171.	-145.
Size (w × h × d)	[mm^3]	76.2 × 50.8 × 0.20	76.2 × 50.8 × 3.2
Hole Diameter	[mm]	—	10.

Table 2.4.1: Specifications of the beam counters. A negative value of distance from the target denotes upstream of the target.

Figure 2.4.1 [44] shows a schematic view of the Bull's Eye counter. The counter had a quartz radiator of 300 μm thick and a light diffuser made of lucite foam. Produced Čerenkov light was read out through the diffuser, with eight 2-inch photo-multiplier tubes of Hamamatsu model H1161 arranged like the spokes of a wheel. Spectra of the counter and how it was included in the trigger logic are presented in Section 3.4.

2.5 Forward Spectrometer

In this section, we describe each detector component in the Forward Spectrometer, following a description of the basic and conceptual design of the spectrometer system.

2.5.1 Conceptual Design

As shown in Figure 1.2.3, the new Forward Spectrometer was placed on the opposite side of the beam line to the older arm, the Henry Higgins. The configuration of the Forward Spectrometer is schematically shown in Figure 2.5.1.

Based on the motivation to construct the spectrometer, which is described in Section 1.2, the Forward Spectrometer was designed as to be able to sweep a region from 6 degrees to about 25 degrees in the laboratory frame with respect to the incident beam. The solid angle of its acceptance was designed to be rather small ($\sim$ 5 msr), so that the multiplicity of incoming particles into the aperture was expected to be moderate, 6 – 10 in average per central Au+Au collision at the most forward angle of 6 degrees. Otherwise, reconstruction of the detected

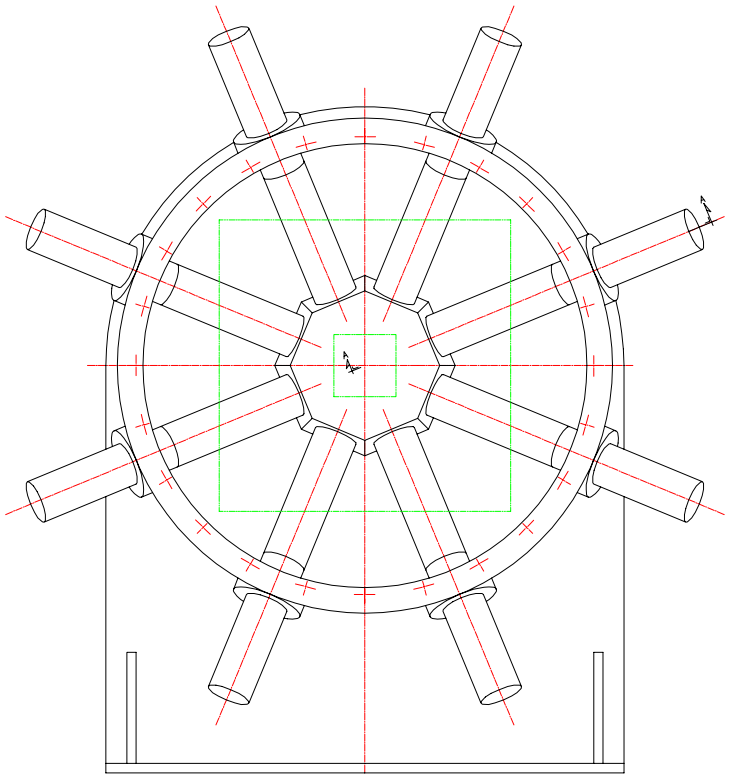

Figure 2.4.1: A schematic view of the Bull's Eye counter [44]. The small square at the center is the Čerenkov radiator.

tracks based on the information of the tracking detectors could have become too complicated a task.

In the work to fix the specifications of the Forward Spectrometer, special care was devoted for its capability to deal with high particle-density events. To reduce the spatial particle density at the detectors, the distance between the target and the center of the first chamber complex was enlarged to be 2.5 m, while it was 1.0 m for the Henry Higgins spectrometer. With the same end, the two-magnet arrangement was adopted; a dipole magnet was placed in front of the first tracking chambers as shown in Figure 2.5.1. The aim of this first magnet is to curl up secondary particles with low momenta, which can be generated in the various material in the experimental apparatus, such as the beam pipe, return yokes of the magnets, frames of the chambers, and so forth. In addition, the magnet also serves to reduce the spatial particle density at the chambers by sweeping the particles to be detected.

However at the most forward angles, it had been found by a Monte Carlo

Figure 2.5.1: A schematic view of the Forward Spectrometer at the 6 degree setting. FM1, FM2: dipole magnets. FTR1, FTR2: tracking chamber complexes. FTOF: a time-of-flight wall. For descriptions of the devices, see Section 2.5.

study [45] that the background rate in the tracking chambers would be too high to operate them properly and to reconstruct tracks with a sufficient confidence level, without any shielding installed. According to the study, the background particles at the chambers could be much reduced by putting heavy material in front of the first magnet and in the space between the beam pipe and the spectrometer arm. The designed pieces of shielding are shown in Figure 1.2.3, though all of them have not been installed so far. Among the shielding, the most essential part is the collimator in front of the first magnet, *i.e.* at the most upstream of the spectrometer system. It serves to prevent the material such as the yoke of the first magnet, which could become a major generator of background particles, from being seen from the target, and at the same time to limit the solid angle of the spectrometer itself. The aperture of the spectrometer was designed to be determined by the entrance window of the collimator, to be 4 degrees in the

horizontal direction and $\pm$ 2 degrees in the vertical, leading to the solid angle of $\sim$ 5 msr. Details of the collimator can be found in one of the following subsections.

Another essence in the design of the Forward Spectrometer was in the configuration of the tracking system. In the Henry Higgins spectrometer, four sets of drift chambers were used as the main tracking devices. For the Forward Spectrometer, however, track finding and reconstruction only with projective chambers, *e.g.* drift chambers, would be much harder work because of the higher particle density. To avoid erroneous defining of tracks, time projection chambers with capability of providing three-dimensional information on particle trajectories were selected as more suitable devices. Two tracking chamber complexes, each of which consisted of a time projection chamber and one or two accompanying drift chamber(s), were set in front of and behind the second magnet as shown in Figure 2.5.1. The main task of the time projection chambers was to find and define tracks in use of their high capability of three-dimensional pattern recognition; precise positions and angles of the found tracks were to be measured with the drift chambers, making the best use of their high spatial resolution. In use of the information of the time projection chambers, the area on the drift chambers to be searched in the reconstruction procedure for hits to be associated with a track candidate could be highly reduced, so that not only incorrectly identified tracks should diminish, but needed computation power could be also saved. Specifications of the tracking chambers are described below.

As the device for particle identification, we used a time-of-flight scintillation counter wall. The device has been designed and constructed standing on the experience of the Henry Higgins spectrometer, which has achieved excellent capability of particle identification with the time-of-flight resolution of $\sim$ 75 ps in r.m.s.. The Forward Spectrometer was equipped with a similar, but more compact, time-of-flight system. Specifications of the wall can be found in one of the following subsections.

2.5.2 Spectrometer Coordinates

We defined a coordinate system on the spectrometer as follows: the origin was at the target position; the z-axis was a line perpendicular to the surfaces of the magnets and the tracking chambers as shown in Figure 2.5.1; the y-axis was vertically upward; the x-axis was taken to form a right-handed rectangular

Magnet		FM1	FM2
Gap Size (w × h × d)	[mm^3]	229. × 159. × 508.	597. × 283. × 762.
Yoke Size (w × h × d)	[mm^3]	546. × 616. × 508.	1346. × 1422. × 762.
Effective Field Length	[cm]	62.	94.
Maximum Field	[T]	∼1.0	∼1.0
Number of Field Clamps		2	2
Clamp Thickness	[mm]	25.4	76.2
Yoke-to-Clamp Distance	[mm]	121.	121.

Table 2.5.1: Specifications of the dipole magnets.

system. The spectrometer angle was defined as the angle between the incident beam line and the z-axis of the spectrometer coordinates.

2.5.3 Dipole Magnets

The Forward Spectrometer had two dipole magnets: one (FM1) was placed upstream of the tracking chamber system to sweep out background particles with low momenta, and the other (FM2) was an analyzing magnet with an effective length of 94 cm and bending power of about 0.9 T·m at its full strength. Both of the magnets were C-shaped with iron yokes and field clumps at their entrances and exits, and their specifications are summarized in Table 2.5.1. Field maps of FM1 and FM2 were measured with Hall probes at 0.6 T and 0.4 T settings, respectively. The magnets were placed so that the z-axis of the spectrometer coordinate system was perpendicular to the entrance surfaces and 10 mm from the inside edges of the gaps. The distances from the target to the centers of FM1 and FM2 were 175 cm and 351 cm, respectively.

2.5.4 Tracking Chamber Complexes

The spectrometer was equipped with two tracking chamber complexes, in front of and behind the analyzing magnet, FM2. The chamber complexes were de-

signed aiming at dealing with high particle-density events encountered in Au+Au collisions. The first complex (FTR1) consisted of a time projection chamber (TPC1) and a drift chamber (FT2) at the downstream of TPC1*; the second (FTR2) contained a time projection chamber (TPC2) and two drift chambers (FT3, FT4) sandwiching TPC2. The time projection chambers were used as the primary track-finding devices, making the most of their high capability of three-dimensional track finding with good two-particle separation, and the main purpose of the drift chambers was to improve spatial resolution of the tracking system.

2.5.4.1 Time Projection Chambers

At the center of each tracking chamber complex, a time projection chamber was set as a main tracking device. The two time projection chambers were designed for operation under a high particle-density condition [46].

Each of the time projection chambers consisted of four major parts, as shown in Figure 2.5.2, *i.e.* an aluminum cage holding the gas, a field cage to supply the drift field for electrons, an end-cap multi-wire proportional chamber (MWPC), and a gating grid [47] to suppress field distortion caused by drifting-back positive ions [48, 49]. Specifications of the time projection chambers are summarized in Table 2.5.2.

The chambers were operated with a gas mixture of argon (75 %) and isobutane (25 %) to obtain small electron diffusion size and, consequently, small pixel size [50]. The readout scheme of the time projection chambers was the segmented anode wire readout, which has been developed to handle high multiplicity events in relativistic heavy-ion collision experiments [51, 52, 53]. Unlike a standard time projection chamber equipped at its end-cap with a MWPC with cathode pad readout, a chamber with this scheme has rows of segmented anode wires in place of long sense wires of a standard end-cap MWPC (Figure 2.5.3). The most important advantage of the scheme over the cathode pad scheme was, in our case, better two-particle separation. While the separation with cathode pads is limited primarily by the distribution of the induced charge on the pads, that with the segmented anode wire readout scheme is determined dominantly by the diffusion of the drift electrons, which can be kept reasonably small by choosing

*Another drift chamber (FT1) was installed in front of TPC1 in 1994.

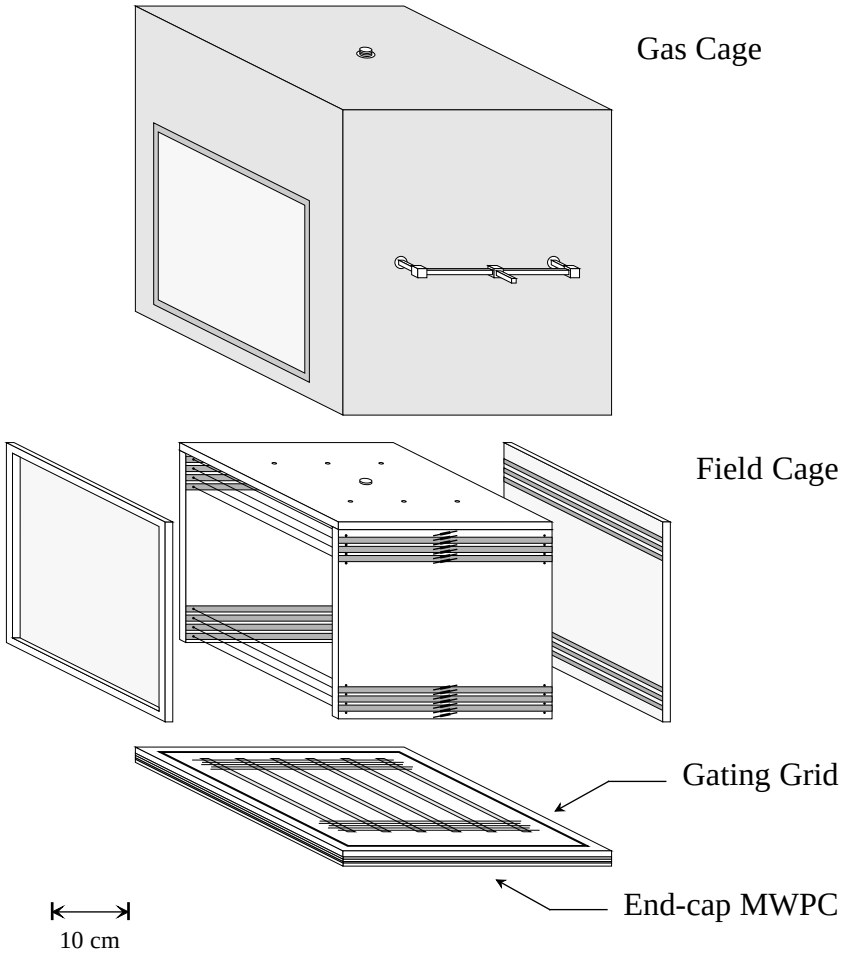

Figure 2.5.2: A schematic structure of the upstream time projection chamber, TPC1.

Chamber		TPC1	TPC2
Effective Volume (w × h × d)	[cm^3]	29. × 20. × 28.	77. × 35. × 33.
Lever Arm	[mm]	230.	270.
Number of Rows		6	6
Row-to-Row Pitch	[mm]	46.	54.
Drift Field	[V/cm]	800.	640.
Maximum Drift Length	[cm]	26.	42.
Anode-to-Anode Pitch	[mm]	3.	4.
Anode-to-Cathode Gap	[mm]	3.	4.
Effective Anode Wire Length	[mm]	7.	7.
Anode Wire Diameter	[μm]	15.	15.
Operation Voltage	[-kV]	1.90	2.15 - 2.20
Number of Anode Wires	[/row]	96	192
Total Number of Readout		576	1152
Gating Grid Wire Pitch	[mm]	1.	1.
Grid-to-Cathode Distance	[mm]	8.	8.
Gating Grid Operation Voltage	[V]	±80.	—*

Table 2.5.2: Specifications of the time projection chambers. * The gating grid of TPC2 was kept open in 1993 runs.

an appropriate gas mixture. Other advantages of the scheme include the smaller amount of the data and availability of pipeline TDC modules with lower cost compared to the modules needed to read out cathode pads.

As the readout modules for the time projection chambers, we used current pre-amplifiers of Radeka type [54] and amplifier/discriminator boards, which were designed by the KEK electronics group originally for experiments at the Superconducting Kaon Spectrometer [55] at KEK. The pre-amplifier boards contained 16 each hybrid amplifier chips, and were directly mounted on the bottom planes of the chambers. The quasi-differential output of the pre-amplifiers were sent to the amplifier/discriminator cards, which were arranged in crates on the spectrometer platform to reduce the electric noise by minimizing the length of the analog cables. FASTBUS pipeline TDC's of LeCroy model 1879 were used to record the timing of the leading and trailing edges of the discriminated signals. The TDC's were programmed to have a time range of 6 μsec for TPC1, and 12 μsec for TPC2, in order to cover the maximum drift time.

As mentioned above, TPC1 and TPC2 were also equipped with gating grid systems. In 1993 runs, we operated the gating grid system only for TPC1 in the upstream tracking chamber complex which was under a severer condition.

Performance of the chambers is summarized in Table 4.2.2, and more detailed studies of their performance can also be found in References [56, 57]. The both chambers were positioned normal to the z-axis of the spectrometer coordinates; the distances form the target to their centers were 250 cm and 458 cm, respectively.

2.5.4.2 Drift Chambers

Three projective drift chambers (FT2 – FT4) were utilized for tracking, complimentary to the time projection chambers, to improve spatial resolution of the tracking system. Geometrical specifications of the drift chambers are summarized in Table 2.5.3. Each pair of adjacent planes was staggered by the half size of the cells, *i.e.* the pitch between a sense wire and a cathode wire, to solve the left/right ambiguity. The gas mixture used for the drift chambers was argon (50 %) and isobutane (50 %).

Signals from the sense wires were read out with pre-amplifier cards plugged on the chambers in groups of 16 channels each, and were then received by main am-

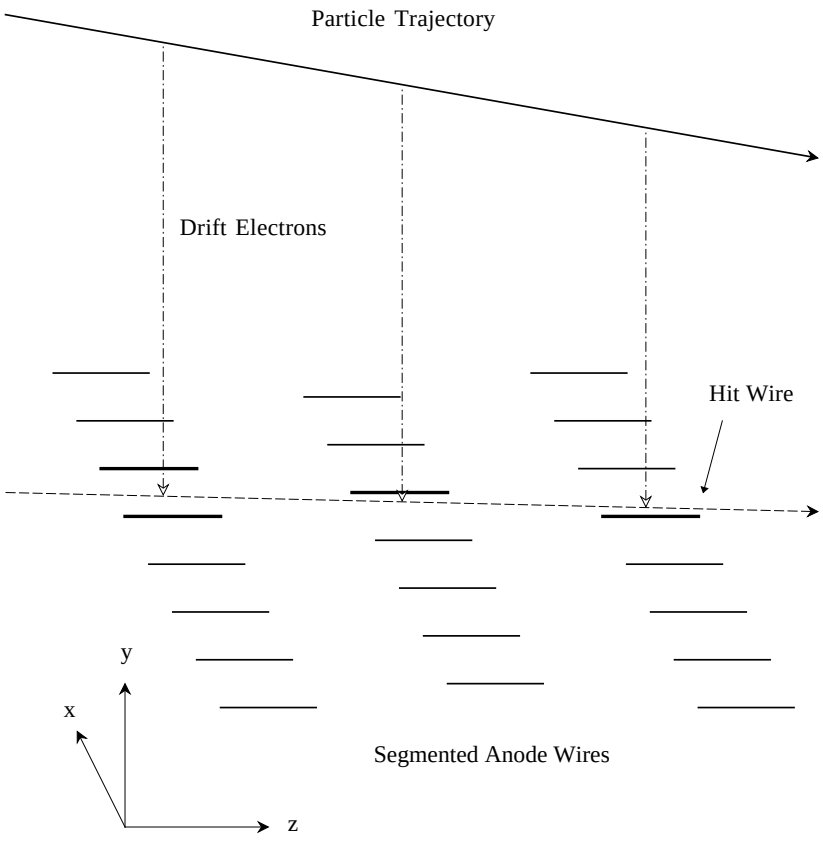

Figure 2.5.3: A schematic view of segmented anode wires of a time projection chamber. A particle trajectory and drift path of electrons are also shown.

Chamber	Wire Orientation		# Planes	# Wires / Plane	Drift Length
FT2	X	0. deg.	4	56	3.0 mm
	Y	90. deg.	2	36	3.0 mm
	U	-30. deg.	2	64	3.0 mm
	V	30. deg.	2	64	3.0 mm
	total		10 planes	552 wires	
FT3	X	0. deg.	4	78	4.0 mm
	U	-30. deg.	2	80	4.0 mm
	V	30. deg.	2	80	4.0 mm
	total		8 planes	632 wires	
FT4	X	0. deg.	4	78	5.0 mm
	U	-30. deg.	2(1)*	80	5.0 mm
	V	30. deg.	2(1)*	80	5.0 mm
	total		8(6) planes*	632(472) wires*	

Table 2.5.3: Geometrical specifications of the drift chambers. The wire orientation was measured from the vertical, and counterclockwise looking into the beam. * U and V modules of FT4 had only 1 plane each operational in 1993 runs; total number of operating planes was 6.

plifiers and discriminators arranged in crates on the spectrometer platform. The discriminated signals from two adjacent channels were recorded in one channel of a FASTBUS pipeline TDC of LeCroy model 1879, delaying one of the signals by 400 nsec which was much larger than the maximum drift time; this technique was developed at BNL to reduce the cost of the TDC modules. The time range of the TDC's was set at the minimum value of 1 μsec with the best timing resolution of 2 nsec.

All the drift chambers were positioned normal to the z-axis of the spectrometer coordinates. The distances form the target to their centers were 224 cm, 427 cm, and 489 cm, respectively.

Flight-Path Length	[m]	6.0
Effective Area (w × h)	[cm^2]	126. × 42.
Number of Segments		100(95)*
Segment Size (w × d × h)	[mm^3]	12.4 × 12.5 × 419.

Table 2.5.4: Geometrical specifications of the time-of-flight wall. * Out of 100 slats of FTOF, only 95 was operational in 1993 runs.

2.5.5 Time-of-Flight Wall

Aiming at systematic studies of semi-inclusive spectra of identified mesons and baryons produced in relativistic heavy-ion collisions, high capability of particle identification was a requirement for the experiment. Standing on experience of the E802/859 experiments, we adopted a time-of-flight scintillation counter wall as the particle-identification device.

The time-of-flight wall, FTOF, was at the most downstream of the Forward Spectrometer. It was tilted on the x-z plane by -6 degrees with respect to the x-axis, as seen in Figure 2.5.1, in order to maximize its effective segmentation. The distance from the target to the beam-side edge of the time-of-flight wall was 600 cm. Table 2.5.4 summarizes geometrical specifications of the wall.

The time-of-flight wall had 100 segments, though only 95 of them were operational in 1993 runs. Each segment, called a slat, was a rod of plastic scintillator, BC404 of Bicron. It was read out with two photo-multiplier tubes of Hamamatsu model R3478S, through light guides on its both ends. Mounted on each tube was a newly developed on-tube discriminator board with two outputs: analog and discriminated [58]. The discriminated outputs were transmitted to the second discriminators in the counting house via 68 m long coaxial cables, and then were recorded with CAMAC TDC's of Phillips model 7186, each of which contained 16 channels of time digitizers with the minimum binning of 25 psec. The analog outputs were also put into FASTBUS ADC's of LeCroy model 1882N in the counting house; the ADC information was used for so-called slewing correction (Section 4.2) as well as for a charge cut (Section 4.3).

2.5.6 Collimator

A high particle density condition is one of the major experimental difficulties in relativistic heavy-ion collision experiments. The Forward Spectrometer was therefore equipped with a sweeping magnet, FM1, in front of the tracking chambers. At the most forward angles, however, it turned out by a Monte Carlo study that the background particles coming into the chambers needed to be further reduced to make the spectrometer system properly functioning [45]. The solution was to place shielding of heavy material in front of FM1, so as to limit the spectrometer aperture. In 1993 runs, we used a lead collimator. Its front surface having a square window of 52 mm high and 52 mm wide was placed 76 cm from the target, leading to the opening angle of 4.0 degrees by 4.0 degrees (about 5 msr in solid angle). The body of the collimator covered the entire solid angle of the tracking chambers viewed from the target position, except through the window. The thickness of the collimator was 56 cm, corresponding to 3.3 nuclear interaction length (1.0×10^2 radiation length).

2.6 Henry Higgins Spectrometer

The other arm of magnetic spectrometer (the Henry Higgins spectrometer) [36] was on the other side of the beam line. It has been used for the E802/859 experiments with lighter beams up to ^{28}Si, and for the E866 experiment to cover the backward region from about 20 degrees with respect to the incident beam. Its advantage over the Forward Spectrometer was a larger aperture of 25 msr, but it could not handle the high particle density encountered in Au+Au collisions at the forward angles in the laboratory frame, as noted in Section 1.2. Kinematic coverages of the two arms, however, had some overlap, which provided means to check systematics of analysis.

Since the spectrometer arm was not used in the data analysis in this thesis, we omit detailed descriptions of the Henry Higgins spectrometer here.

2.7 Zero-degree Calorimeter

As an event characterization device, a scintillator/iron calorimeter (ZCAL) was placed at the end of the beamline, 11.7 m downstream from the target, to measure the total kinetic energy of beam particles and fragments.

It has been found in the E802/859 experiments that the energy deposit in ZCAL and the energy emitted in the transverse direction have a strong negative correlation [30], indicating that the both observables could be measures of the collision geometry, *i.e.* centrality. In the analysis in this thesis, the energy deposit in ZCAL was used to define the centrality of the collisions; the less the energy deposit was, the more central the event was considered.

ZCAL had a face of 600 mm by 600 mm toward the beam, and consisted of 138 layers of scintillator and iron with a length of 193 cm (8.9 interaction length). The whole volume was divided into two blocks, the upstream and the downstream, and each of them was read out with eight photo-multiplier tubes.

2.8 Data Acquisition System

The data acquisition system consisted of a VAX 11/785 host computer and VME-based front ends [59, 60]. The main front end with a Motorola 68020 microprocessor was called the Chairman, and supervised all activities of the front ends. A VME-resident intelligent interface was assigned to each CAMAC crate; all the crates could be read out thereby in parallel. There was also a FASTBUS interface which could handle up to 16 FASTBUS crates through a data/control highway. Collected data were sent out by the Chairman to the host computer via the VME link server. The host, VAX11/785, recorded the received data onto magnetic tapes.

Chapter 3

Run Conditions

3.1 Overview

In this chapter, we present a summary of various experimental conditions of the data taken in October, 1993, with the E866 Forward Spectrometer. The statistics of the analyzed data set is shown at the end of this chapter.

3.2 Target

We used a ^{197}Au target with an interaction rate of about 1.5 % with the ^{197}Au beam. Specifications of the target are summarized in Table 3.2.1. Data with empty target were also collected for subtraction of the background contribution (see Section 5.2) at each angle setting of the Forward Spectrometer.

Target Nucleus	Au
Atomic Number (Z)	97
Mass Number (A)	197
Thickness (D) [g/cm^2]	0.975

Table 3.2.1: Specifications of the target.

3.3 Beam Conditions

The beam intensity was controlled at $3 - 7 \times 10^4$ particles per spill. The beam profile was monitored with beam line chambers (SWIC's) provided by the AGS beam line group, and also with the counting rate of the beam counters. The counting rate of HOLE counter was kept less than 1 % of the rate of $BEAM$ trigger defined in Section 3.4.

3.4 Trigger Conditions

We collected data in parallel with three different trigger conditions. For descriptions on the devices making the triggers, see Sections 2.4 and 2.7.

3.4.1 Trigger Setup

The trigger with an incoming beam particle ($BEAM$) was defined only with the beam counters BTOT and HOLE as

$$BEAM \equiv \overline{PRE} \cap BTOT_1 \cap BTOT_2 \cap \overline{HOLE_1 + HOLE_2} \quad (3.4.1)$$

where $\overline{PRE}$ shows pile-up rejection for a beam particle preceded by another particle within 1 μsec, subscripts 1 and 2 represent photo-multiplier tubes on the both ends of the scintillator, and + denotes an analog sum of the two signals. Data collected with this trigger was used for various calibration purposes.

The interaction trigger (INT) was defined using the Bull's Eye counter as

$$INT \equiv BEAM \cap \overline{BE} \quad (3.4.2)$$

where $\overline{BE}$ represents light yield in the Bull's Eye counter less than the threshold. Figure 3.4.1 shows ADC spectra of the counter, taken with $BEAM$ and INT triggers.

To collect data from central collisions efficiently, we formed a central trigger ($\overline{ZCAL}$) with the zero-degree calorimeter as

$$\overline{ZCAL} \equiv INT \cap \overline{ZCAL_{SUM}} \quad (3.4.3)$$

where $\overline{ZCAL_{SUM}}$ means measured energy in the zero-degree calorimeter less than the threshold. The threshold was adjusted so that about 10 % of INT trigger events gave $\overline{ZCAL}$ triggers.

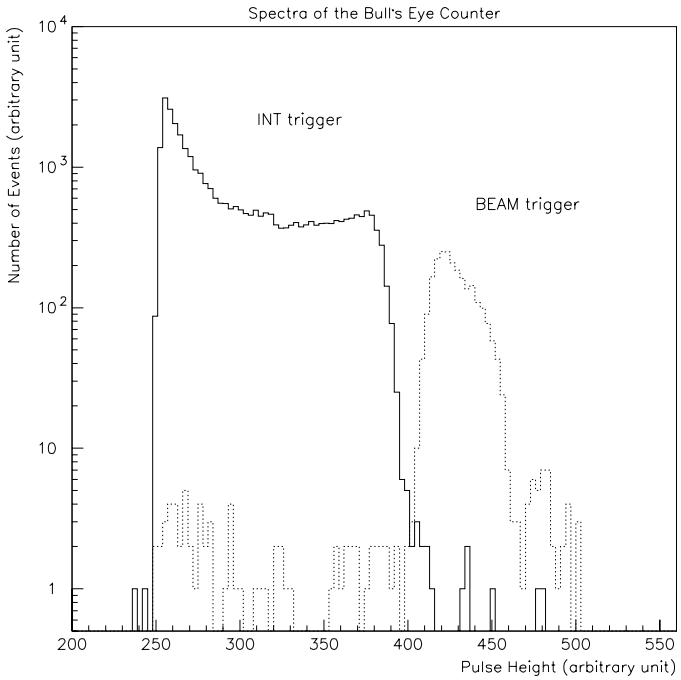

Figure 3.4.1: ADC spectra of the Bull's Eye counter. The two overlaid spectra correspond to two trigger conditions, $BEAM$ (dotted histogram) and INT (solid histogram).

3.4.2 Trigger Rate

The trigger signals were managed by a VME-bus-based trigger supervisor [61]. It set scale-down factor for each trigger and changed the rate at which events of the trigger type were to be written on the data tapes.

Using the target with an interaction rate of about 1.5 %, the ratio of trigger rate of INT to $BEAM$ was 2.5 – 3.0 % due to background contributions such as interactions of the beam particles with the beam counters. The procedure of the background subtraction is described in Section 5.2. $\overline{ZCAL}$ trigger was, on the other hand, set up as mentioned above so that its rate was about 10 % of INT trigger's. In most runs, the scale-down factors were set at 2,500, 5, and 1 for $BEAM$, INT, and $\overline{ZCAL}$ triggers, respectively; the typical rate of data collection was, then, 5 – 6 $BEAM$, 60 – 80 INT, and 25 – 35 $\overline{ZCAL}$ events per spill. The dead time of the data acquisition system was typically 50 – 70%.

Polarity	A			B		
Trigger	$BEAM$	INT	$\overline{ZCAL}$	$BEAM$	INT	$\overline{ZCAL}$
6 degrees	5.4K	66.2K	37.6K	9.3K	123.3K	50.2K
9 degrees	7.3K	96.7K	39.0K	6.5K	86.7K	35.4K
12 degrees	6.3K	85.1K	34.0K	6.1K	81.4K	32.9K
15 degrees	—	—	—	6.2K	82.8K	33.5K
18 degrees	5.3K	70.5K	28.3K	5.9K	78.3K	31.2K
21 degrees	7.0K	67.5K	37.6K	6.7K	88.6K	35.9K
Total	31.3K	386.0K	176.5K	40.7K	541.1K	219.1K

Table 3.6.1: A summary of the data statistics. The leftmost column lists the spectrometer angle.

3.5 Spectrometer Setting

The spectrometer was rotated in 3-degree steps, considering kinematic overlap between the settings, from 6 degrees to 21 degrees. At each spectrometer angle, we took data with two different polarity settings of FM1 and FM2; one favoring positively charged particles and the other favoring negatives. The polarity which bent positive particles toward the beam was called the A polarity, which was the negative-favor setting for the Forward Spectrometer; the other polarity was called the B. The magnetic field of FM1 was set at 0.2 T except for zero-field runs, and that of FM2 was at 0.4 T.

3.6 Data Statistics

Here we summarize in Table 3.6.1 the statistics of collected data for each spectrometer angle, polarity setting, and trigger type.

Because of a hardware trouble, A polarity data at 15 degrees were not included in the data analysis.

Chapter 4

Data Analysis I — Data Reduction

4.1 Overview

The procedure of the data reduction for the Forward Spectrometer is described in this chapter, divided into five sections. In Section 4.2, fine tuning of the detector alignment and calibration of the detectors are summarized. The main parts of the data reduction, *i.e.* track reconstruction, momentum determination, and particle identification, are described in the following three sections (4.3 – 4.5). Finally, several correction factors to be applied in the analysis are discussed in Section 4.6.

4.2 Calibration

The topics in this section include two kinds of, but not independent, issues: one is fine tuning of detector alignment, or relative geometry of the detectors, and the other is calibration of the detector components. Note that the positions of all the detectors were primarily based on the survey results. Considering the finite precision of the survey, and possible changes of the alignment with rotating the spectrometer, only fine tuning was performed to the alignment using data with straight tracks taken in zero-field runs.

Practically, calibration of the detectors needs to be performed in parallel to track reconstruction work, since calibration of some detectors requires information from other detectors. The time projection chambers, for example, cannot

measure the absolute y-positions of tracks without accompanying drift chambers since there is no way to determine their time-zero by themselves. The time-of-flight wall also requires tracking information, *e.g.* the momenta of reconstructed particles, to be calibrated precisely. For the sake of convenience, however, the procedure of calibration is described as a separated issue in this section. For details of track reconstruction, see Section 4.3.

4.2.1 Internal Geometry of Tracking Chamber Complexes

The internal geometry of each tracking chamber complex was calibrated using tracks reconstructed with the time projection chamber in the chamber complex. The basic principle was to project tracks from the time projection chamber onto the accompanying drift chambers, and make them match with the positions of hit wires of the drift chambers. The drift chambers were treated as MWPC's at this stage, since their timing information had not been calibrated yet.

Using the x-planes of the drift chambers, the relative positions of the chambers were first adjusted in the x-direction. Though FT3 or FT4 did not have y-planes, the u- or v-planes also provided us with the y-positions of tracks, once adjustment in the x-direction had been done. The relative positions of the chambers in the y-direction and the time-zero of the time projection chambers, which was equivalent to their absolute y-positions, were then calibrated using the y-information.

The displacement of the chambers from their surveyed positions was found to be 1.1 mm at most, which was consistent with the precision of the survey. For various angle settings of the spectrometer, the internal geometry was consistent within 100 μm and 800 μm in the x- and y-directions, respectively.

4.2.2 Time Projection Chambers

From the TDC information of a time projection chamber, the y-position of a track was derived as

$$y \;=\; v \cdot \left(\frac{t_l + t_t}{2} - t_0 \right) \;, \tag{4.2.1}$$

where v is the drift velocity of electrons, t_l is the timing of the leading edge of a pulse and t_t is of the trailing, and t_0 is the time-zero. The drift velocity and the

time-zero were calibrated at the same time with the internal geometry adjustment in the tracking chamber complexes.

During the running period, the drift velocity v was found to be constant within 0.1 % for TPC1, and within 0.7 % for TPC2; the average velocity was 49.7 mm/μsec and 48.6 mm/μm for TPC1 and TPC2, respectively, and was consistent with the expected values [62].

4.2.3 Drift Chambers

For each of the drift chambers, the relation between the drift time and the drift length was calibrated using tracking information from the time projection chamber in the same chamber complex. The relation was approximated with an equation:

$$x(t) \;=\; a\sqrt{t-t_0} + b(t-t_0) + c(t-t_0)^2 \qquad (4.2.2)$$

where $x(t)$ is the drift length, $(t-t_0)$ is the TDC value subtracted with the time-zero, and a, b, and c are calibration constants. The constants were calibrated on a plane-by-plane basis, and the time-zero on a wire-by-wire.

4.2.4 Global Geometry of Tracking Chamber Complexes

The relative geometry of the two tracking chamber complexes was adjusted using straight tracks in zero-field runs; data with the both magnets off were taken at each spectrometer angle for the geometry adjustment, since the two chamber complexes could move relative to each other with different angle settings of the spectrometer. The maximum misalignment of FTR1 from the result of the survey was 1.4 mrad in the x- and 1.8 mrad in the y-direction; that of FTR2 was 1.4 mrad and 3.4 mrad in the x- and y-directions, respectively.

4.2.5 Time-of-Flight Wall

Calibration of the time-of-flight wall, FTOF, was performed after track reconstruction and momentum determination (Sections 4.3 and 4.4). The time of flight TOF and the y-position y_{TOF} of a particle were calculated from the TDC/ADC

information of a hit on FTOF as

$$TOF = C \cdot \frac{t_{cor}^{top} + t_{cor}^{bot}}{2} - t_0^g \tag{4.2.3}$$

$$y_{TOF} = v \cdot \frac{t_{cor}^{top} - t_{cor}^{bot}}{2} \tag{4.2.4}$$

$$t_{cor}^i = t^i - t_0^i - \left\{ s_0^i + s_1^i \left(\frac{a^i - a_0^i}{g^i} \right)^{-\frac{1}{2}} \right\} , \tag{4.2.5}$$

where

t^i	:	TDC value
t_0^i	:	time-zero
a^i	:	ADC value
a_0^i	:	ADC pedestal
g^i	:	gain of a photo-multiplier tube
s_j^i	:	slewing correction factors ($j = 0, 1$)
C	:	clock of a TDC [nsec/bin]
t_0^g	:	global time-zero
v	:	propagation velocity of scintillation light [mm/bin]

and $i = top$ or bot denotes one of the photo-multiplier tubes on the both sides of a slat. For roughly selected high momentum pions with the minimum effect of multiple scattering, the expected time of flight and y-position on the time-of-flight wall were independently calculated from the tracking information. Calibration of FTOF was performed to let the two ways of measurement achieve the best agreement.

Performed calibration is listed in Table 4.2.1; the position and the size of FTOF in the x-direction were also adjusted using matching with the track projections.

4.2.6 Magnets

The ratio of the bending power between FM1 and FM2 was calibrated using the dependence of the x-position of the target image on momentum. Figure 4.2.1 shows the dependence before calibration in a 12 degree run; the momentum dependence indicated an incorrect bending-power ratio, since reconstructed tracks

Parameter	Calibration Conditions
Global Time-Zero	for each run
Relative Time-Zero	for each PMT; common for all runs
ADC Pedestal	for each PMT; common for all runs
Gain of PMT	for each PMT; common for all runs
Slewing Parameters	for each PMT; common for all runs
Propagation Velocity	for each slat; common for all runs
Clock of TDC	not calibrated

Table 4.2.1: Calibration performed for the time-of-flight wall. PMT stands for photo-multiplier tube.

were traced back to the target position through FM1 assuming the momenta determined with FM2.

For the A and the B polarity settings defined in Section 3.5, the ratio was found to be off by 1.4 % and 0.7 %, respectively, from the expected value. Because the information was only on the ratio, the discrepancy from the expected setting was shared equally between the two magnets.

4.2.7 Performance of the Detectors

Let us review the performance of the detectors in the Forward Spectrometer here. The efficiency and the spatial/timing resolution of each detector were calculated from the residual distribution with the track projection onto the detector. Fully reconstructed positively charged pions within the momentum range from 1.0 GeV/c to 3.0 GeV/c were selected for the examination, to minimize the effect of multiple scattering and of contamination by other particle species.

Table 4.2.2 summarizes the performance of the detectors in a 12 degree run. All the values listed were averaged over the effective areas, while the detection efficiency of the time projection chambers was found to have a position dependence (Section 4.6). Note that the listed values of resolution are in r.m.s..

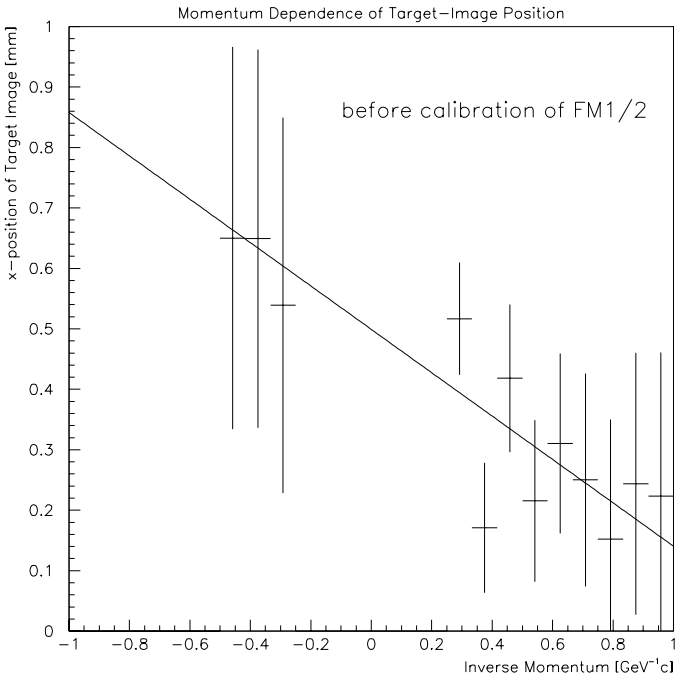

Figure 4.2.1: The momentum dependence of the x-position of the target image in a 12 degree run, before calibration of the field-strength ratio between FM1 and FM2. The solid line represents the result of fitting.

4.3 Track Reconstruction

We developed a tracking code for the Forward Spectrometer, which was called FAReAST*. The procedure of track reconstruction is described in this section.

The basic tracking algorithm was as follows: the first step of track reconstruction was performed independently in each tracking chamber complex; if a track found in FTR1 matched with one in FTR2 at the center of FM2, it was regarded to form a track passing through the spectrometer and the momentum of the particle was calculated from the bending angle in FM2; the track was traced back to the target position through FM1 using the calculated momentum to check if it was a real particle coming from the target; a hit on the time-of-flight wall to be associated with the track was also searched for.

Figure 4.3.1 displays a typical high particle-multiplicity event in a 12 degree

*Forward Arm Reconstruction Algorithm Starting from the TPC's.

Time Projection Chambers		TPC1	TPC2
Efficiency per Row		88 %	84 %
Resolution per Row	(x)	0.73 mm	1.06 mm
	(y)	0.36 mm	0.57 mm
Cluster Size	(x)	3.9 mm	4.9 mm
	(y)	1.6 mm	2.2 mm

Drift Chambers	FT2	FT3	FT4
Efficiency per Plane	91 %	91 %	92 %
Resolution per Plane	0.32 mm	0.30 mm	0.38 mm

Time-of-Flight Wall		FTOF
Timing Resolution		74 psec
Position Resolution	(y)	8.9 mm

Table 4.2.2: A summary of the performance of the detectors in the Forward Spectrometer. The examination was performed in a 12 degree run. The listed values of resolution are in r.m.s..

run with five reconstructed tracks.

4.3.1 Track Finding in Time Projection Chambers

Track finding was started from each of the two time projection chambers, making the most of their capability to provide three-dimensional information.

Because of diffusion of drift electrons, more than one wire on a row could be fired by a single particle. Hits on a row which were close in both of the x- and y-directions were hence associated together to form a cluster. Since the time projection chambers were out of the magnetic field, each particle passing through one of them left a cluster on each row, nearly aligned on a straight track. Track finding in a time projection chamber was accordingly to find aligned clusters on several rows of the chamber. The required numbers of fired rows were set at 4 and 3 (out of 6 each) for internal tracking of TPC1 and of TPC2, respectively, considering the finite inefficiency of the chambers.

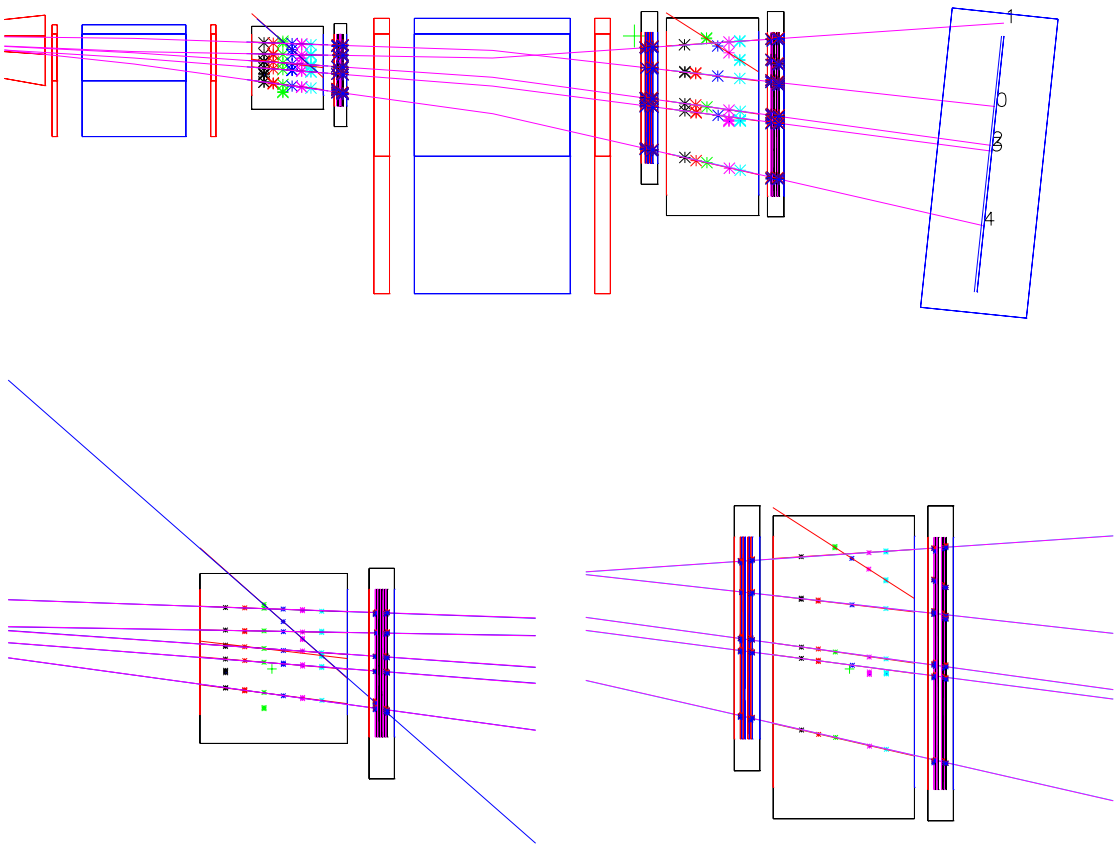

Figure 4.3.1: A typical high particle-multiplicity event in a 12 degree run. Upper: a top view of the Forward Spectrometer and reconstructed tracks. Lower left: a top view of the first tracking chamber complex, FTR1. Lower right: a top view of the second tracking chamber complex, FTR2.

Chamber	# Existing	# Required
TPC1	6 rows	4 rows
TPC2	6 rows	3 rows
FT2	10 planes	6 planes
FT3	8 planes	4 planes
FT4	8(6) planes*	2 planes

Table 4.3.1: The required numbers of rows and planes to form a FS track; see text for a description. * Only 6 planes of FT4 were operational in 1993 runs.

4.3.2 Track Confirmation with Drift Chambers

Each track found in a time projection chamber, which we called a TPC track, was extrapolated onto drift chambers accompanying the time projection chamber, to find hits on the drift chambers to be associated with the track. On each plane of each drift chamber, the two wires closest to the track projection were examined if fired; if one (or both) of them was fired, it was regarded as associated with the track. Each TPC track was required to be associated with hits on a certain number of planes of the drift chambers, or was discarded otherwise. The requirement on number of fired planes in each drift chamber is tabulated in Table 4.3.1. A TPC track confirmed with the accompanying drift chambers was called a FTR track.

4.3.3 Track Fitting

Each FTR track was fitted with a straight line using the position information of both the time projection chamber and the drift chambers. The left/right ambiguity on each plane of the drift chambers was solved at the same time, in an iterative way to minimize the χ^2 of the fitting. When hits on two near-by wires on the same plane of a drift chamber had been associated with a track, the hit leading to the less χ^2 was chosen in this stage.

4.3.4 Track Matching at Analyzing Magnet

After fitting FTR1/2 tracks with straight lines, the tracks were extrapolated to the analyzing magnet, FM2. For each pair of the FTR1/2 tracks, matching plane in FM2 was defined as shown in Figure 4.3.2 based on an effective edge approximation. Each track pair was checked if the two tracks matched in distances in the x- and y-directions and also in angle on the y-z plane. The matching criteria needed to depend on momentum due to the resolution of the tracking system including an effect of multiple scattering, but the momenta of the track candidates were not yet known at this stage. The cut here was therefore set loose, *i.e.*

$$|\Delta x| < 10\sigma_{p=\infty}(\Delta x) \quad (4.3.1)$$

$$|\Delta y| < 10\sigma_{p=\infty}(\Delta y) \quad (4.3.2)$$

$$|\Delta \frac{dy}{dz}| < 10\sigma_{p=\infty}(\Delta \frac{dy}{dz}) \ , \quad (4.3.3)$$

where Δx and Δy are the distances between the two tracks in the x- and y-directions, respectively, on the matching plane, $\Delta(dy/dz)$ is the angle difference on the y-z plane, and $\sigma_{p=\infty}$ denotes the r.m.s. width of the matching at the limit of high momentum, which was determined from the data. A matched pair of FTR1/2 tracks was regarded as a track passing through the two tracking chamber complexes, and recorded as a FS track. Existence of associated hit(s) on the time-of-flight wall was not required at this stage.

The cut was refined in a later stage of tracking, after momentum determination (Section 4.4), by applying a momentum-dependent cut in the three-dimensions. The cut width was determined based on the data at the most forward angle (6 degrees) in the momentum range from 1.0 GeV/c to 4.0 GeV/c. Figure 4.3.3 shows the r.m.s. width $\sigma(p)$ of track matching in a 12 degree run, as a function of momentum. At below 1.0 GeV/c, the data statistics was not enough to determine the width of matching; we hence used an extrapolation function as follows:

$$\sigma^2(p) = \left(\sigma_{p=\infty} + \frac{\sigma_{p=1} - \sigma_{p=\infty}}{p}\right)^2 + \left(\frac{\sigma_{p=1}}{p}\right)^2 \quad (4.3.4)$$

where $\sigma_{p=1}$ denotes the matching width for particles with momentum of 1 GeV/c. The momentum-dependent cut was applied at $\pm 5\sigma(p)$. An effect of various cuts in track reconstruction is discussed and corrected in Section 4.6.

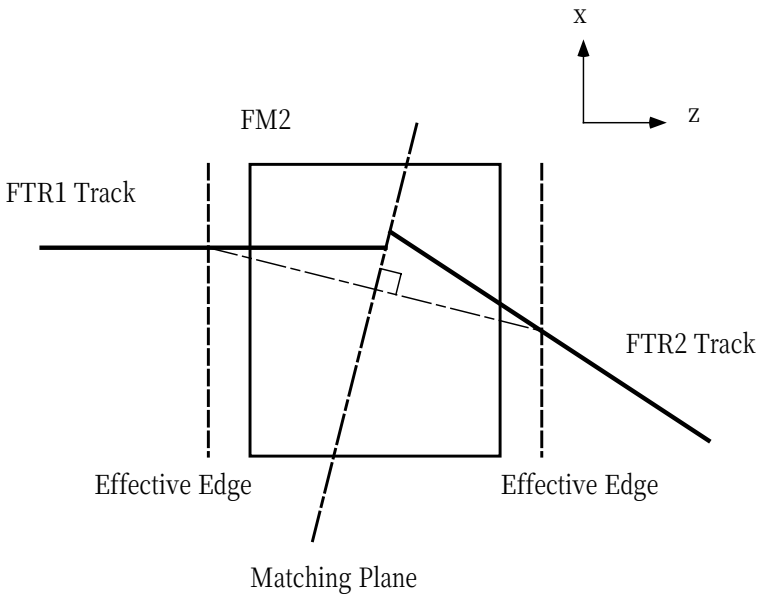

Figure 4.3.2: The definition of the matching plane at the analyzing magnet, FM2.

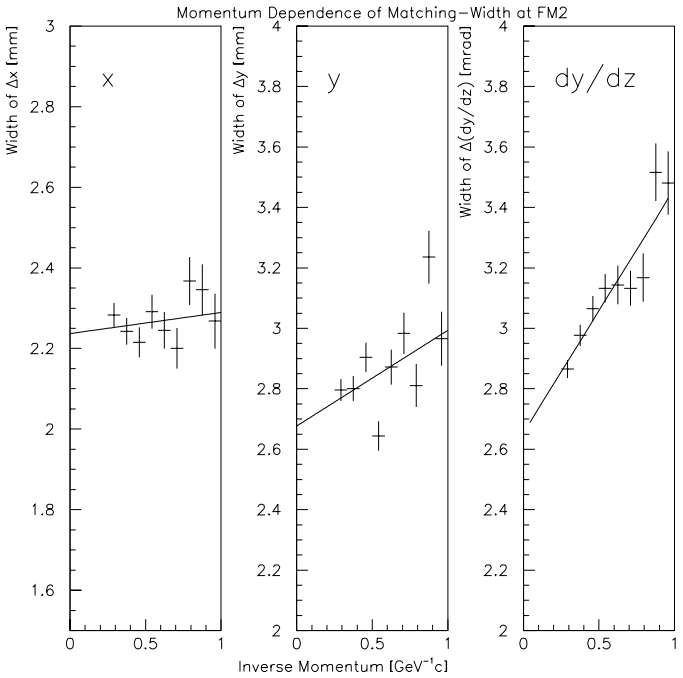

Figure 4.3.3: The r.m.s. width of track matching at the analyzing magnet in a 12 degree run, as a function of momentum. Left: x-position matching. Middle: y-position matching. Right: dy/dz angle matching.

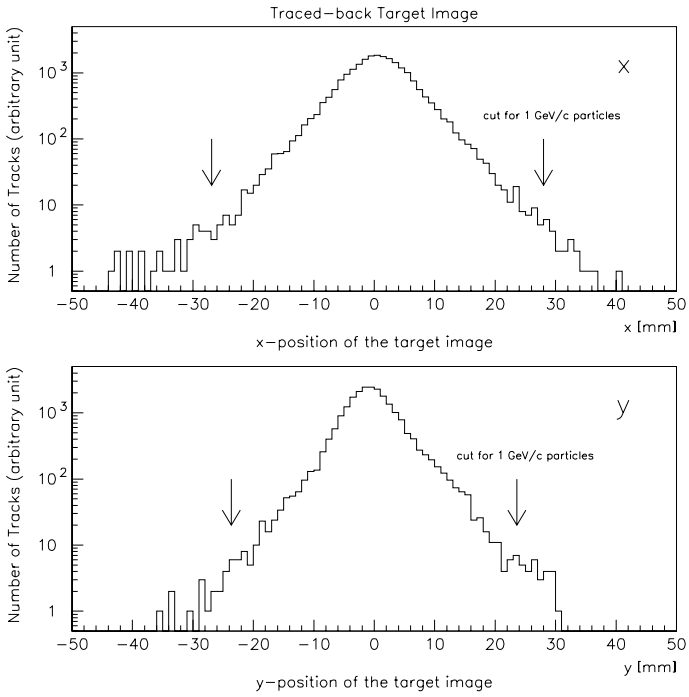

Figure 4.3.4: Traced-back target images in the x- and y-directions in a 12 degree run. The cut width for 1 GeV/c particles are indicated by arrows.

4.3.5 Target Cut

After momentum determination, each FS track was traced back to the target position through FM1 with a ray tracing method. Figure 4.3.4 shows the target image without a momentum cut in a 12 degree run; the width of the target image was momentum dependent as shown in Figure 4.3.5. A target cut was applied at $\pm 3\sigma(p)$ in the x- and y-directions, where $\sigma(p)$ denotes the momentum-dependent r.m.s. width of the target image at the most forward angle setting, *i.e.* 6 degrees. For momentum below 1.0 GeV/c, the same extrapolation function as for track matching at FM2 (Equation 4.3.4) was used for $\sigma(p)$.

Since we regarded any pair of FTR1/2 tracks matching at FM2 as a FS track, some *ghost* tracks could be created in the matching stage. Most of fake tracks generated from accidental matching of wrong combinations were to be rejected by the target cut, due to their incorrectly calculated momenta. Nevertheless, ghost tracks generated in one of the time projection chambers in the stage of internal

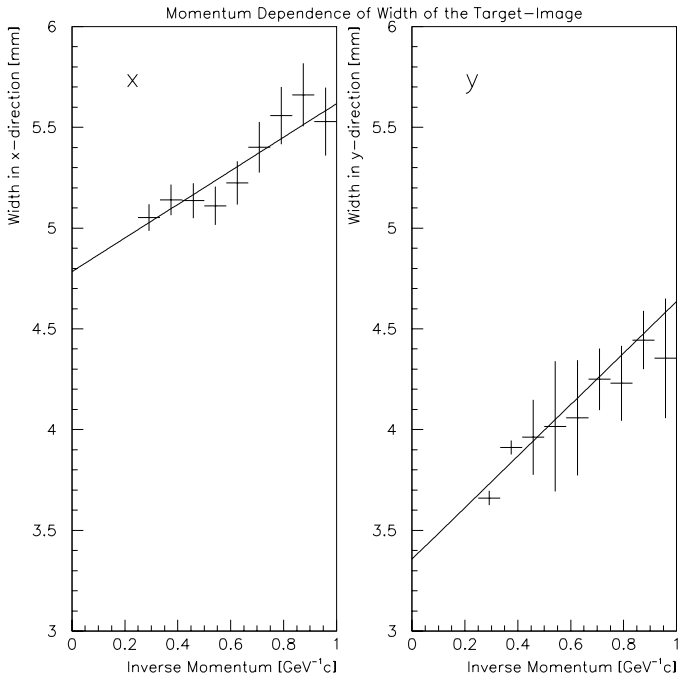

Figure 4.3.5: The r.m.s. width of the target image in a 12 degree run, as a function of momentum. Left: the x-direction. Right: the y-direction.

tracking could satisfy the cut criteria, since they tended to be bunched close to one another within the two-particle separation of the time projection chambers. Among such a cluster of tracks sharing a FTR1 or a FTR2 track, only the track which was traced back closest to the target position was selected while the others were discarded as fake tracks.

4.3.6 Fiducial Cut

Since the acceptance of the spectrometer was determined by the collimator in front of FM1, the emission angles of accepted particles should have a clear cutoff both in the x- and y-directions. Due to the finite angular resolution of the spectrometer, however, the measured distribution of emission angle had blunt edges as shown in Figure 4.3.6. This effect might distort the particle distribution near the edges of the geometrical acceptance. Also, incomplete survey of the collimator position could lead to a large systematic error associated with the acceptance calculation (Section 5.5) near the edges. To avoid these effects and

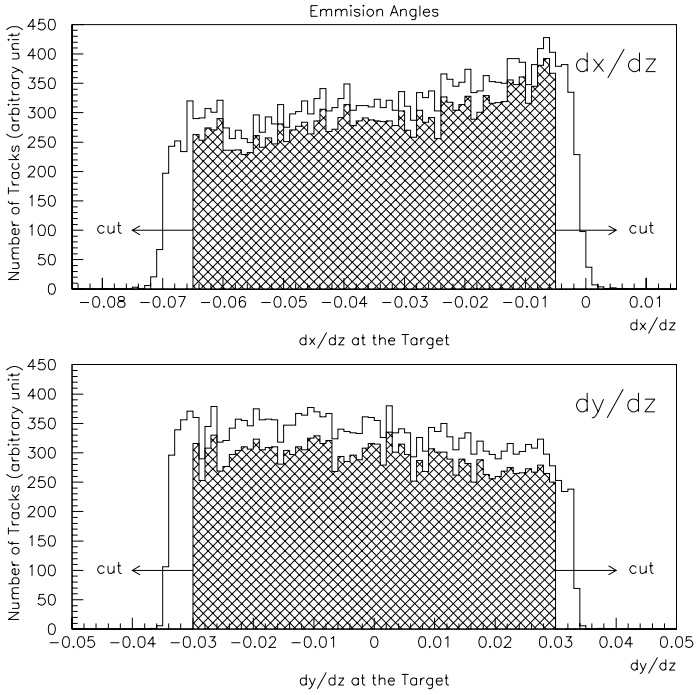

Figure 4.3.6: Distributions of measured emission angle and the applied fiducial cut; in a 12 degree run and in the spectrometer coordinates. The hatched areas represent distributions of tracks after the fiducial cut. Upper: on the x-z plane. Lower: on the y-z plane.

reduce systematic errors, a fiducial cut was applied on the emission angle at the target. The applied cut is also shown in Figure 4.3.6.

4.3.7 Association with Time-of-Flight Wall

For each FS track, a hit on the time-of-flight wall was searched for to be associated; the track was extrapolated onto FTOF, and position matching in the x- and y-directions was required. Figure 4.3.7 shows the momentum dependence of the r.m.s. width σ of the matching in a 12 degree run. The width in the y-direction was treated as a constant, since it was dominated by the position resolution of the time-of-flight wall and showed little dependence on momentum. On the other hand, the width in the x-direction was found to be momentum-dependent in the examined momentum range from 1.0 GeV/c to 4.0 GeV/c, and extrapolation was again performed for momentum below 1.0 GeV/c. A cut was applied at $\pm 3\sigma$

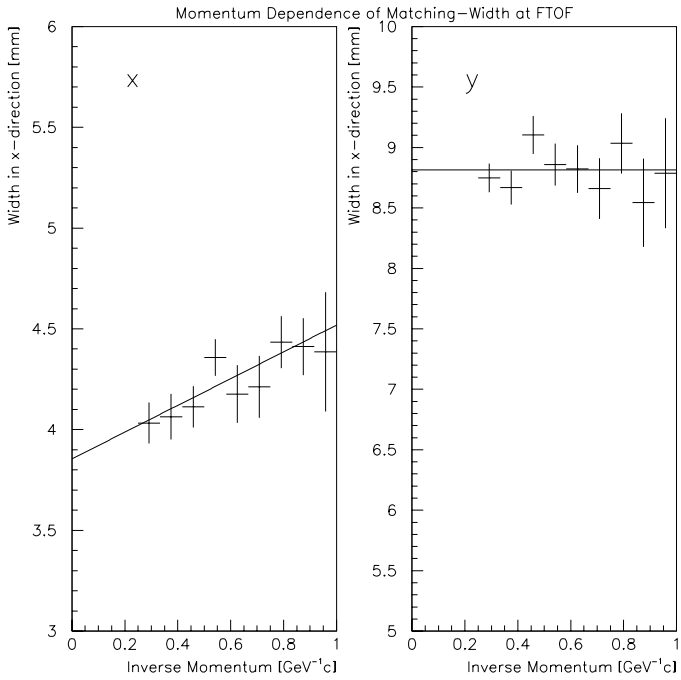

Figure 4.3.7: The r.m.s. width of position matching at the time-of-flight wall in a 12 degree run, as a function of momentum. Left: the x-direction. Right: the y-direction.

determined from the data at 6 degrees, in the both x- and y-directions. If more than one hit was found on FTOF within the cut, the one closest to the track projection was selected.

To assure that the associated hit was originated from a charged hadron, not from a γ-ray or a δ-ray, a cut was applied on the energy deposit in the wall, *i.e.* the normalized ADC value a_{norm} which was defined as

$$a_{norm} \equiv \sqrt{\frac{a^{top} - a_0^{top}}{g^{top}} \cdot \frac{a^{bot} - a_0^{bot}}{g^{bot}}}\ , \tag{4.3.5}$$

where a^i, a_0^i, and g^i are the ADC value, the ADC pedestal, and the gain of the channel, respectively, with $i = top$ or bot representing one of the two photo-multiplier tubes on the slat. A distribution of a_{norm} in a 12 degree run, as well as the applied cut, is shown in Figure 4.3.8. The typical fraction of hits rejected by the cut was ~ 5 %.

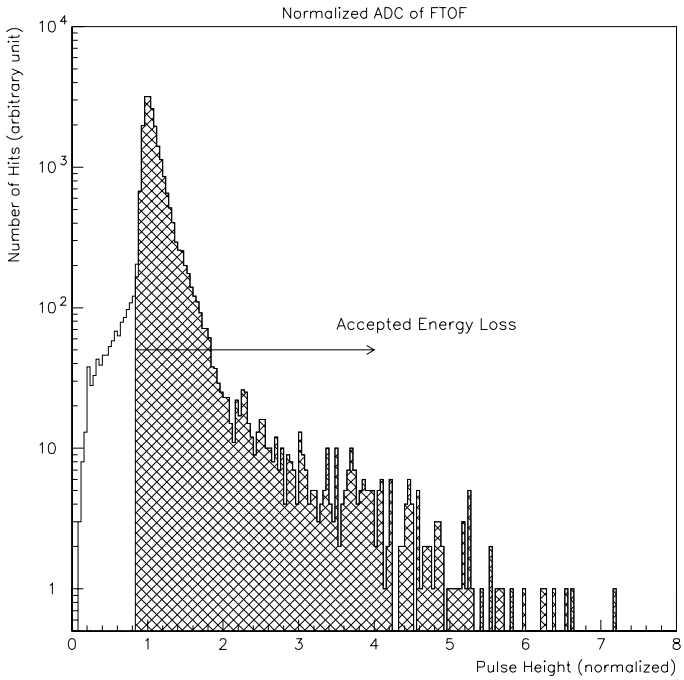

Figure 4.3.8: Distribution of normalized ADC of the time-of-flight wall in a 12 degree run. The hatched area represents the applied cut.

4.4 Momentum Determination

The momentum of a FS track was calculated with a field map of FM2. The y-(main) component of the magnetic field was integrated along the z-axis, and was stored in a table as a function of x- and y-positions. For each reconstructed track, its x- and y-positions were sampled near the entrance and the exit of FM2, and the field integration was calculated from the table by linear interpolation. The momentum kick in the x-direction dp_x was calculated from the average of the two field integration $\langle \int B_y dl \rangle$ [T · m] as

$$dp_x = \mp 0.2998 \cdot \langle \int B_y dl \rangle \ [\mathrm{GeV}/c] \ , \tag{4.4.1}$$

where the negative and positive signs apply to positively and negatively charged particles, respectively. The signed momentum of the particle p was then calculated as

$$p = \frac{dp_x}{u_x^{out} - u_x^{in}} \ , \tag{4.4.2}$$

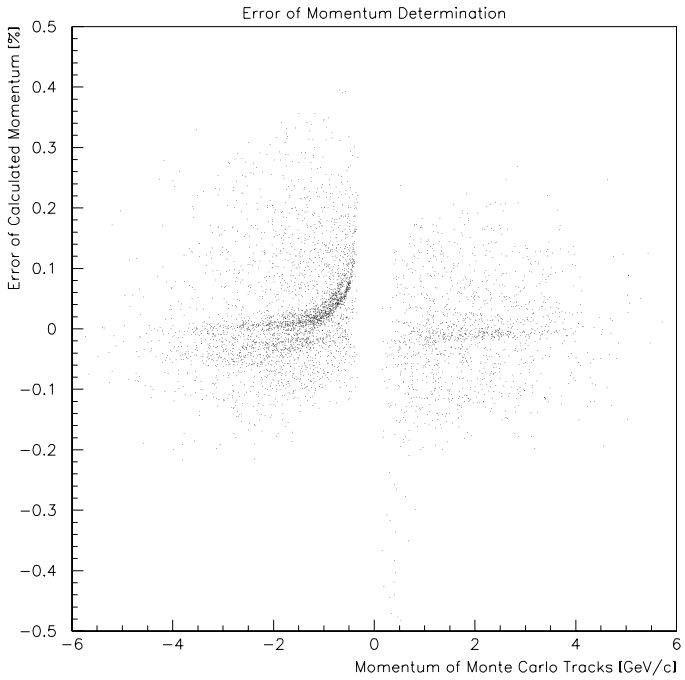

Figure 4.4.1: The error of the momentum determination with Monte Carlo tracks [63].

where u_x^{in} and u_x^{out} are the x-components of the direction (unit) vectors of the track segments before and after FM2, respectively. Error of the calculation was studied with Monte Carlo tracks [63], and the result is shown in Figure 4.4.1 as a function of momentum. The error associated with the method of momentum determination was assured be to less than 0.2 %, which was negligibly small compared to the intrinsic momentum resolution of the tracking system (see Section 4.5).

4.5 Particle Identification

A discussion on the particle identification criteria is presented in this section, as well as the basic algorithm of the procedure. Particular emphasis is laid on the experimental resolution of mass measurement and its contributing factors.

4.5.1 Algorithm

The species of a particle was identified by its squared mass m^2, calculated from a combination of measurement with the tracking system and with the time-of-flight system as

$$m^2 = p^2 \left\{ \left(\frac{TOF}{L} \right)^2 - 1 \right\} , \tag{4.5.1}$$

where p is the measured momentum, TOF is the time of flight, and L is the flight-path length determined from the tracking information.

Figure 4.5.1 shows a scatter plot of measured squared mass versus signed momentum in a 12 degree run. The applied particle identification cuts, which are described in the following subsections, are also shown in the figure.

4.5.2 Mass Resolution

A discussion is presented below on the resolution of mass measurement, as an important factor in determination of criteria for particle identification. From the experimental mass resolution, we estimated each of the contributing factors, including the angular resolution of the spectrometer and the time-of-flight resolution. By the formalization of the mass resolution, the applicable range of the particle-identification method can be extended, for instance to higher momentum regions or to rare particles such as antiprotons.

4.5.2.1 Contributing Factors

The experimental resolution of mass measurement was determined by following two factors: the momentum resolution of the tracking system and the timing resolution of the time-of-flight system. The momentum resolution σ_p was limited by the intrinsic angular resolution of the tracking system and multiple scattering of the particles, and was evaluated [64] as

$$\left(\frac{\sigma_p}{p} \right)^2 = (c_1 p)^2 + \left(\frac{c_2}{\beta} \right)^2 \tag{4.5.2}$$

$$c_1 = \frac{\sigma_\theta}{0.30 \int B dl} \tag{4.5.3}$$

$$c_2 = \frac{0.014 Z}{0.30 \int B dl} \sqrt{\frac{x}{L_r}} \left(1 + 0.038 \ln \frac{x}{L_r} \right) \tag{4.5.4}$$

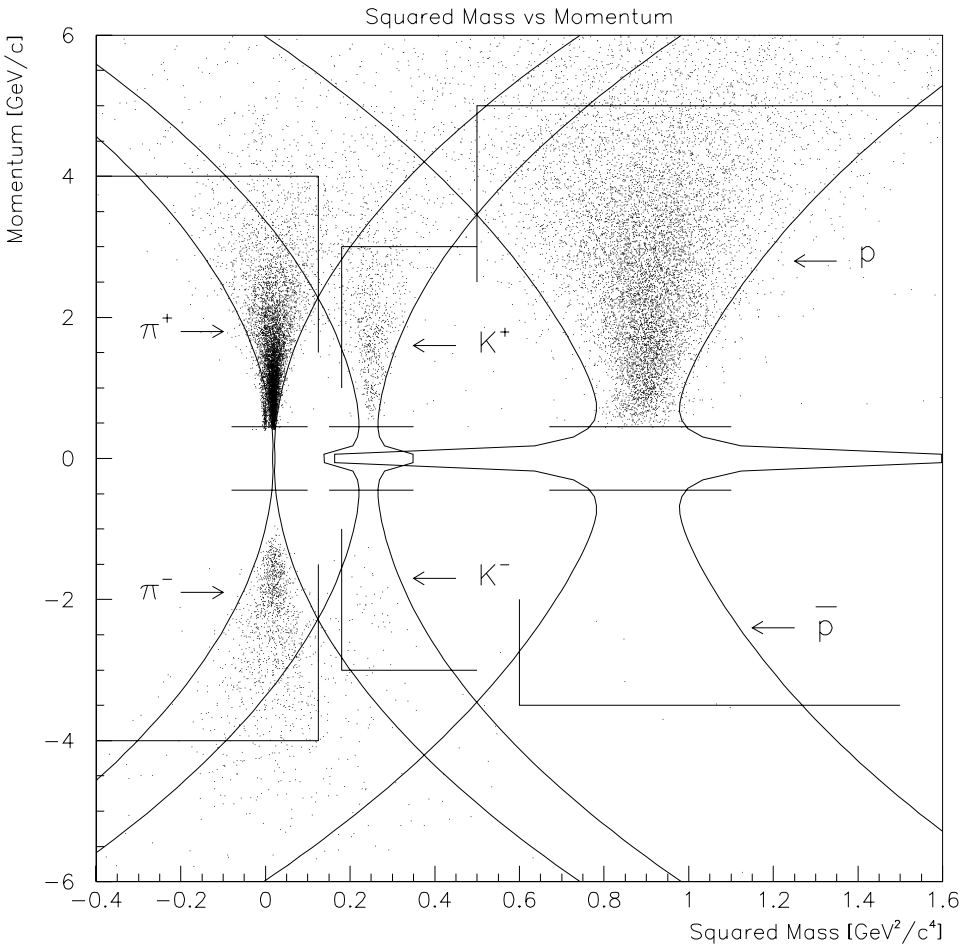

Figure 4.5.1: A scatter plot of measured squared mass versus signed momentum in a 12 degree run. See text for a description on the particle identification cuts indicated by solid lines.

where

p : momentum of the particle [GeV/c]
β : velocity of the particle (in unit of c)
Z : charge of the particle (in unit of e)
σ_θ : intrinsic angular resolution
$\int Bdl$: bending power of FM2 [T · m]
x/L_r : amount of material (in unit of radiation length),

and c_1 and c_2 represent the contributions of the angular resolution and multiple scattering, respectively.

Furthermore, assuming the time-of-flight resolution and the flight-path length to be nearly constant, the resolution of squared mass σ_{m^2} was unfolded as a function of momentum in a form of

$$\sigma_{m^2}^2 = 4m^2 \left(\frac{\sigma_p}{p}\right)^2 + \frac{4p^4}{\beta^2}\left(\frac{\sigma_{TOF}}{L}\right)^2 \quad (4.5.5)$$

$$= 4m^2p^2 \cdot c_1^2 + 4m^2\left(1 + \frac{m^2}{p^2}\right) \cdot c_2^2 + 4p^2\left(m^2 + p^2\right) \cdot c_3^2 \quad (4.5.6)$$

$$c_3 = \frac{\sigma_{TOF}}{L}\ , \quad (4.5.7)$$

where

m : mass of the particle
σ_{TOF} : time-of-flight resolution
L : flight-path length,

and c_3 represents the contribution of the time-of-flight resolution.

4.5.2.2 Effect of Multiple Scattering

As discussed above, the three factors determining the mass resolution, *i.e.* the angular resolution, the effect of multiple scattering, and the time-of-flight resolution, can in principle be deconvoluted from the momentum dependence of the mass resolution using real data. Fitting of the mass resolution as a function of momentum was although insensitive to the effect of multiple scattering, since the

acceptance did not include the very low momentum region where multiple scattering becomes a dominant factor. For this reason, the effect of multiple scattering was evaluated from the amount of material in the Forward Spectrometer, rather than from fitting the data. The material in the tracking chambers is summarized in Tables 4.5.1 and 4.5.2. Since the measured angles of a track in front of and behind FM2 roughly reflect the angles of the particle trajectory at the center of the two tracking chamber complexes, the amount of material from the center of TPC1 to the center of TPC2 was considered for the evaluation. As is summarized in Table 4.5.3, the amount was ~ 1.20 % in total; from Equation 4.5.4, the coefficient c_2 was evaluated to be

$$c_2 \simeq 1.05 \times 10^{-2} \tag{4.5.8}$$

for particles with $Z = 1$ and with the FM2 field at 0.4 T.

4.5.2.3 Momentum and Time-of-Flight Resolution

Figure 4.5.2 shows the experimental resolution of squared mass σ_{m^2} in a 12 degree run, as a function of momentum. The dashed lines in the figure indicate the result of least χ^2 fitting to Equation 4.5.6 with two free parameters, c_1 and c_3, which represent the angular resolution and the time-of-flight resolution, respectively; the coefficient c_2 was fixed at the value in Equation 4.5.8.

The results of fitting are listed in Table 4.5.4 for various spectrometer angle settings. The values of the coefficients at the 21 degree setting correspond to the angular resolution σ_θ and the time-of-flight resolution σ_{TOF} of

$$\sigma_\theta = 1.8 \times 10^{-3} \tag{4.5.9}$$

$$\sigma_{TOF} = 77 \text{ psec} , \tag{4.5.10}$$

and to the momentum resolution σ_p of 1.8 % for pions at 1.0 GeV/c, and 2.1 % for protons at the same momentum. The obtained time-of-flight resolution was consistent with the evaluation using high momentum pions (74 psec; see Section 4.2). It was also found that the angular resolution became worse at the forward angles; the time-of-flight resolution also showed a dependence, but to a slight degree. They could be regarded as effects of a high particle-density condition, such as mis-association of hits on the tracking chambers.

Chamber	Material	Average Thickness x [cm]	Radiation Length L_r [cm]	x/L_r [%]
TPC1	Argon-Isobutane (75:25)	35.2	12040	0.292
	Mylar Windows	0.0019	28.7	0.005
	Kapton Films	0.0050	~ 25	0.020
	Cu Foils	0.0006	1.43	0.042
	Paste	0.005	~ 40	0.013
	Cu-Be Wires	0.00026	1.46	0.018
	Subtotal			0.39
TPC2	Argon-Isobutane (75:25)	45.0	12040	0.374
	Mylar Windows	0.0025	28.7	0.009
	Kapton Films	0.0050	~ 25	0.020
	Cu Foils	0.0006	1.43	0.042
	Paste	0.005	~ 40	0.013
	Cu-Be Wires	0.00020	1.46	0.013
	Subtotal			0.47
Grand Total				0.86

Table 4.5.1: The material in the time projection chambers.

Chamber	Material	Average Thickness x [cm]	Radiation Length L_r [cm]	x/L_r [%]
FT2	Argon-Isobutane (50:50)	4.00	13320	0.030
	Al Windows	0.0051	8.89	0.057
	Mylar Foils	0.0070	28.7	0.024
	W-Au Wires	0.00014	3.50	0.004
	Subtotal			0.12
FT3	Argon-Isobutane (50:50)	5.52	13320	0.041
	Al Windows	0.0051	8.89	0.057
	Mylar Foils	0.0064	28.7	0.022
	W-Au Wires	0.00009	3.50	0.003
	Subtotal			0.12
FT4	Argon-Isobutane (50:50)	5.52	13320	0.041
	Al Windows	0.0051	8.89	0.057
	Mylar Foils	0.0064	28.7	0.022
	W-Au Wires	0.0007	3.50	0.002
	Subtotal			0.12
Grand Total				0.36

Table 4.5.2: The material in the drift chambers.

Material	Average Thickness x [cm]	Radiation Length L_r [cm]	x/L_r [%]
TPC1 (1/2)			0.20
Air	6.2	30420	0.02
FT2			0.12
Air	146.3	30420	0.48
FT3			0.12
Air	5.5	30420	0.02
TPC2 (1/2)			0.24
Total			1.20

Table 4.5.3: The material in the Forward Spectrometer from the center of TPC1 to the center of TPC2.

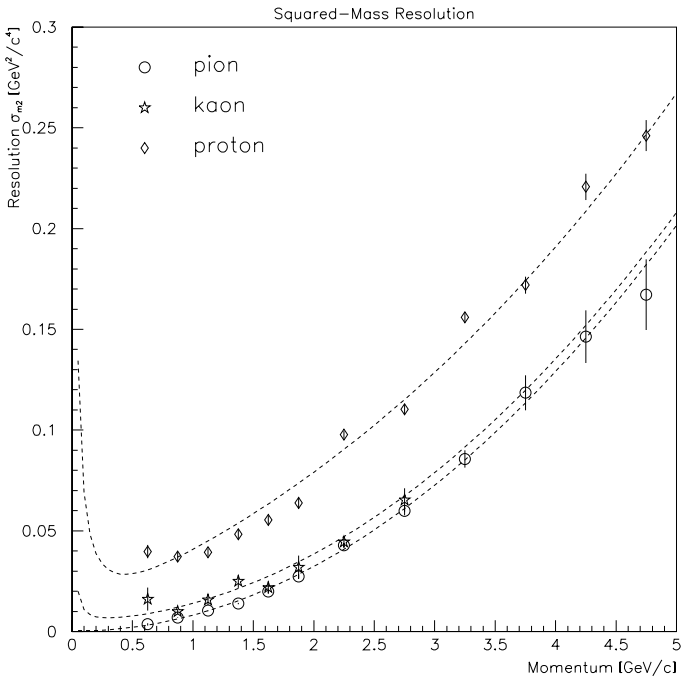

Figure 4.5.2: The experimental resolution of squared mass in a 12 degree run, as a function of momentum. Dashed lines indicate the result of fitting with two free parameters. See text for details.

Spectrometer Angle	c_1	c_3
6 degrees	$(2.61 \pm 0.04) \times 10^{-2}$	$(4.51 \pm 0.04) \times 10^{-3}$
9 degrees	$(2.17 \pm 0.03) \times 10^{-2}$	$(4.35 \pm 0.04) \times 10^{-3}$
12 degrees	$(1.93 \pm 0.03) \times 10^{-2}$	$(4.03 \pm 0.04) \times 10^{-3}$
15 degrees	$(1.76 \pm 0.03) \times 10^{-2}$	$(3.96 \pm 0.04) \times 10^{-3}$
18 degrees	$(1.59 \pm 0.05) \times 10^{-2}$	$(4.14 \pm 0.07) \times 10^{-3}$
21 degrees	$(1.50 \pm 0.04) \times 10^{-2}$	$(3.86 \pm 0.06) \times 10^{-3}$

Table 4.5.4: The angular and time-of-flight resolution estimated from the momentum dependence of the squared-mass resolution; c_1 represents the former factor, and c_3 the latter. The listed errors are only statistical. See text for a description.

4.5.3 Cut Criteria

Particle identification was performed using the squared-mass resolution σ_{m^2}, which was parameterized in the previous subsection as a function of momentum; the basic criterion to identify a particle was a relation:

$$\left| m^2_{cal} - m^2_0 \right| \quad < \quad 2.5 \; \sigma_{m^2} \; , \tag{4.5.11}$$

where m^2_{cal} denotes the squared mass calculated from the momentum and the time of flight, and m_0 is the real mass of the particle species. The cut is displayed in Figure 4.5.1 with curved lines.

Figure 4.5.3 shows plots of the measured squared mass with momentum slices, in a 12 degree run. In the momentum range from 1.5 GeV/c to 2.0 GeV/c (upper plot), pions, kaons, and protons were well separated with more than $\pm 2.5 \; \sigma_{m^2}$. In the range from 2.5 GeV/c to 3.0 GeV/c (lower), however, kaons could be, for example, substantially contaminated by pions. An additional cut was hence applied on m^2_{cal}, so that contamination by other particle species was to be eliminated. Moreover in higher momentum regions, particles with a less yield tend to be buried in the tail of more yielded particles. Considering the effect, a cutoff of the highest momentum was determined for each particle species from the data, at 4.0 GeV/c for pions ($\pi^{\pm}$), at 3.0 GeV/c for kaons ($K^{\pm}$), at 5.0 GeV/c for protons, and at 3.5 GeV/c for antiprotons. These additional particle-identification cuts

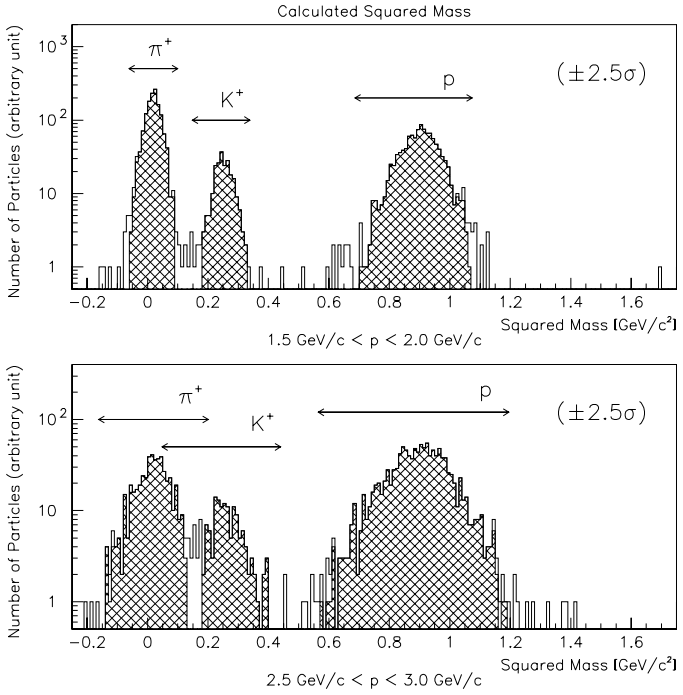

Figure 4.5.3: Distributions of calculated squared mass m^2_{cal} with momentum slices; in a 12 degree run with a polarity favoring positive particles. Upper: from 1.5 GeV/c to 2.0 GeV/c. Lower: from 2.5 GeV/c to 3.0 GeV/c. The arrows indicate the primary particle-identification cut ($m^2_0 \pm 2.5\sigma_{m^2}$). The hatched areas represent identified particles.

are also indicated in Figure 4.5.1 with straight lines.

With these cuts, the contamination by π^+ in K^+ was evaluated to be less than 3 % at the highest analyzed momentum, except for the most forward spectrometer setting at 6 degrees where it reached ~ 6 %. For pions and protons, the contamination by other particle species was less than 1 %. The contamination was treated as a systematic error; all the systematic errors related to the analysis procedure are listed and summarized in Section 5.7.

4.6 Corrections

In this section, we summarize the corrections related to the data reduction procedure. The corrections discussed here were used in evaluation of the particle

production cross sections, which is described in Section 5.5.

4.6.1 Tracking Efficiency

The efficiency of track reconstruction ϵ_{track} was estimated as the product of four independent terms, as:

$$\epsilon_{track} \equiv \epsilon_{cham} \cdot \epsilon_{TOF} \cdot \epsilon_{recon} \cdot \epsilon_{multi} \tag{4.6.1}$$

where

ϵ_{cham}	:	detection efficiency of the tracking chambers
ϵ_{TOF}	:	detection efficiency of the time-of-flight wall
ϵ_{recon}	:	reconstruction (software) efficiency for single particle
ϵ_{multi}	:	multiplicity dependence of reconstruction efficiency.

A discussion follows on each of these terms.

4.6.1.1 Tracking Chambers (ϵ_{cham})

Since the track reconstruction started from the two time projection chambers, tracks which we failed to find in one of them would never be recovered in the later stages of the analysis. Inefficiency of the time projection chambers was hence important to be studied. It was found from the data that the efficiency of the time projection chambers was not uniform over their entire active areas; it changed with the x-position due to different particle densities, and with the y-position due to electron diffusion and absorption during drift. Angle settings of the Forward Spectrometer and the beam intensity may also affect the efficiency. The efficiency of each row of the time projection chambers was evaluated with tracks reconstructed using the other five rows of the chamber, as a function of the x- and y-positions, on a run-by-run basis. The total tracking efficiency of the chamber was estimated from the efficiency per row by a simple calculation of combinations. For example for TPC1, we required four rows out of six to be fired as mentioned in Section 4.3. Then the tracking efficiency ϵ_{TPC1} was expressed as

$$\epsilon_{TPC1} = {}_6C_6 \cdot \epsilon_{row}^6 + {}_6C_5 \cdot \epsilon_{row}^5(1-\epsilon_{row}) + {}_6C_4 \cdot \epsilon_{row}^4(1-\epsilon_{row})^2 \tag{4.6.2}$$

where ϵ_{row} is the efficiency per row of the chamber.

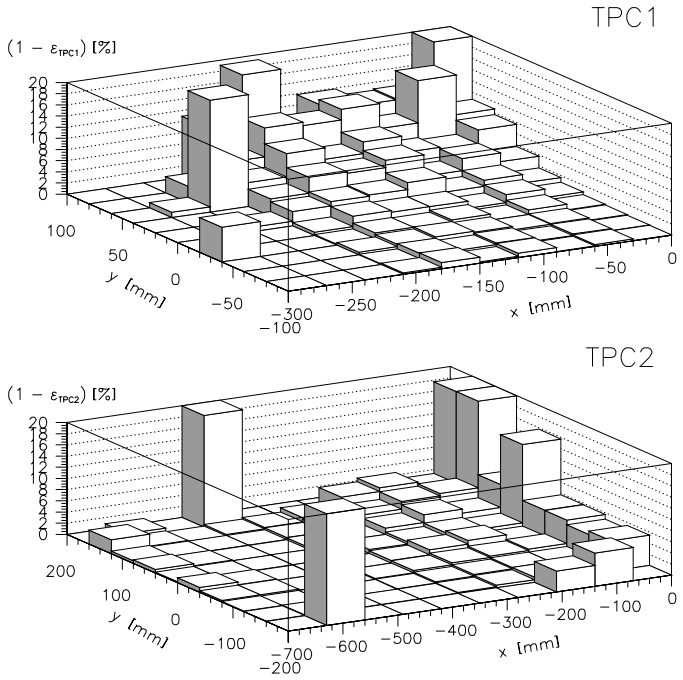

Figure 4.6.1: Maps of the tracking efficiency of the time projection chambers; in a 12 degree run, and as a function of the x- and y-positions. The statistical errors are large at the edges.

Efficiency maps of the time projection chambers in a 12 degree run are shown in Figure 4.6.1. Note that the statistical errors are large at the edges of the effective areas. A dependence of the efficiency on the x- and y-positions can be seen in the figure.

Contribution of the drift chambers to the tracking inefficiency was very small ($\ll 1$ %), since the numbers of planes required for tracking were set small enough (see Section 4.3) considering the detection efficiency of the chambers (91 – 92 % per plane as presented in Section 4.2). The total tracking efficiency of the chamber system $\epsilon_{chamber}$ was hence evaluated as

$$\epsilon_{cham} \;=\; \epsilon_{TPC1} \cdot \epsilon_{TPC2} \;. \tag{4.6.3}$$

4.6.1.2 Time-of-Flight Wall (ϵ_{TOF})

Since the readout modules used for the time-of-flight wall did not have multi-hit capability, second (or later) particles hitting a slat in an event could not be

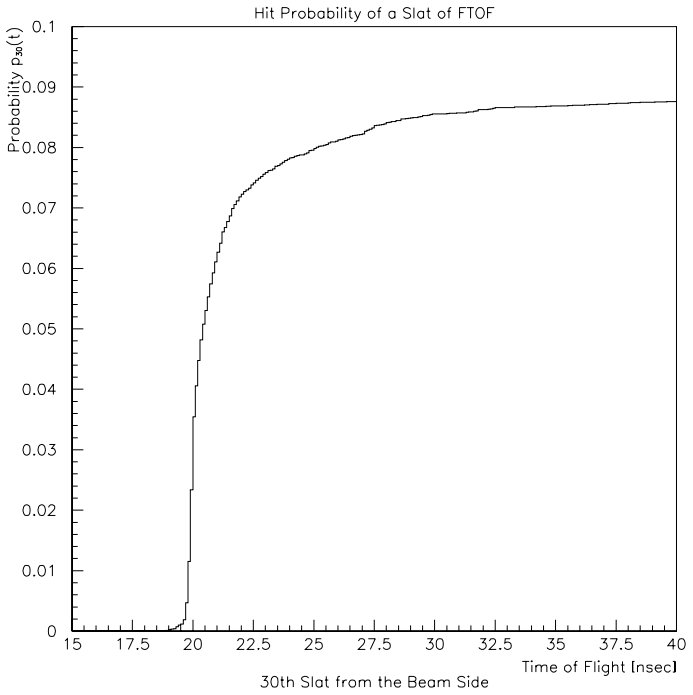

Figure 4.6.2: Time-integrated hit probability of a slat of the time-of-flight wall as a function of time of flight; for $\overline{ZCAL}$ events in a 12 degree run.

recorded. That resulted in inefficiency for slow particles, *e.g.* protons, especially in high multiplicity events. The effect was evaluated from the data as a function of the slat number and timing, on a run-by-run basis and for each trigger type; the detection efficiency ϵ_{TOF} of slat i at time t was estimated to be

$$\epsilon_{TOF} \;=\; 1 - p_i(t) \;, \tag{4.6.4}$$

where $p_i(t)$ is a trigger-type-dependent probability that the slat had been hit by another particle by the time t. Figure 4.6.2 shows the time-integrated hit probability of a slat (the 30th counted from the beam side) $p_{30}(t)$ as a function of the time of flight, for $\overline{ZCAL}$ events in a 12 degree run.

Distribution of the detection efficiency ϵ_{TOF} for protons is shown in Figure 4.6.3 as a function of the slat number, in a 12 degree run with a polarity setting favoring positively charged particles. Smaller slat numbers correspond to the beam side, where the particle density was higher and particles with higher momenta were preferred.

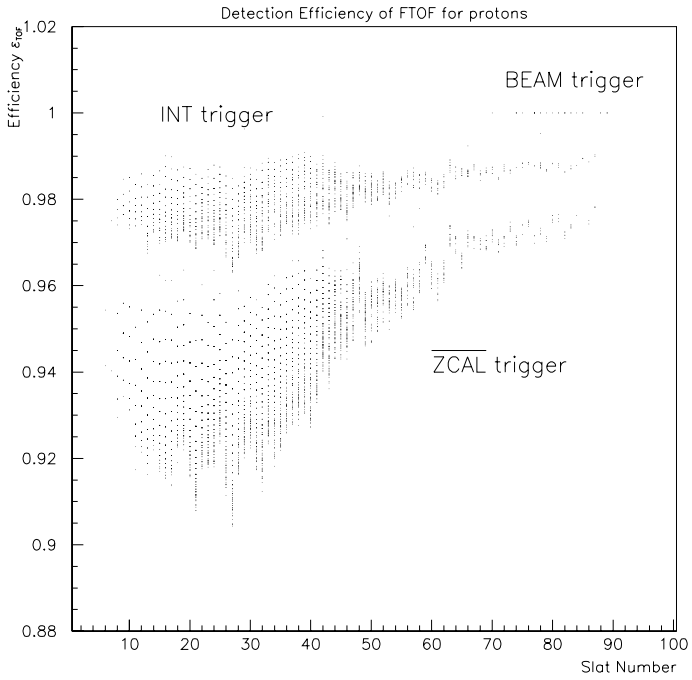

Figure 4.6.3: The estimated detection efficiency of the time-of-flight wall for protons; in a 12 degree run with a polarity setting favoring positive particles. Each point represents a detected proton. The abscissa is the slat number; smaller slat numbers correspond to the beam side.

4.6.1.3 Particle and Momentum Dependence (ϵ_{recon})

The efficiency of the track reconstruction routine may drop in the low momentum region mainly due to multiple scattering, even though the various cut criteria were determined as a function of momentum (Section 4.3).

The effect was evaluated with a Monte Carlo study, for each particle species and as a function of momentum. With a pion, a kaon, or a proton, 2×10^5 each single track events were generated and tracked using the GEANT simulation package* [65] with the energy loss and multiple scattering switches on, but without decay; particle decay in flight is discussed in one of the following subsections, as an independent effect. Track reconstruction was performed assuming all the detectors had detection efficiency of 100 %. The ratio of reconstructed tracks to those geometrically accepted represented the efficiency of the tracking

*Version 3.15 of the simulation code was used for Monte Carlo studies in this thesis.

routine. Figure 4.6.4 shows the efficiency ϵ_{recon} for pions, kaons, and protons, as a function of inverse momentum p^{-1}. The solid lines in the figure indicate fitting to an empirical approximation function with two free parameters p_0 and a:

$$\epsilon_{recon} \simeq \begin{cases} 1 & (|p| \geq p_0) \\ 1 - a \cdot \left(|p|^{-1} - p_0^{-1} \right)^2 & (|p| < p_0) \ . \end{cases} \tag{4.6.5}$$

Efficiency for pions and kaons was consistent to each other within the statistical error, staying constant above 0.5 GeV/c, while efficiency for protons had a tendency to drop below 1.0 GeV/c. The analytical behavior of the efficiency justified the nature of the cuts applied in the tracking procedure.

To avoid a large systematic error resulting from a correction for the efficiency, a cutoff of the lowest momentum was set at 450 MeV/c for those particle species. In conjunction with the particle-identification limit at high momentum (Section 4.5), the momentum range of the analysis was thus limited from 450 MeV/c to 4.0 GeV/c for pions, from 450 MeV/c to 3.0 GeV/c for kaons, and from 450 MeV/c to 5.0 GeV/c for protons. The momentum cutoffs were taken into account in the acceptance calculation (see Section 5.5).

4.6.1.4 Multiplicity Dependence (ϵ_{multi})

In the previous subsection, the efficiency of track reconstruction was discussed with single track events. Under a high particle-density condition, an additional fraction of tracks may be lost due to confusion in the tracking routine. A Monte Carlo study was performed to estimate the effect.

With two different spectrometer settings, at 6 degrees and at 21 degrees, we generated 2×10^5 particles each, with a simple kinematic parameterization simulating central Au+Au collisions at the AGS energy[†], and prepared data sets with different multiplicity by merging the events. Since the effect of multi-hits on the time-of-flight wall was treated as an independent correction, association of FTOF was not required in this study; the number of particles successfully reconstructed with the tracking chambers was counted for each data set, and compared to that from single track events. The track reconstruction again assumed 100 % detection efficiency of all the detectors.

[†]The parameterization and the yield ratio of various hadrons were based on a preliminary result from the Henry Higgins spectrometer on particle production in the Au+Au collisions [66, 67].

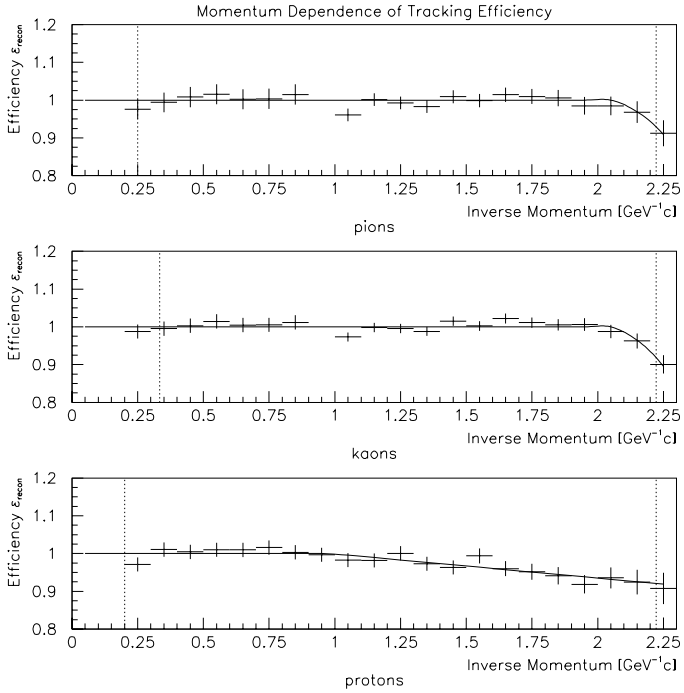

Figure 4.6.4: The momentum dependence of the tracking efficiency for pions (upper), kaons (middle), and protons (lower) estimated by a Monte Carlo study. The dotted lines indicate the momentum cutoffs of analysis for each particle species.

The effect was notable in the high momentum region, while particles with low momenta were spread out by the two bending magnets and were less affected. Figure 4.6.5 shows the estimated multiplicity-dependent term of the tracking efficiency $\epsilon_{multi}(N, p)$ as a function of momentum p, with the Forward Spectrometer at 6 degrees and an average multiplicity N of 10.4. As shown in the figure, the term was then approximated as

$$\epsilon_{multi}(N, p) \simeq 1 - a(N) \cdot |p| \tag{4.6.6}$$

where coefficient $a(N)$ is a function of multiplicity N. The values of $a(N)$ agreed within 20 % for the two angle settings, as shown in Figure 4.6.6, and were approximated in a form of

$$a(N) \simeq a_0 \cdot N\sqrt{N-1} \tag{4.6.7}$$

with a constant a_0. The value of a_0 was determined by fitting the data set

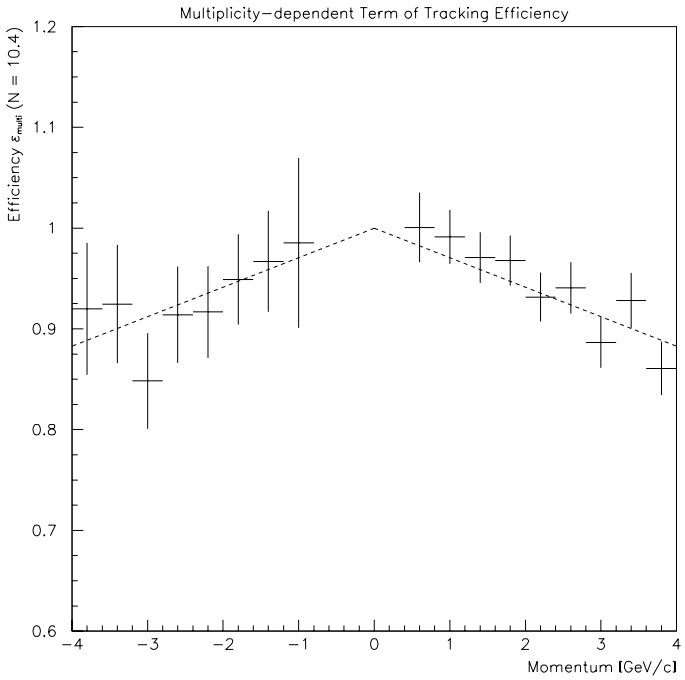

Figure 4.6.5: The multiplicity-dependent term of the tracking efficiency estimated by a Monte Carlo study as a function of momentum. With an average multiplicity N of 10.4, and the spectrometer at 6 degrees.

at 6 degrees to Equation 4.6.7, since very high particle multiplicity was to be observed only at the forward angles. As the result, the multiplicity-dependent term ϵ_{multi} of the track reconstruction efficiency was written as

$$\epsilon_{multi}(N,p) \simeq 1 - a_0 \cdot N\sqrt{N-1} \cdot |p| \quad (4.6.8)$$

$$a_0 = (9.1 \pm 1.0) \times 10^{-4} \ , \quad (4.6.9)$$

and was used for a correction. The error of the approximation was included in the systematic errors summarized in Section 5.7.

4.6.2 Decay in Flight

Particle decay in flight in the spectrometer must also be corrected. Due to the finite resolution of the spectrometer, a fraction of particles having decayed may be reconstructed and may not be distinguished from their original particle species, especially in the high momentum region where Lorentz boost is dominant for

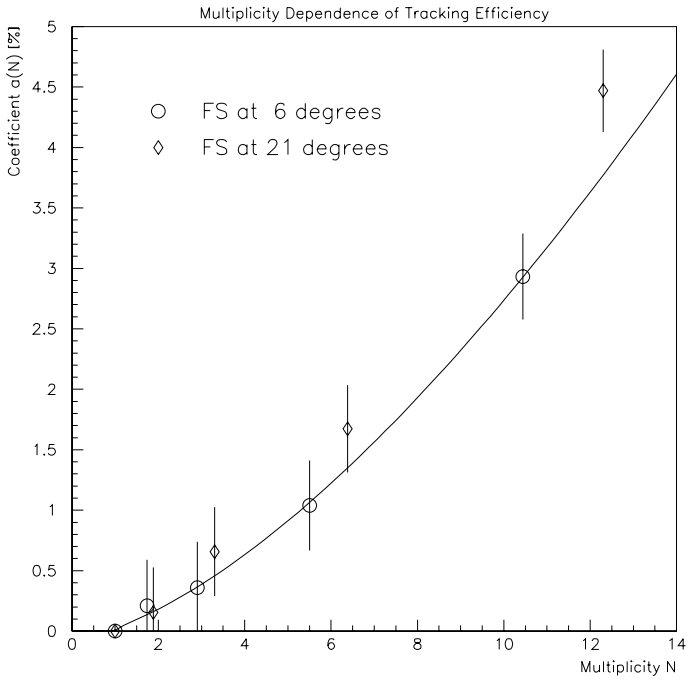

Figure 4.6.6: The multiplicity dependence of the tracking efficiency, with the Forward Spectrometer at 6 degrees and at 21 degrees, estimated by a Monte Carlo study. See text for the definition of $a(N)$. Solid line is a result of fitting to the 6 degree data.

kinematics of the decay products. The effect of decay on the tracking efficiency was evaluated with a Monte Carlo simulation. For each of pions and kaons, 1×10^5 single track events were generated and tracked with and without decay using the GEANT. Reconstructed and correctly identified particles were counted, and a ratio of the numbers was taken with and without decay, to evaluate the effect on the tracking efficiency.

Figure 4.6.7 shows the result for pions and kaons. Since the main decay branches of kaons ($K^{\pm} \to \mu^{\pm}\nu$, $\pi^{\pm}\pi^0$, 3π, or $\pi^0 l^{\pm}\nu$) have large Q-values, kaons having decayed were well distinguished; we hence used the survival rate of kaons calculated from the flight-path length L and momentum p, not the fitting result of the Monte Carlo study, as the tracking efficiency $\epsilon_{decay}(K)$, *i.e.*

$$\epsilon_{decay}(K) \;=\; \exp\left(-\frac{m_K L}{\tau_K p}\right) \;, \qquad (4.6.10)$$

where m_K and τ_K are the mass and the lifetime of charged kaons, respectively. The small Q-value of pion decay ($\pi^{\pm} \to \mu^{\pm}\nu$), on the other hand, allowed a considerable fraction of pions having decayed to be reconstructed and *identified* still as pions. Accordingly, decay in flight of pions was corrected with the evaluated tracking efficiency, which was

$$\epsilon_{decay}(\pi) \;=\; \max\left[\exp\left(0.0196 - \frac{0.0140L}{p}\right),\ 1\right] \ , \qquad (4.6.11)$$

where L is the flight-path length of the pion in unit of [m], and p is its momentum in [GeV/c].

4.6.3 Particle Identification Efficiency

Since the particle-identification cuts were determined from the data themselves (see Section 4.5), it was possible to evaluate at what level particles were discarded as *not identified*, or were contaminated by other particle species.

The efficiency of particle identification ϵ_{PID} was evaluated using a Gaussian approximation as

$$\epsilon_{PID} \;=\; \int_{m^2_{min}}^{m^2_{max}} \frac{1}{\sqrt{2\pi}\sigma_{m^2}} \exp\left\{-\frac{(m^2 - m_0^2)^2}{2\sigma_{m^2}}\right\} dm^2 \ , \qquad (4.6.12)$$

where m_0 is the real mass of the particle, σ_{m^2} is the momentum-dependent resolution of squared mass m^2, and m^2_{min} and m^2_{max} are the momentum-dependent cut values on m^2. On the other hand, the contamination by other particle species was evaluated to be at most 1 % for pions and protons, and 3 % for kaons (6 % at the 6 degree setting), as noted in Section 4.5.

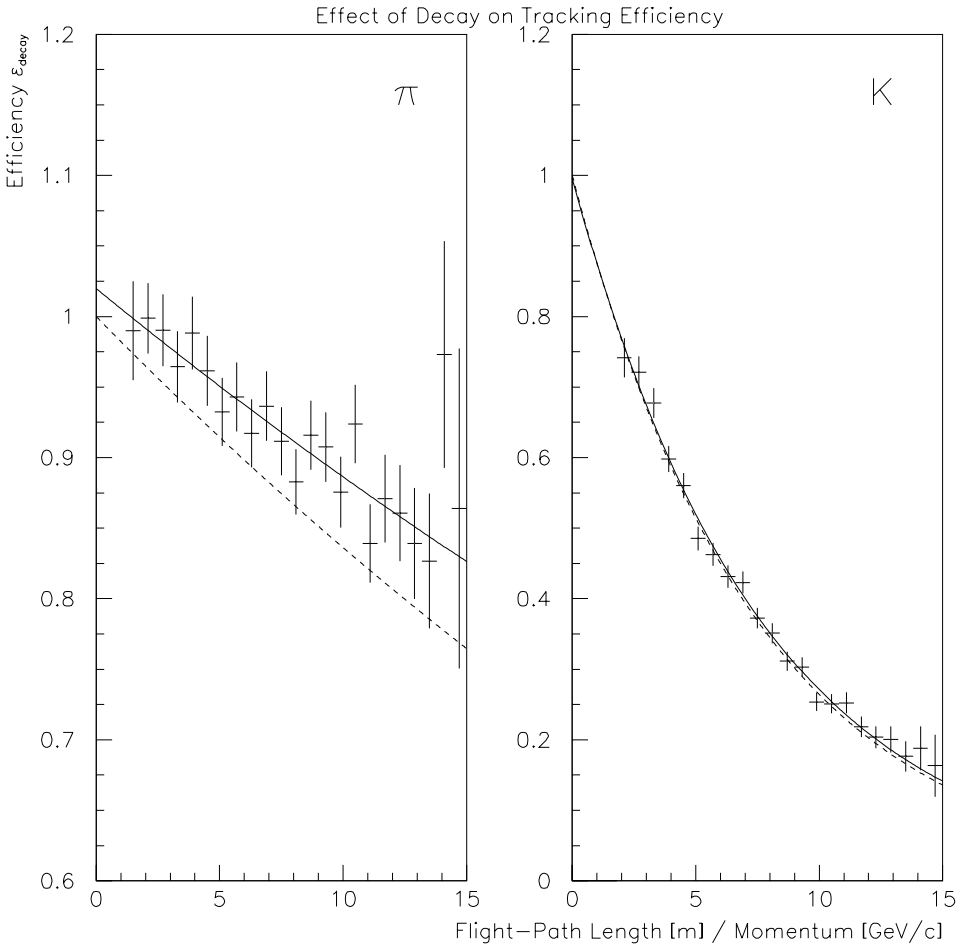

Figure 4.6.7: The effect of decay in flight on the tracking efficiency estimated by a Monte Carlo study. The ordinate is the ratio of numbers of particles which were reconstructed and correctly identified in Monte Carlo simulations with and without decay. Left: pions. Right: kaons. Solid lines are results of exponential fitting. Dashed lines represent the survival rate of the particles.

Chapter 5

Data Analysis II — Cross Section Evaluation

5.1 Overview

In the first half of this chapter, the procedure of evaluation of the particle production cross sections is described. First, the definition of the interaction trigger cross section is given in Section 5.2. Sections 5.3 and 5.4 give accounts of incorporation of other subsystems than the Forward Spectrometer into the analysis; the former is on the event selection with the beam counters, and the latter describes the applied centrality cut utilizing the zero-degree calorimeter. The way to evaluate the invariant cross sections of particle production is presented in Section 5.5.

The systematics of the analysis is discussed in Sections 5.6 – 5.8. Section 5.6 shows an examination of the systematics with kinematic reflections; Section 5.7 summarizes various systematic errors in the analysis; the internal consistency of the analysis is checked using Monte Carlo data in Section 5.8.

5.2 Interaction Trigger Cross Section

The trigger cross section σ_{trig} of the interaction (INT) trigger was defined as

$$\sigma_{trig} \equiv \left(\frac{S_{trig} N_{trig}}{N_{beam}} - \frac{S^{bg}_{trig} N^{bg}_{trig}}{N^{bg}_{beam}} \right) \frac{10^{24} A}{N_A D} \text{ [barn]} , \qquad (5.2.1)$$

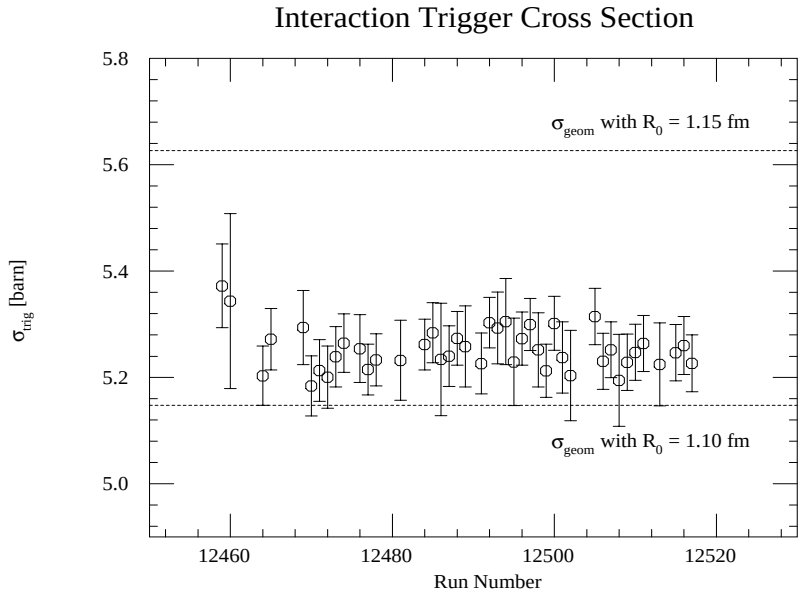

Figure 5.2.1: The interaction trigger cross section as a function of the run number. The error bars indicate the statistical errors only. Two dashed lines indicate geometrical cross sections calculated with a parameter $R_0 =$ 1.15 fm and 1.10 fm (see text).

where

N_{beam}	:	number of beam particles
N_{beam}^{bg}	:	number of beam particles with empty target
N_{trig}	:	number of triggers
N_{trig}^{bg}	:	number of triggers with empty target
S_{trig}	:	scale-down factor
S_{trig}^{bg}	:	scale-down factor with empty target
A	:	mass of the target nuclei [amu = g/mol]
N_A	:	Avogadro's number = 6.02×10^{23} [mol^{-1}]
D	:	target thickness [g/cm^2] ,

subtracting the background contributions such as originating from interactions of beam particles with the beam counters and so forth. Figure 5.2.1 shows the interaction trigger cross section as a function of the run number.

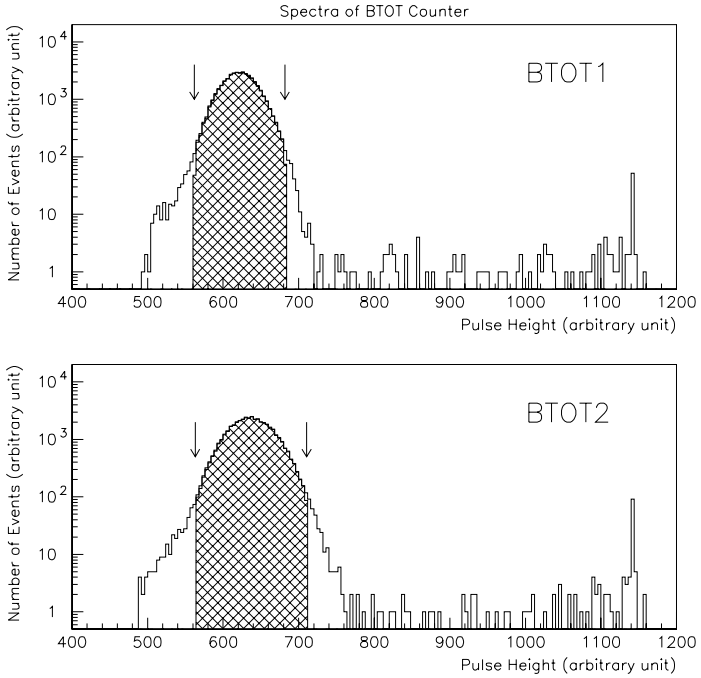

Figure 5.3.1: ADC spectra of the beam defining counter, BTOT. The two figures correspond to the two photo-multiplier tubes on the both sides of the counter. The hatched areas represent *good* beam events (see text); the cuts applied for the ADC's are indicated by arrows.

The geometrical cross section σ_{geom} of Au+Au collisions can be calculated as

$$\sigma_{geom} \quad = \quad \pi \left(2 \times \sqrt[3]{197} \cdot R_0 \right)^2 \tag{5.2.2}$$

with a parameter $R_0 \simeq 1.15$ fm. Values of σ_{geom} with $R_0 = 1.15$ fm and 1.10 fm are also indicated in Figure 5.2.1 as a reference.

5.3 Event Selection

To eliminate events with beam particles which interacted with the beam counters, gates were set in the software for the ADC's of the beam defining counter, BTOT, at $\pm 2.5\sigma$, where σ denotes the r.m.s. width of the ADC distribution. Figure 5.3.1 shows ADC spectra of BTOT as well as the applied gates.

The beam halo was rejected in the trigger logic by requiring anti-coincidence of the HOLE counter, but only using the analog sum of the two outputs of the

counter (Equation 3.4.1). To make sure all the halo particles to be rejected, we used the TDC information of the two photo-multiplier tubes on HOLE; only events with no valid TDC recorded were selected. The fraction of the events rejected by the cut was ~ 1 % of the total events.

5.4 Centrality Cut

The definitions of two types of semi-inclusive triggers, central and non-central, are described in this section. The triggers were defined in the software and used for the centrality cut applied in the analysis.

5.4.1 Central Trigger

We re-defined the central trigger in the software, since the hardware cut for the centrality of collisions could have been drifting with time. A software threshold (upper limit) was set for the energy deposit in ZCAL so as to adjust the trigger cross section to be 0.21 barn, corresponding to 4.0 % of the interaction cross section or the impact parameter less than 2.6 fm. Figure 5.4.1 shows spectra of ZCAL, taken with INT and $\overline{ZCAL}$ triggers; the applied software gate is also shown. The time dependence of the software threshold is shown in Figure 5.4.2 as a function of the run number. For the central trigger, the background contributions were evaluated to be less than 1 % with the empty target runs.

5.4.2 Non-Central Trigger

The non-central trigger was also defined similarly as the central trigger. A lower limit was set for the energy deposit in ZCAL in the software to the data taken with INT trigger, so as to reject central 0.50 barn of cross section (9.5 % of the interaction cross section), leaving events corresponding to the impact parameter larger than 4.0 fm. In evaluation of the trigger cross section, the background contributions were subtracted making use of the empty target runs, in the same way as for the interaction trigger (Section 5.2).

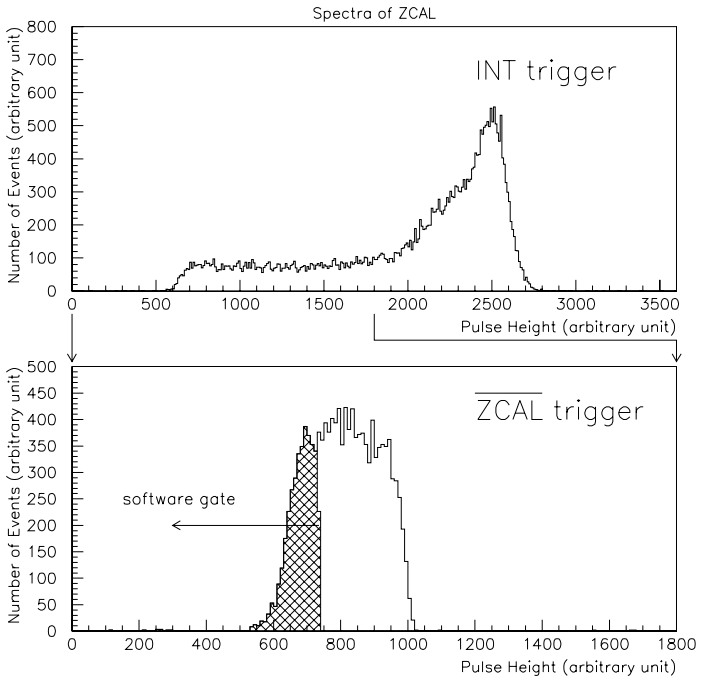

Figure 5.4.1: ADC spectra of the zero-degree calorimeter taken with INT (upper) and $\overline{ZCAL}$ (lower) triggers. Note different horizontal scales. The hatched area represents the software gate for the centrality cut at 0.21 barn.

5.5 Invariant Cross Sections

Cross section σ of particle production can be written in a Lorentz invariant form:

$$E\frac{d^3\sigma}{dp^3} = \frac{d^3\sigma}{p_t dp_t dy d\phi} = \frac{d^3\sigma}{m_t dm_t dy d\phi} \tag{5.5.1}$$

with transverse momentum p_t or transverse mass m_t ($= \sqrt{m_0^2 + p_t^2}$), where m_0, p, E, y, and ϕ are the rest mass, momentum, total energy, rapidity, and azimuthal angle of the particle, respectively. The invariant cross section was evaluated for each particle species in bins of rapidity and transverse momentum, as

$$E\frac{d^3\sigma}{dp^3} = \frac{S_{trig}N_i(y,p_t)}{N_{beam}} \cdot \frac{10^{24}A}{N_A D} \cdot \frac{1}{\epsilon} \cdot \frac{1}{p_t \Delta y \Delta p_t \Delta\phi_i(y,p_t)} \ [\text{barn} \cdot \text{GeV}^{-2}\text{c}^3] \ , \tag{5.5.2}$$

where S_{trig}, N_{beam}, A, N_A, and D are as defined in Section 5.2, and

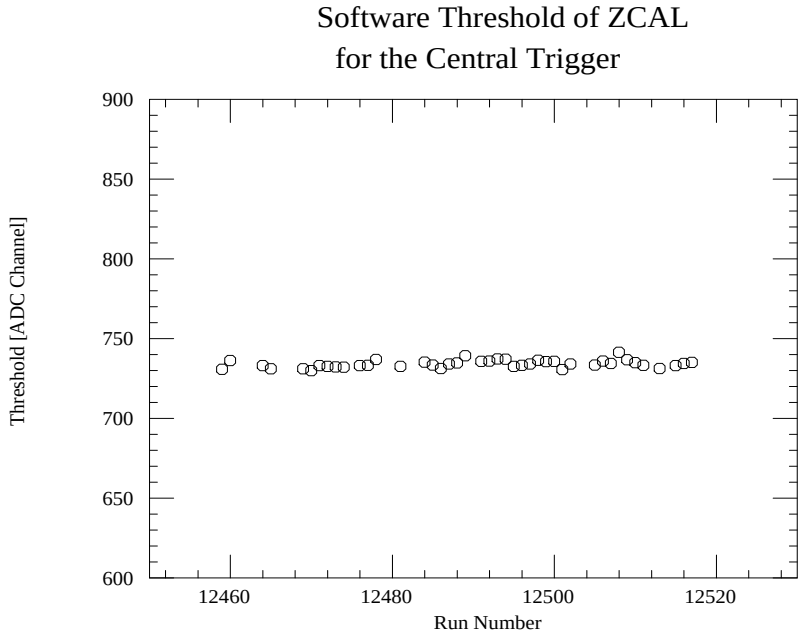

Figure 5.4.2: The software threshold of the zero-degree calorimeter for the central trigger, as a function of the run number. The ordinate corresponds to the abscissa of Figure 5.4.1.

$N_i(y, p_t)$	:	number of particles ($i = \pi^{\pm}$, $K^{\pm}$, p, $\overline{p}$, d, $\cdots$)
ϵ	:	total analysis efficiency
Δy	:	bin size in rapidity
Δp_t	:	bin size in transverse momentum
$\Delta\phi_i(y, p_t)$	:	azimuthal acceptance.

The total analysis efficiency ϵ was defined as

$$\epsilon \equiv \epsilon_{track} \cdot \epsilon_{decay} \cdot \epsilon_{PID} \tag{5.5.3}$$

where ϵ_{track}, ϵ_{decay}, and ϵ_{PID} are the efficiency factors for tracking, for decay in flight, and for particle identification, respectively, which are discussed in Section 4.6. Invariant differential yield per trigger was also defines as

$$E\frac{d^3\sigma}{dp^3}\Big/\sigma_{trig} = \frac{N_i}{N_{trig}} \cdot \frac{1}{\epsilon} \cdot \frac{1}{p_t \Delta y \Delta p_t \Delta\phi_i(y, p_t)} \tag{5.5.4}$$

to compare data with different centrality cuts.

Particle	Lower Cutoff [GeV/c]	Higher Cutoff [GeV/c]
$\pi^{\pm}$	0.45	4.0
$K^{\pm}$	0.45	3.0
p	0.45	5.0
$\overline{\mathrm{p}}$	0.45	3.5

Table 5.5.1: The analyzed momentum ranges for various particle species. For descriptions on the cutoffs, see Sections 4.5 and 4.6.

In the analysis, the unit bin size was taken to be

$$\Delta y = 0.05 \tag{5.5.5}$$

$$\Delta p_t = 0.025 \text{ [GeV/}c\text{]} . \tag{5.5.6}$$

Geometrical acceptance was calculated for each y-p_t bin by a Monte Carlo method. Around the spectrometer aperture, 2×10^6 particles of both charges were generated and tracked using the GEANT with all the physical interactions off. In heavy materials such as the collimator or the frames of the tracking chambers, any particle was forced to stop there. From the number of particles which passed through all detectors from FT2 to FTOF*, the geometrical acceptance $\Delta\phi/2\pi$ was calculated as a function of momentum and polar emission angle with respect to the incident beam; it was then converted to a function of rapidity and transverse momentum for each particle species. The fiducial cut (Section 4.3) and the momentum cutoffs (Sections 4.5 and 4.6) were included in the calculation. Table 5.5.1 summarizes the analyzed momentum ranges for various particle species.

Figure 5.5.1 shows examples of the acceptance maps, for pions at the 6 degree setting. It also shows the statistical errors associated with the calculation of the maps; bins at the edges of the acceptance with statistical errors larger than 5 % were rejected.

Overlaps of kinematic coverages between different spectrometer settings (angle and/or polarity) were treated by averaging the cross sections in the overlapping bins.

*Existence of dead slats of the time-of-flight wall was also taken into account.

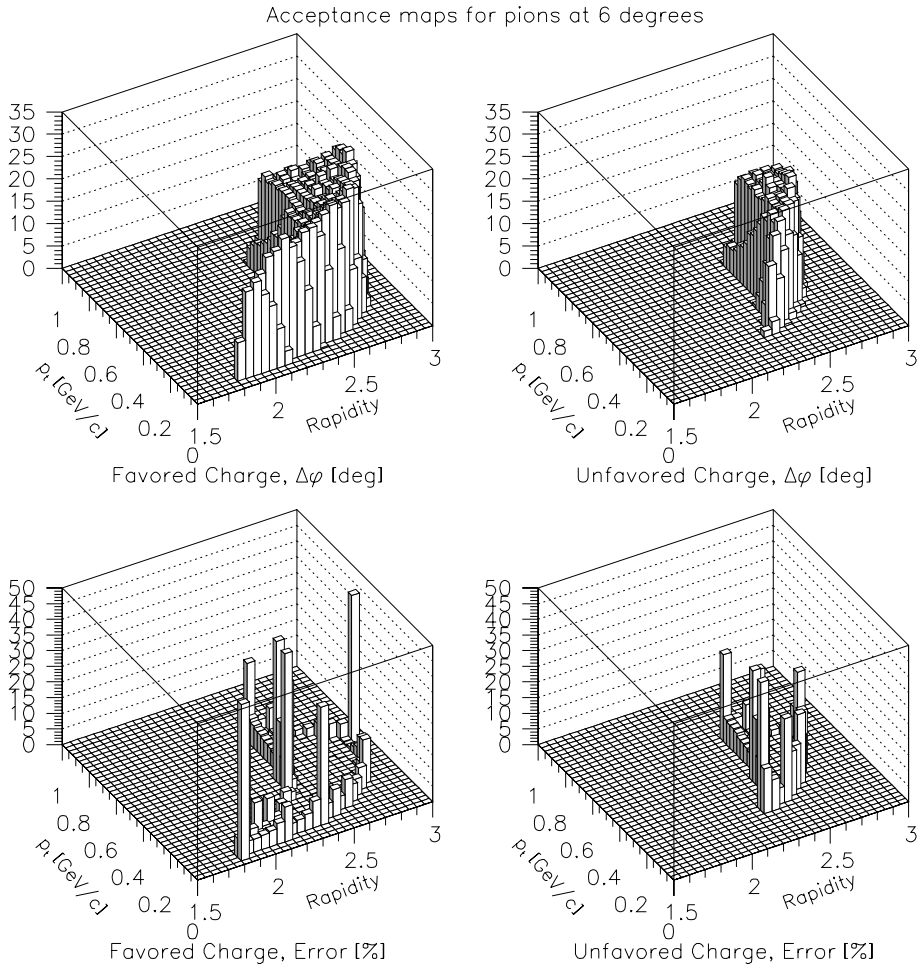

Figure 5.5.1: Samples of acceptance maps; pions at the 6 degree setting.

5.6 Systematics Examination

The systematics of the analysis was examined utilizing the kinematic symmetry of the collision system with respect to the center-of-mass rapidity y_{cm} ($\simeq 1.6$). Figure 5.6.1 shows ratios of invariant differential yields between kinematically reflected rapidity regions, as a function of transverse kinetic energy $(m_t - m_0)$ for positively charged kaons and protons*. To get enough statistics for the systematics examination, the centrality cut was applied at central 0.50 barn of cross section here, rather than 0.21 barn used to select central collision events in the analysis. The error bars in the figure indicate the statistical errors of the ratios. A systematic discrepancy of $\sim$ 10 % at most can be seen at the edges of the kinematic coverage. It was considered as a systematic error originating from the calculation of the geometrical acceptance, whose procedure is described in Section 5.5.

5.7 Summary of Systematic Errors

The applied corrections and the associated systematic errors in the analysis chain are listed in Table 5.7.1. The overall systematic error of the absolute values of particle yields and cross sections was estimated to be $\pm$ 10 %.

5.8 Consistency Examination with Monte Carlo Data

An extensive Monte Carlo study was performed to examine the systematics and the internal consistency of the analysis procedure. A data set was generated with a kinematic parameterization, and was processed through the entire analysis chain. The consistency between the original parameterization in the event generator and the obtained results of the analysis should be a good test of the systematics.

To simulate a central Au+Au collision, 800 particles including pions, kaons, protons, neutrons, and antiprotons were generated in solid angle of 4π. The

*Since the Forward Spectrometer covered only forward half of the rapidity regions for pions (see Section 6.1), they could not be used for the systematics examination.

Correction	Typical Correction	Systematic Error	Reference
Data Reduction			
Tracking Efficiency	0 – 10 %	± 3 %	Section 4.6
Decay in Flight			Section 4.6
$\pi^{\pm}$	0 – 18 %	± 1 %	
$K^{\pm}$	30 – 200 %	± 5 %	
Particle Identification	1 – 31 %	± 2 %	Section 4.6
Particle Misidentification			Section 4.5
Contamination in K^+	—	$^{+\ 3}_{-\ 0}$ %	*
Contamination in $\pi^{\pm}$, p	—	$^{+\ 1}_{-\ 0}$ %	
Cross Section Evaluation			
Target Thickness	—	± 2 %	Section 3.2
Empty-Target Subtraction			Section 5.4
Central Trigger	—	$^{+\ 0}_{-\ 1}$ %	
Non-Central Trigger	∼ 40 %	± 1 %	
Geometrical Acceptance	—	± 7 %	Section 5.5
Total		± 10 %	

Table 5.7.1: The applied corrections and the associated systematic errors in the analysis chain. The typical correction values listed were taken from a 12 degree run. * At the 6 degree setting, the contamination by π^+ in K^+ was estimated to be ∼ 6 %.

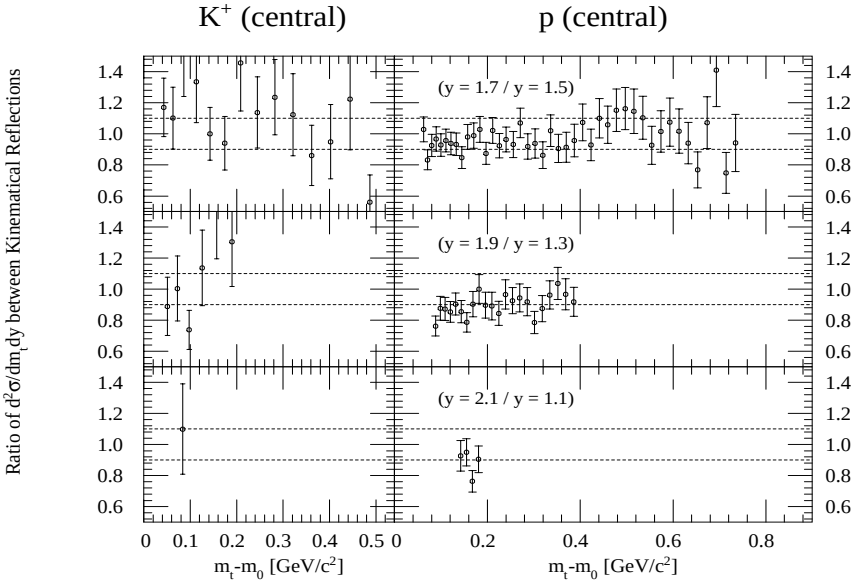

Figure 5.6.1: A systematics examination with kinematic reflections. Ratios of invariant differential yields between kinematically reflected rapidity (y) regions are shown for positively charged kaons (left) and for protons (right). Top: ratios between y = 1.7 and 1.5. Middle: between y = 1.9 and 1.3. Bottom: between y = 2.1 and 1.1. The dashed lines represent (100±10) % to guide an eye.

momentum and the emission angle of each particle were distributed with a simply parameterized function of rapidity y and transverse mass m_t, which is expressed as

$$\frac{d^2\sigma}{2\pi m_t dm_t dy} = A_0(y) \exp\left(-\frac{m_t - m_0}{T_0(y)}\right) \tag{5.8.1}$$

with two rapidity-dependent parameters $A_0(y)$ and $T_0(y)$*. The parameters for each particle species were determined based on a preliminary result from the Henry Higgins spectrometer on central Au+Au collisions [66, 67]. For each spectrometer angle and polarity setting used in the experiment (see Section 3.5), 5×10^3 central events were generated and tracked by a simulation code based on the GEANT. All the switches for physical interactions in the GEANT package

*A discussion on validity of the parameterization is given in Section 6.2.

were turned on, and the energy cutoffs were lowered[†] from the standard values to reproduce the background conditions.

The generated events were then converted into *data* files, taking the actual resolution and efficiency of the detectors into account. The analysis was performed in exactly the same way as done with the real data. As a sample of the results, the obtained transverse-mass spectra for charged pions, positively charged kaons, and protons in the rapidity range from 1.6 to 1.8 are shown in Figure 5.8.1, with the corresponding parameterization in the event generator. Finally, the transverse-mass spectra were fitted to Equation 5.8.1, and the rapidity density and the inverse slope parameter T_0 were calculated for each particle species and rapidity bin. Figure 5.8.2 shows the results for charged pions, charged kaons, and protons as a function of rapidity, comparing with the original parameterization. The results displayed a reasonable agreement within the statistical errors.

[†]The cutoff energies for tracking in the GEANT were set at 2.5 MeV for hadrons and neutral particles, and at 0.1 MeV for γ-rays and electrons.

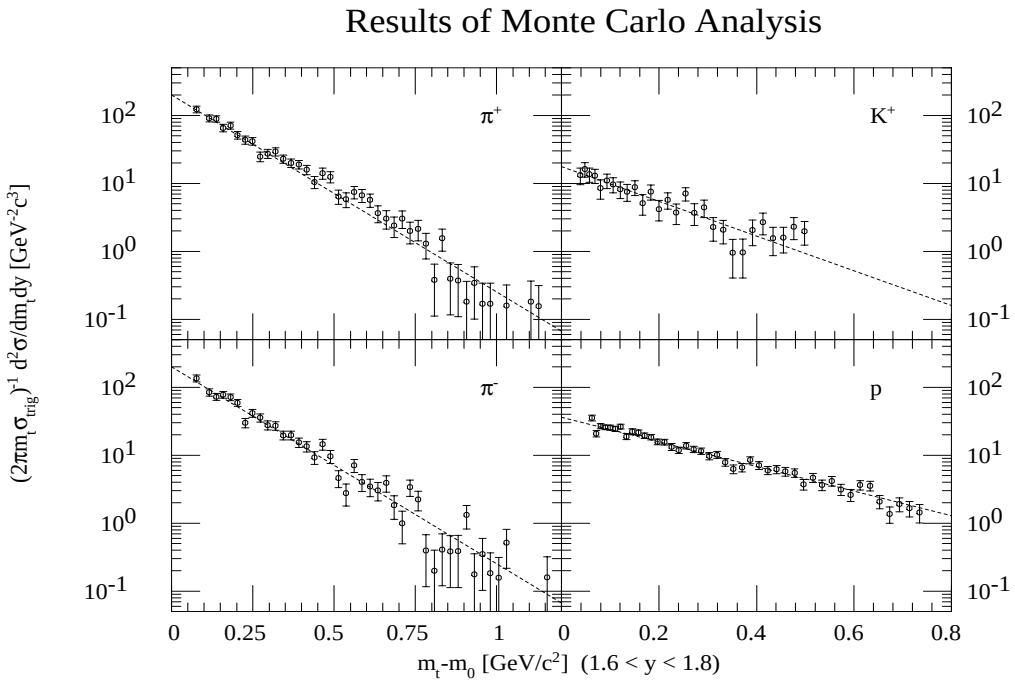

Figure 5.8.1: Transverse-mass spectra of charged pions ($\pi^{\pm}$), positively charged kaons (K^{+}), and protons in a Monte Carlo study. The rapidity range is from 1.6 to 1.8. The dashed lines indicate the parameterization in the event generator.

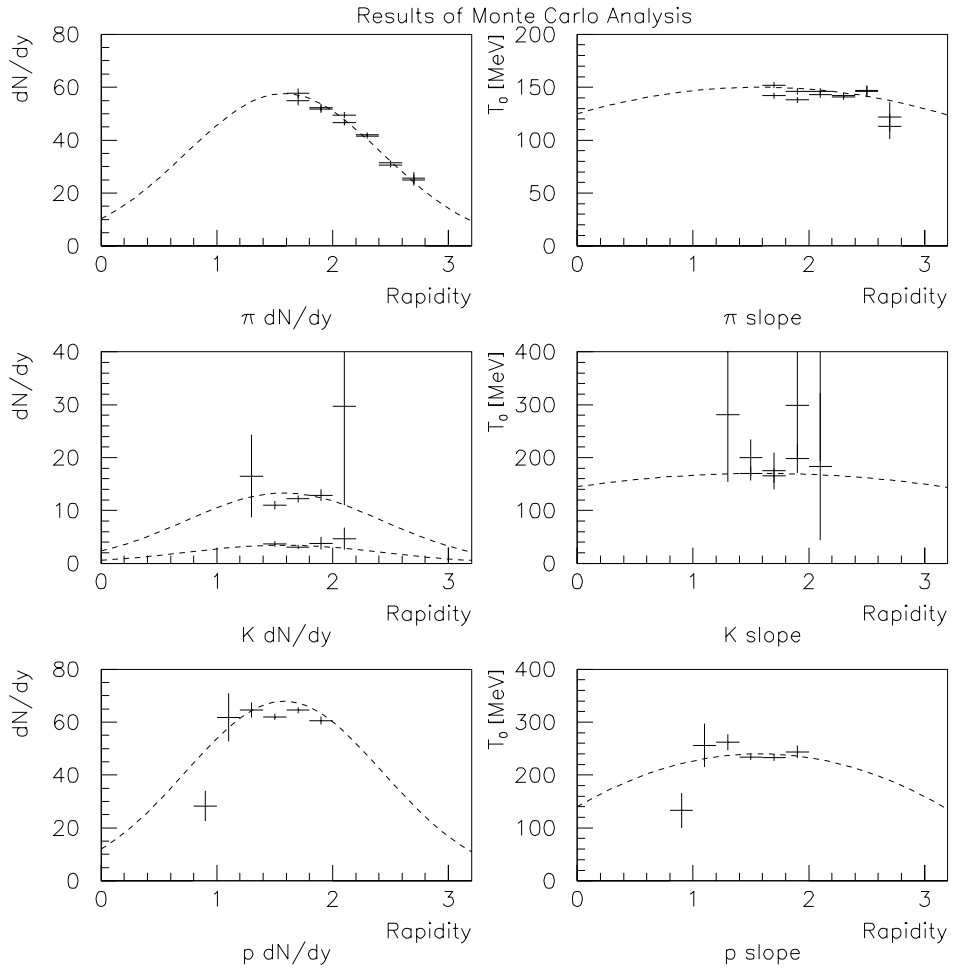

Figure 5.8.2: Rapidity densities dN/dy (left) and inverse slope parameters T_0 (right) of charged pions ($\pi^{\pm}$; top), charged kaons ($K^{\pm}$; middle), and protons (p ; bottom) in a Monte Carlo study as a function of rapidity. In the plot of yields of kaons (middle left), the upper and the lower points represent K^+ and K^-, respectively. The dashed lines display the parameterization in the event generator.

Chapter 6

Experimental Results

6.1 Overview

In this chapter, we present the experimental results from the analysis procedure described in Chapters 4 and 5, on production of charged pions ($\pi^{\pm}$), positively charged kaons (K^{+}), and protons. The analyzed data set covered kinematic regions shown in Figure 6.1.1 for those particle species.

The cross sections are presented as a function of transverse kinetic energy ($m_t - m_0$), motivated by a fact that production cross sections of secondary particles in p+p collisions are empirically known to be well described with transverse mass [68, 69], as

$$\frac{d\sigma^2}{2\pi m_t dm_t dy} = A_0 \exp\left(-\frac{m_t - m_0}{T_0}\right) , \qquad (6.1.1)$$

where A_0 is a normalization factor and T_0 is called the inverse slope parameter. The parameterization has also been confirmed to be applicable in p+A and A+A collisions [26, 28].

The semi-inclusive results from the central collision events are presented in Section 6.2, with discussions on the consistency with earlier data and on the parameterization. In Section 6.3, we present the results from the non-central collision events. As a further reference, the results of inclusive analysis are shown in Section 6.4.

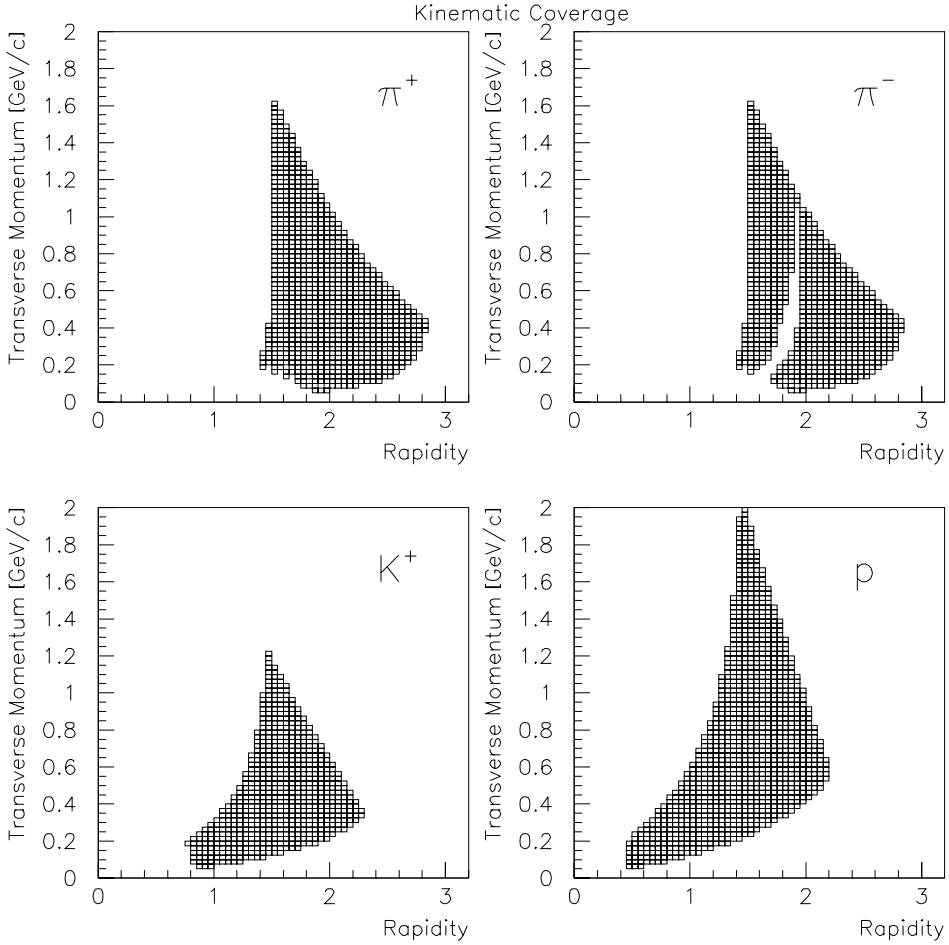

Figure 6.1.1: The kinematic coverages for $\pi^{\pm}$, K^+, and protons.

6.2 Central Collisions

In this section, we presented the experimental results from central Au+Au collisions at 11 A GeV/c. As described in Section 5.4, central 0.21 barn of cross section, corresponding to 4.0 % of the total interaction cross section, was selected. A discussion follows on the consistency of the results with earlier data from the Henry Higgins spectrometer. The parameterization used to evaluate the particle yields is also introduced in this section.

6.2.1 Transverse-Mass Spectra

Figures 6.2.1 and 6.2.2 show the invariant differential yields of $\pi^{\pm}$, K^{+}, and protons in central collisions of Au+Au at 11 A GeV/c, as a function of transverse kinetic energy. The top spectrum in each figure is displayed with the correct ordinate value, while the others are successively divided by a factor of 10. The error bars indicate the statistical errors only.

6.2.2 Consistency with Earlier Data

Here we compare the transverse-mass spectra with preliminary results from the Henry Higgins spectrometer. The comparison serves to examine the systematics of the analysis. It would also be allowed to extend the covered kinematic ranges by merging the two data sets, once the consistency is assured.

Figures 6.2.3 – 6.2.5 compare the invariant differential yields of $\pi^{\pm}$ and protons, measured with the Forward Spectrometer and with the Henry Higgins. The Henry Higgins data* were from preliminary analysis of the first Au beam runs at AGS in 1992 [66, 70]. In the same way as the analysis of the Forward Spectrometer data, a centrality cut was applied at 4.0 % of the total interaction cross section, utilizing the zero-degree calorimeter. In Figures 6.2.3 and 6.2.4, the pion data from the Henry Higgins are reflected with respect to the center-of-mass rapidity of 1.6. Protons are directly compared without reflection. Kaons could not be compared because of no overlapping rapidity region.

As seen in the figures, spectra of protons measured with the two spectrometers

*These data were presented at the Tenth International Conference on Ultra-Relativistic Nucleus-Nucleus Collisions (Quark Matter '93) at Bolänge, Sweden (1993).

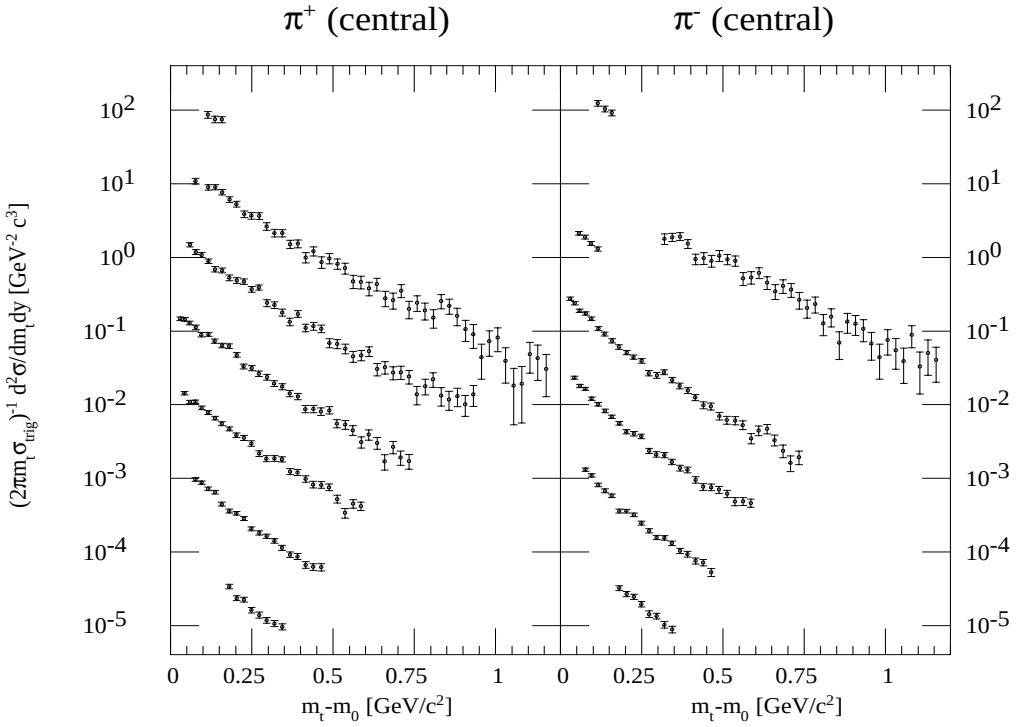

Figure 6.2.1: The invariant differential yields of $\pi^{\pm}$ in central (4 %) Au+Au collisions at 11 A GeV/c, as a function of transverse kinetic energy ($m_t - m_0$). The successive spectra are for different rapidity (y) bins, from $y = 1.5$ (top) to $y = 2.7$ (bottom) with intervals of 0.2. Each successive spectrum is divided by 10. The error bars indicate the statistical errors only.

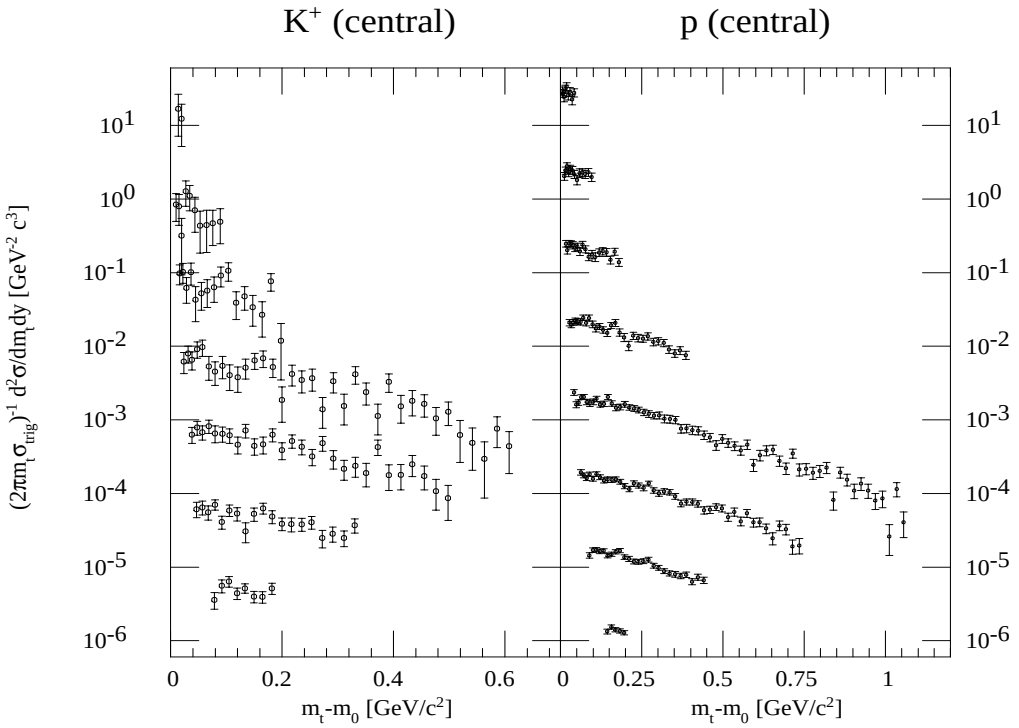

Figure 6.2.2: The invariant differential yields of K^+ and protons in central (4 %) Au+Au collisions at 11 A GeV/c, as a function of transverse kinetic energy ($m_t - m_0$). The successive spectra are for different rapidity (y) bins, from $y = 0.9$ (top) to $y = 2.1$ (bottom) for K^+ and from $y = 0.7$ (top) to $y = 2.1$ (bottom) for protons, with intervals of 0.2. Each successive spectrum is divided by 10. The error bars indicate the statistical errors only.

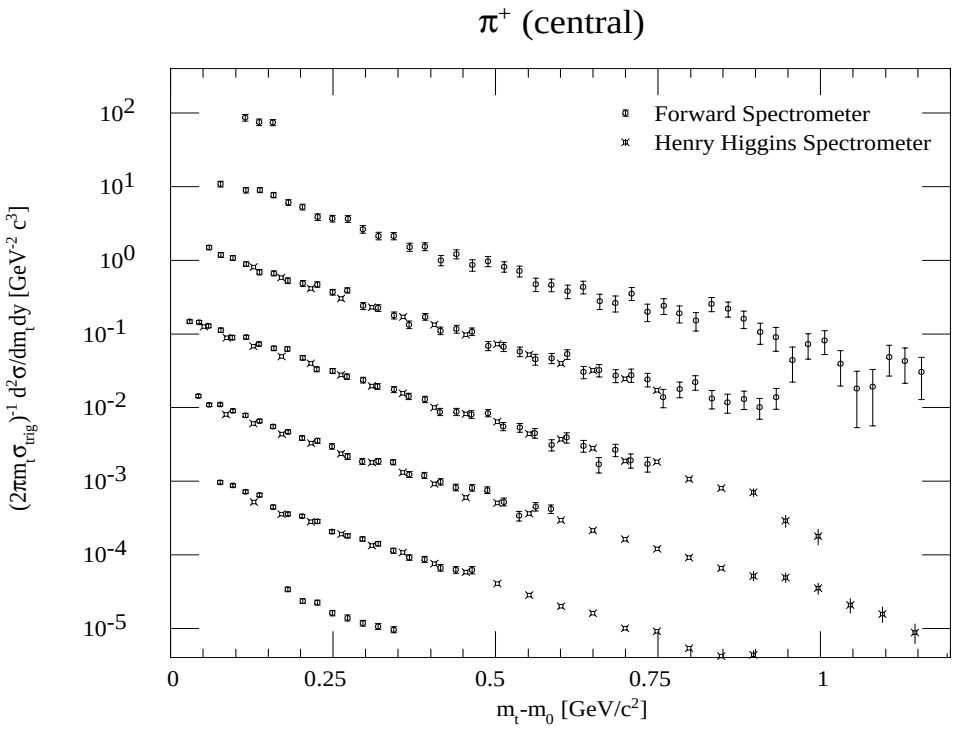

Figure 6.2.3: The invariant differential yield of π^+ measured with the two spectrometer arms; in central (4 %) Au+Au collisions at 11 A GeV/c and as a function of transverse kinetic energy ($m_t - m_0$). The successive spectra are for different rapidity (y) bins, from $y = 1.5$ (top) to $y = 2.7$ (bottom) for the Forward Spectrometer with intervals of 0.2. The data from the Henry Higgins are reflected with respect to $y_{cm} = 1.6$. Each successive spectrum is divided by 10. The error bars indicate the statistical errors only.

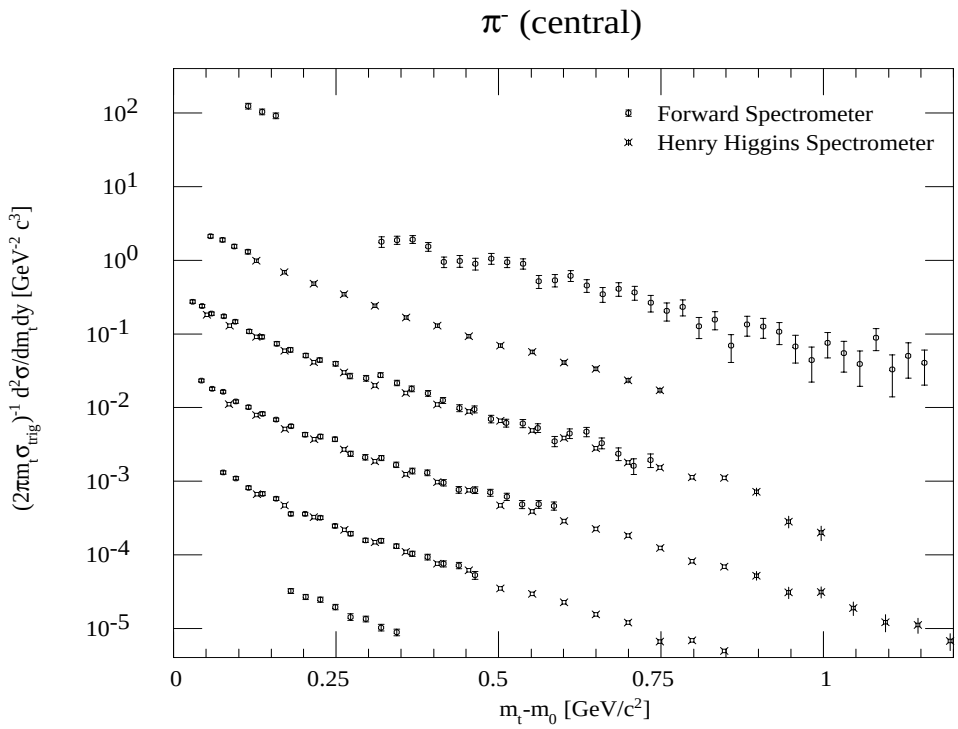

Figure 6.2.4: The invariant differential yield of π^- measured with the two spectrometer arms; in central (4 %) Au+Au collisions at 11 A GeV/c and as a function of transverse kinetic energy ($m_t - m_0$). The successive spectra are for different rapidity (y) bins, from $y = 1.5$ (top) to $y = 2.7$ (bottom) for the Forward Spectrometer with intervals of 0.2. The data from the Henry Higgins are reflected with respect to $y_{cm} = 1.6$. Each successive spectrum is divided by 10. The error bars indicate the statistical errors only.

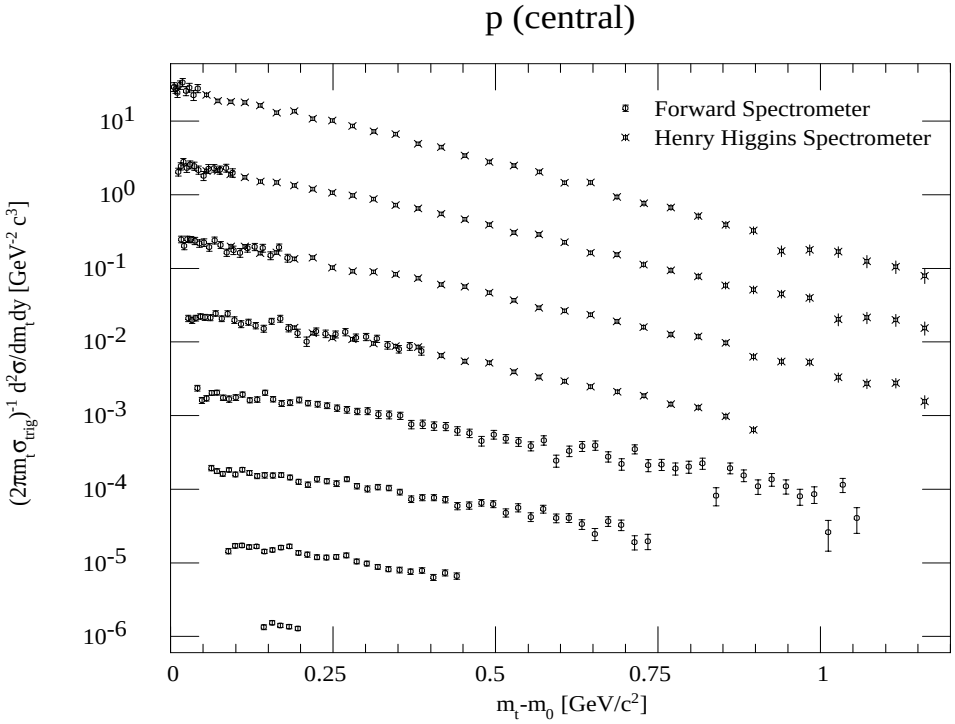

Figure 6.2.5: The invariant differential yield of protons measured with the two spectrometer arms; in central (4 %) Au+Au collisions at 11 A GeV/c and as a function of transverse kinetic energy ($m_t - m_0$). The successive spectra are for different rapidity (y) bins, from $y = 0.7$ (top) to $y = 2.1$ (bottom) with intervals of 0.2. Each successive spectrum is divided by 10. The error bars indicate the statistical errors only.

agreed with each other well within the statistical errors. A systematic discrepancy of $\sim$ 10 % was observed for $\pi^{\pm}$ at low transverse kinetic energies, while in most kinematic regions their spectra also showed a good agreement. Evaluation of the total yields and the inverse slope parameters of protons was performed based on the combined data set, being predicated on the consistency. A wider coverage thus obtained of transverse kinetic energy should lead to accordingly smaller systematic errors. On the other hand, the pion data from the Henry Higgins were not combined, to avoid systematic errors originating from the required kinematic reflection and from the discrepancy of the two data sets at the edges of the acceptance. The potential gain of kinematic coverage by combining the data sets was also smaller for pions.

6.2.3 Parameterization

The single-exponential parameterization (Equation 6.1.1) was found not to be suitable to describe the results for all particle species, as seen in Figures 6.2.1 and 6.2.2, especially for π^- and for protons. Discussions on the deviations from the single-exponential scaling, *i.e.* the enhancement of π^- and the suppression of protons in the low transverse-kinetic-energy regions, are presented in Chapter 7. To describe those spectra, an empirical parameterization was introduced with an enhancement/suppression factor w_D and a damping factor T_D:

$$\frac{d\sigma^2}{2\pi m_t dm_t dy} = A_1 \exp\left(-\frac{m_t - m_0}{T_1}\right)\left\{1 + w_D \exp\left(-\frac{m_t - m_0}{T_D}\right)\right\} \quad , \quad (6.2.1)$$

where A_1 and T_1 are the normalization factor and the inverse slope parameter of the main component, respectively. This parameterization could be equivalently rewritten as a double-exponential with the second set of parameters A_2 and T_2, as

$$\frac{d\sigma^2}{2\pi m_t dm_t dy} = A_1 \exp\left(-\frac{m_t - m_0}{T_1}\right) + A_2 \exp\left(-\frac{m_t - m_0}{T_2}\right) \quad . \quad (6.2.2)$$

The two formulae are related to each other by following relations:

$$A_2 = w_D \cdot A_1 \quad (6.2.3)$$

$$T_2^{-1} = T_1^{-1} + T_D^{-1} \quad . \quad (6.2.4)$$

For a spectrum which could be well described with the single-exponential formula, fitting to the double-exponential could be unstable and futile. For this

reason, we used one of the formulae (Equation 6.1.1 or 6.2.2) depending on the circumstances.

6.2.4 Rapidity Distributions

The rapidity distribution of produced particles was evaluated by an integration of the invariant cross section over transverse mass. From the single-exponential formula (Equation 6.1.1), the cross section $d\sigma/dy$ of particle production in a rapidity bin can be derived as

$$\frac{d\sigma}{dy} = \int_{m_0}^{\infty} \frac{d\sigma^2}{2\pi m_t dm_t dy} \cdot 2\pi m_t dm_t \tag{6.2.5}$$

$$= 2\pi A_0 T_0 (T_0 + m_0) \tag{6.2.6}$$

with already defined parameters. Similarly from the double-exponential (Equation 6.2.2), $d\sigma/dy$ can be expressed as

$$\frac{d\sigma}{dy} = 2\pi A_1 T_1 (T_1 + m_0) + 2\pi A_2 T_2 (T_2 + m_0) \ . \tag{6.2.7}$$

For a correct estimation of the statistical errors of the particle yield and of the inverse slope parameter, fitting of the transverse-mass spectra was performed to the following formulae:

$$\frac{1}{\sigma_{trig}} \cdot \frac{d^2\sigma}{2\pi m_t dm_t dy} = \frac{1}{2\pi T_0 (T_0 + m_0)} \cdot \frac{dN}{dy} \cdot \exp\left(-\frac{m_t - m_0}{T_0}\right) \tag{6.2.8}$$

assuming the single-exponential or

$$\begin{aligned} \frac{1}{\sigma_{trig}} \cdot \frac{d^2\sigma}{2\pi m_t dm_t dy} = & \\ & \frac{1}{2\pi T_1 (T_1 + m_0)} \cdot \frac{1}{1+w} \cdot \frac{dN}{dy} \cdot \exp\left(-\frac{m_t - m_0}{T_1}\right) \\ + & \frac{1}{2\pi T_2 (T_2 + m_0)} \cdot \frac{w}{1+w} \cdot \frac{dN}{dy} \cdot \exp\left(-\frac{m_t - m_0}{T_2}\right) \end{aligned} \tag{6.2.9}$$

assuming the double-exponential, where dN/dy is the particle yield per trigger in a unit rapidity (rapidity density) defined as

$$\frac{dN}{dy} \equiv \frac{1}{\sigma_{trig}} \cdot \frac{d\sigma}{dy} \ , \tag{6.2.10}$$

and w is the yield ratio between the two components which can be related to the normalization factors A_1 and A_2 as

$$w = \frac{A_2 T_2 (T_2 + m_0)}{A_1 T_1 (T_1 + m_0)} . \quad (6.2.11)$$

Rapidity distributions of π^- and protons were evaluated using the double-exponential formula, while the single-exponential was applied to π^+ and K^+. Though the spectra of π^+ also indicated a tendency to enhance in the low transverse-kinetic-energy regions, it was so small as to lead to unstable fitting with the double-exponential formula. As for K^+, we could not determine the shape of its spectra due to its poor statistics. The first point of each transverse-mass spectrum was eliminated from the fitting, considering the systematic error at the edges of the acceptance.

Figures 6.2.6 – 6.2.8 show the rapidity distributions and the inverse slope parameters of $\pi^\pm$, K^+, and protons. The enhancement/suppression factors w are also shown for π^- and protons. The error bars indicate the statistical errors only. The results are also tabulated with the χ^2 of the fitting in Tables 6.2.1 and 6.2.2.

6.3 Non-Central Collisions

The non-central collision events were analyzed in the same way as the central events, to understand the behavior of the single particle spectra through a comparison between different centrality. We selected events corresponding to the impact parameter larger than 4.0 fm; central 0.50 barn of cross section (9.5 % of the interaction cross section) was rejected from the data taken with the interaction (INT) trigger, by a cut on the energy deposit in the zero-degree calorimeter, as described in Section 5.4.

6.3.1 Transverse-Mass Spectra

The invariant differential yields of $\pi^\pm$, K^+, and protons in non-central collisions of Au+Au at 11 A GeV/c are shown in Figures 6.3.1 and 6.3.2, as a function of transverse kinetic energy. The top spectrum in each figure is displayed with the correct ordinate value, while the others are successively divided by a factor of 10. The error bars indicate the statistical errors only.

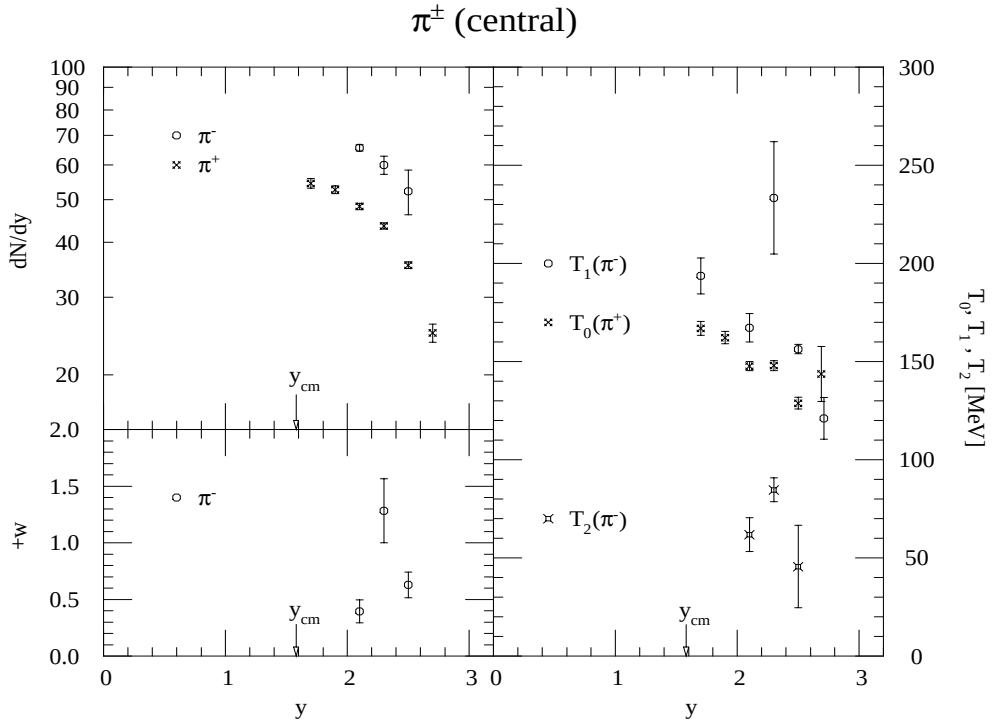

Figure 6.2.6: The rapidity distributions (upper left), the enhancement factor (lower left; π^- only), and the inverse slope parameters (right) of $\pi^\pm$ in central (4 %) Au+Au collisions at 11 A GeV/c. The error bars indicate the statistical errors only. Note that different parameterization was applied for π^+ and π^-. See text for the definitions of w, T_0, T_1, and T_2.

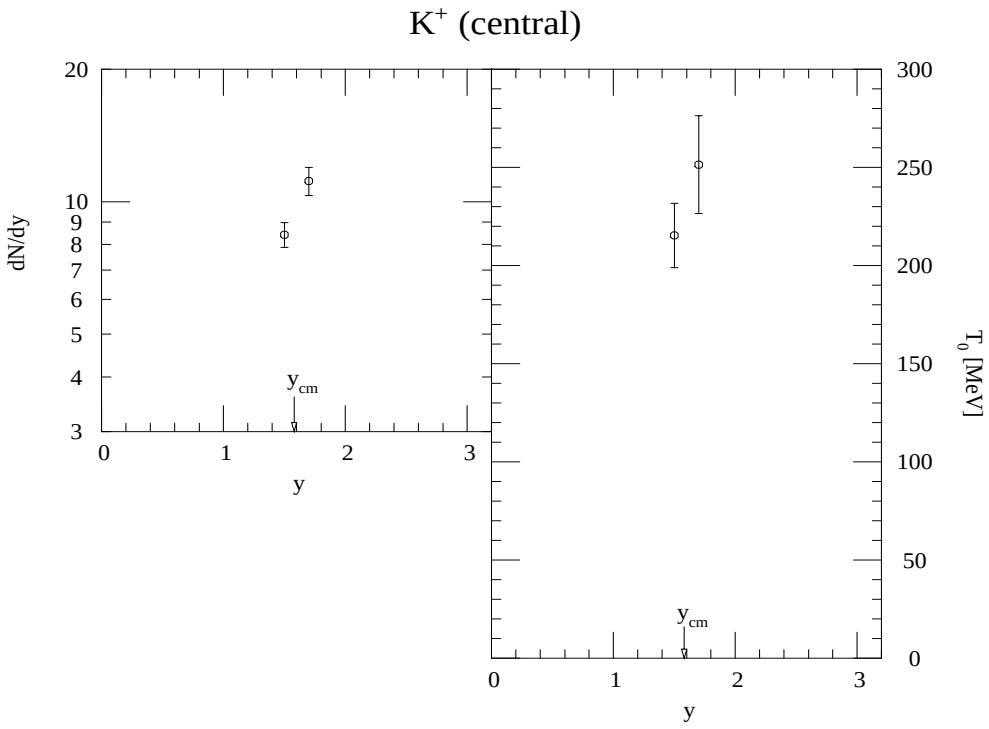

Figure 6.2.7: The rapidity distribution (left) and the inverse slope parameter (right) of K^+ in central (4 %) Au+Au collisions at 11 A GeV/c. The error bars indicate the statistical errors only.

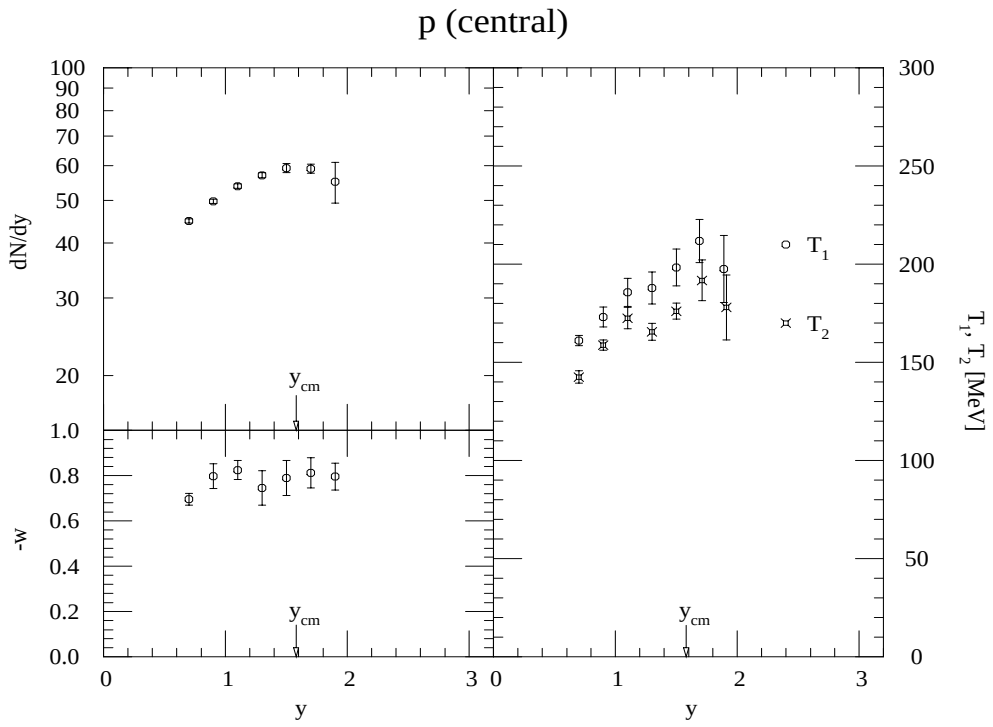

Figure 6.2.8: The rapidity distribution (upper left), the suppression factor (lower left), and the inverse slope parameter (right) of protons in central (4 %) Au+Au collisions at 11 A GeV/c. The error bars indicate the statistical errors only. See text for the definitions of w, T_1, and T_2.

π^+ (central)					
y	dN/dy		T_0 [MeV/c^2]		χ^2 / DOF
1.7	54.48 ± 1.41		167.0 ± 3.6		56.62 / 42
1.9	52.69 ± 1.07		162.3 ± 3.1		52.68 / 35
2.1	48.28 ± 0.79		147.8 ± 2.3		37.11 / 29
2.3	43.60 ± 0.69		148.0 ± 2.6		34.19 / 22
2.5	35.48 ± 0.64		128.9 ± 3.0		32.96 / 15
2.7	24.88 ± 1.19		143.8 ± 14.0		3.59 / 5
π^- (central)					
y	dN/dy	$+w$	T_1 [MeV/c^2]	T_2 [MeV/c^2]	χ^2 / DOF
1.7	—	—	193.7 ± 9.2	—	29.56 / 30
1.9	—	—	—	—	—
2.1	65.58 ± 1.09	0.40 ± 0.10	167.3 ± 7.2	62.0 ± 8.6	30.68 / 27
2.3	59.97 ± 2.85	1.28 ± 0.28	233.4 ± 28.6	84.7 ± 6.1	18.14 / 20
2.5	52.28 ± 6.09	0.63 ± 0.11	156.4 ± 2.4	45.7 ± 21.0	18.81 / 13
2.7	—	—	121.1 ± 10.6	—	2.15 / 3

Table 6.2.1: The rapidity densities dN/dy, the enhancement factor $+w$ (π^- only), and the inverse slope parameters T_0 (for π^+) or T_1 and T_2 (for π^-) of $\pi^\pm$ in central (4 %) Au+Au collisions at 11 A GeV/c, with the χ^2 of the fitting. See text for the definitions of the parameters. Dashes in the table denote that the fitting did not converge for the variables.

K^+ (central)					
y	dN/dy		T_0 [MeV/c^2]		χ^2 / DOF
1.5	8.42 ± 0.55		215.4 ± 16.4		36.66 / 32
1.7	11.16 ± 0.82		251.5 ± 24.9		18.08 / 25
p (central)					
y	dN/dy	$-w$	T_1 [MeV/c^2]	T_2 [MeV/c^2]	χ^2 / DOF
0.7	44.90 ± 0.51	0.70 ± 0.03	161.2 ± 2.6	142.6 ± 3.1	57.71 / 41
0.9	49.77 ± 0.56	0.80 ± 0.05	173.1 ± 5.1	158.8 ± 2.6	36.48 / 47
1.1	53.89 ± 0.65	0.83 ± 0.04	185.7 ± 7.2	172.6 ± 5.4	55.48 / 44
1.3	57.02 ± 0.76	0.75 ± 0.08	187.9 ± 8.1	165.6 ± 4.3	45.75 / 45
1.5	59.23 ± 1.44	0.79 ± 0.08	198.4 ± 9.4	176.1 ± 4.1	84.24 / 56
1.7	59.04 ± 1.42	0.81 ± 0.07	211.9 ± 11.0	191.8 ± 10.4	38.34 / 38
1.9	55.17 ± 5.87	0.80 ± 0.06	197.6 ± 17.1	178.0 ± 16.5	20.29 / 20

Table 6.2.2: The rapidity densities dN/dy, the suppression factor $-w$ (protons only), and the inverse slope parameters T_0 (for K^+) or T_1 and T_2 (for protons) of K^+ and protons in central (4 %) Au+Au collisions at 11 A GeV/c, with the χ^2 of the fitting. See text for the definitions of the parameters.

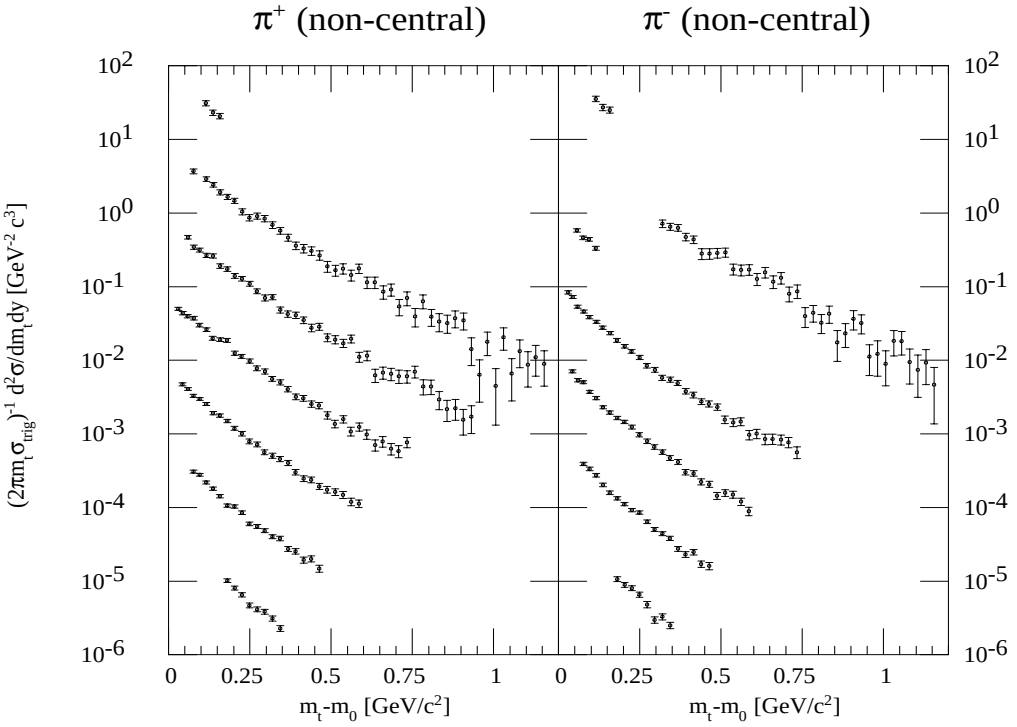

Figure 6.3.1: The invariant differential yields of $\pi^{\pm}$ in non-central (90 %) Au+Au collisions at 11 A GeV/c, as a function of transverse kinetic energy ($m_t - m_0$). The successive spectra are for different rapidity (y) bins, from $y = 1.5$ (top) to $y = 2.7$ (bottom) with intervals of 0.2. Each successive spectrum is divided by 10. The error bars indicate the statistical errors only.

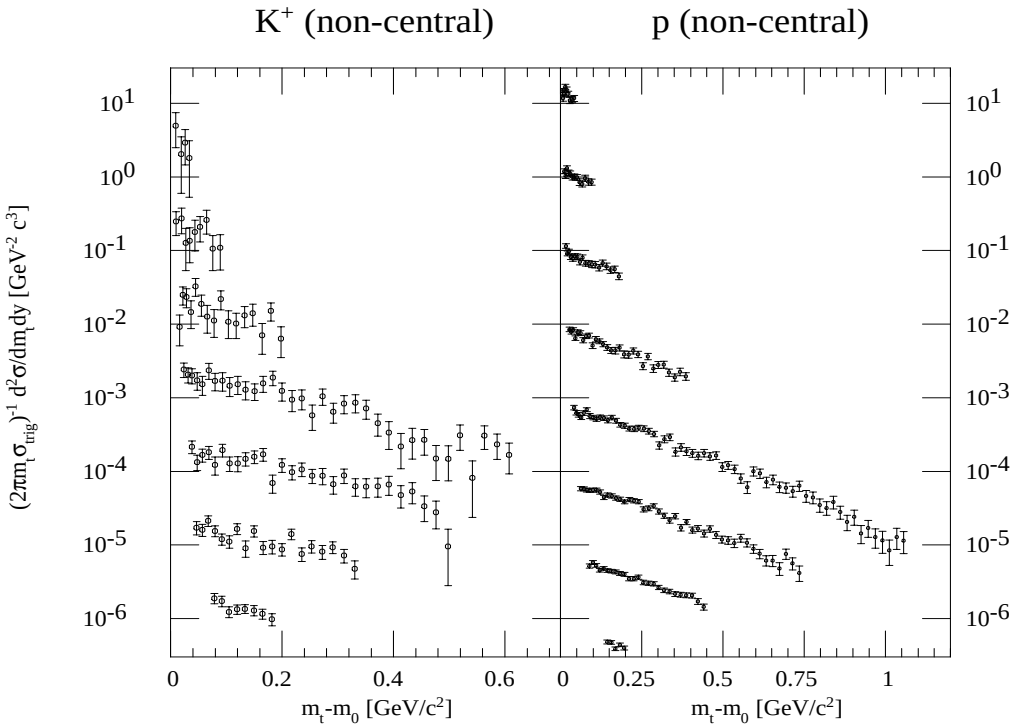

Figure 6.3.2: The invariant differential yields of K^+ and protons in non-central (90 %) Au+Au collisions at 11 A GeV/c, as a function of transverse kinetic energy ($m_t - m_0$). The successive spectra are for different rapidity (y) bins, from $y = 0.9$ (top) to $y = 2.1$ (bottom) for K^+ and from $y = 0.7$ (top) to $y = 2.1$ (bottom) for protons, with intervals of 0.2. Each successive spectrum is divided by 10. The error bars indicate the statistical errors only.

6.3.2 Rapidity Distributions

Even in non-central collisions, π^- and protons showed a discrepancy from the single-exponential formula. Because of the behavior, evaluation of their invariant yields could suffer from a large systematic error if the covered transverse-kinetic-energy region was insufficient or the single-exponential formula was applied. For the non-central collision events, however, no corresponding data were available from the Henry Higgins spectrometer. The rapidity distributions of π^- and protons were hence calculated using the double-exponential formula (Equation 6.2.2) only in rapidity regions where the Forward Spectrometer had good transverse-kinetic-energy coverages. On the other hand, those of π^+ and K^+ were calculated using the single-exponential (Equation 6.1.1) as in the analysis of central collisions.

Figure 6.3.3 shows the rapidity distributions of $\pi^{\pm}$, K^+, and protons in non-central Au+Au collisions at 11 A GeV/c, as well as the inverse slope parameters of π^+ and K^+. The error bars indicate the statistical errors only. The results are also tabulated with the χ^2 of the fitting in Table 6.3.1.

6.4 Inclusive Reactions

Here we present results from inclusive analysis, *i.e.* with the minimum-bias data taken with the interaction trigger. Analysis of particle production cross sections in inclusive reactions has a particular importance in comparisons with existing data, for instance with data with lighter collision systems.

6.4.1 Transverse-Mass Spectra

Figures 6.4.1 and 6.4.2 show the invariant differential cross sections of $\pi^{\pm}$, K^+, and protons in minimum-bias Au+Au collisions at 11 A GeV/c, as a function of transverse kinetic energy. The top spectrum in each figure is displayed with the correct ordinate value, while the others are successively divided by a factor of 10. The error bars indicate the statistical errors only.

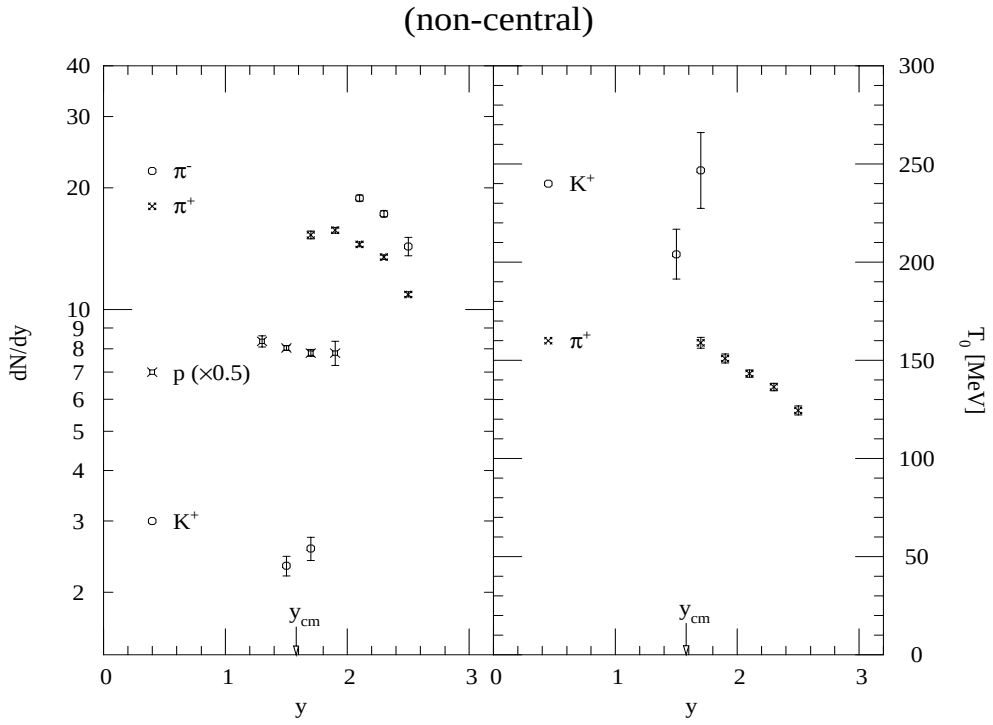

Figure 6.3.3: The rapidity distributions (left) and the inverse slope parameters (right; π^+ and K^+ only) of $\pi^{\pm}$, K^+, and protons in non-central (90 %) Au+Au collisions at 11 A GeV/c. The error bars indicate the statistical errors only.

π^+ (non-central)					
y	dN/dy		T_0 [MeV/c^2]		χ^2 / DOF
1.7	8.56 ± 0.19		159.0 ± 2.8		64.89 / 43
1.9	8.79 ± 0.15		151.0 ± 2.3		52.51 / 36
2.1	8.11 ± 0.11		143.3 ± 1.9		52.41 / 30
2.3	7.54 ± 0.10		136.5 ± 1.9		49.11 / 23
2.5	6.10 ± 0.09		124.6 ± 2.3		44.53 / 16
π^- (non-central)					
y	dN/dy	$+w$	T_1 [MeV/c^2]	T_2 [MeV/c^2]	χ^2 / DOF
1.7	—	—	169.7 ± 17.8	—	32.76 / 31
1.9	—	—	—	—	—
2.1	10.55 ± 0.18	1.27 ± 0.57	206.5 ± 29.3	89.7 ± 8.8	21.77 / 28
2.3	9.65 ± 0.17	0.38 ± 0.10	148.6 ± 6.7	56.3 ± 8.4	21.20 / 21
2.5	8.01 ± 0.42	0.38 ± 0.28	137.6 ± 20.4	53.1 ± 29.5	15.33 / 14
K^+ (non-central)					
y	dN/dy		T_0 [MeV/c^2]		χ^2 / DOF
1.5	1.30 ± 0.07		204.1 ± 12.7		27.94 / 33
1.7	1.44 ± 0.10		246.8 ± 19.3		30.30 / 26
p (non-central)					
y	dN/dy	$-w$	T_1 [MeV/c^2]	T_2 [MeV/c^2]	χ^2 / DOF
1.3	9.34 ± 0.29	—	241.2 ± 43.3	—	36.60 / 26
1.5	9.00 ± 0.13	0.22 ± 0.06	220.7 ± 6.8	109.6 ± 15.5	65.96 / 57
1.7	8.74 ± 0.17	0.12 ± 0.06	240.1 ± 13.1	78.6 ± 29.6	39.57 / 39
1.9	8.74 ± 0.60	0.37 ± 0.31	223.2 ± 48.9	156.8 ± 30.4	13.53 / 21

Table 6.3.1: The rapidity densities dN/dy, the enhancement/suppression factors w (π^- and protons only), and the inverse slope parameters T_0 (for π^+ and K^+) or T_1 and T_2 (for π^- and protons) of $\pi^{\pm}$, K^+, and protons in non-central (90 %) Au+Au collisions at 11 A GeV/c, with the χ^2 of the fitting. See text for the definitions of the parameters. Dashes in the table denote that the fitting did not converge for the variables.

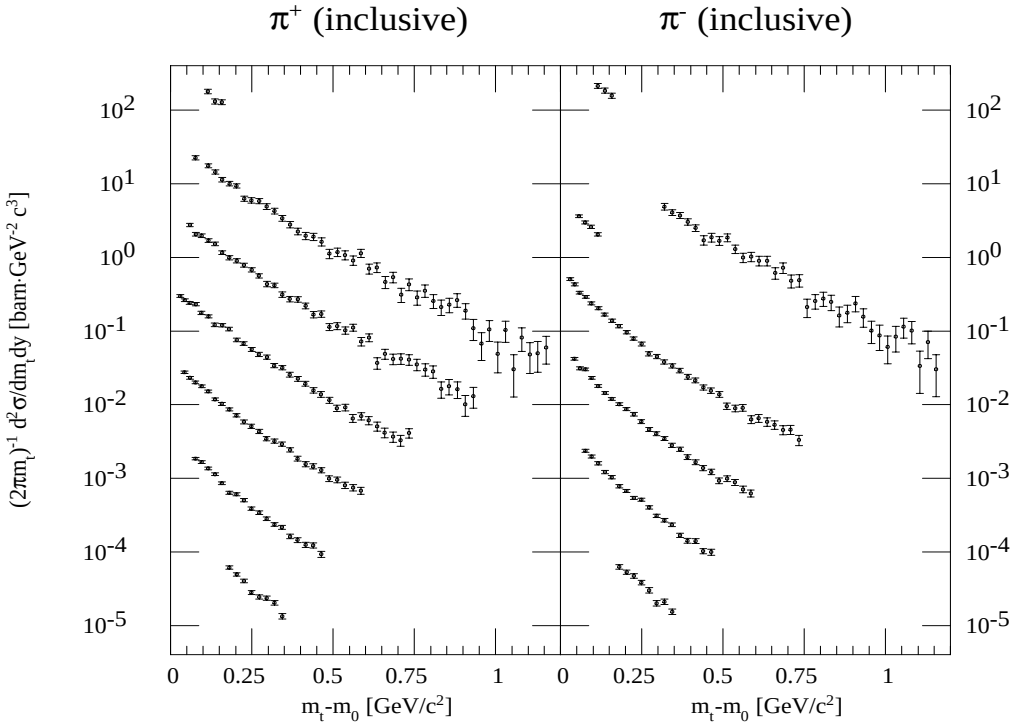

Figure 6.4.1: The invariant cross sections of $\pi^{\pm}$ in minimum-bias Au+Au collisions at 11 A GeV/c, as a function of transverse kinetic energy ($m_t - m_0$). The successive spectra are for different rapidity (y) bins, from $y = 1.5$ (top) to $y = 2.7$ (bottom) with intervals of 0.2. Each successive spectrum is divided by 10. The error bars indicate the statistical errors only.

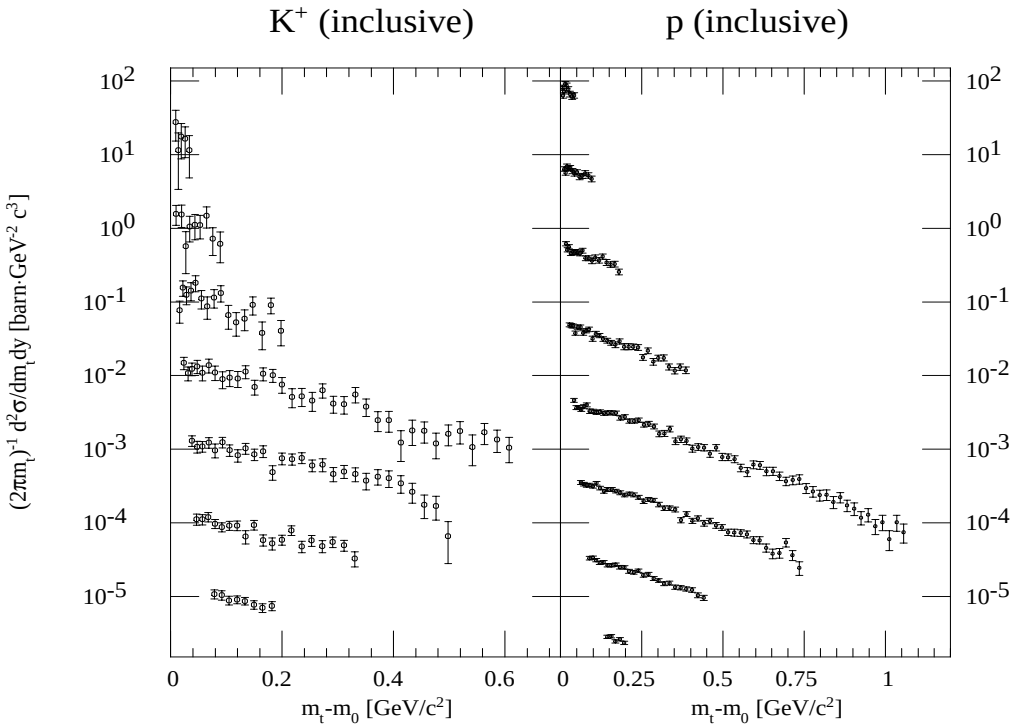

Figure 6.4.2: The invariant cross sections of K^+ and protons in minimum-bias Au+Au collisions at 11 A GeV/c, as a function of transverse kinetic energy ($m_t - m_0$). The successive spectra are for different rapidity (y) bins, from $y = 0.9$ (top) to $y = 2.1$ (bottom) for K^+ and from $y = 0.7$ (top) to $y = 2.1$ (bottom) for protons, with intervals of 0.2. Each successive spectrum is divided by 10. The error bars indicate the statistical errors only.

6.4.2 Rapidity Distributions

The invariant cross sections of $\pi^{\pm}$, K^{+}, and protons in minimum-bias Au+Au collisions at 11 A GeV/c are shown in Figure 6.4.3, as a function of rapidity. The inverse slope parameters are also shown for π^{+} and K^{+}, with which the single-exponential formula was applied. The error bars indicate the statistical errors only, and the results are also tabulated with the χ^2 of the fitting in Table 6.4.1. Considering the validity of the parameterization, the analysis was limited in rapidity regions where the Forward Spectrometer had sufficient transverse-kinetic-energy coverage for each particle species.

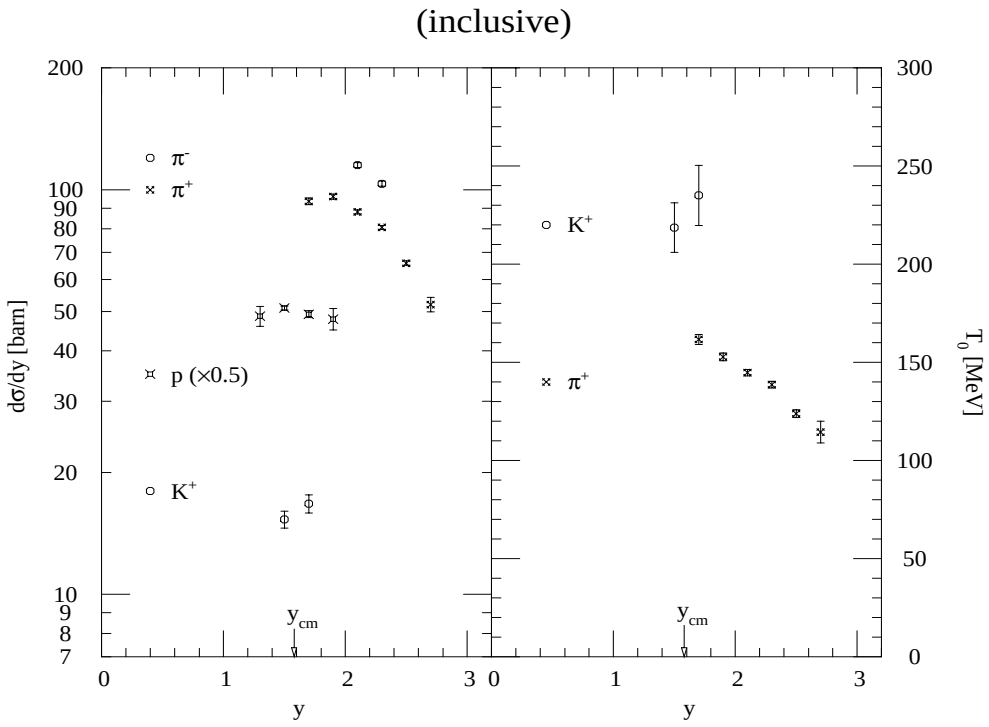

Figure 6.4.3: The invariant cross sections (left) and the inverse slope parameters (right; π^+ and K^+ only) of $\pi^{\pm}$, K^+, and protons in minimum-bias Au+Au collisions at 11 A GeV/c. The error bars indicate the statistical errors only.

π^+					
y	$d\sigma/dy$ [barn]		T_0 [MeV/c^2]		χ^2 / DOF
1.7	93.7 ± 1.8		161.7 ± 2.6		73.11 / 43
1.9	96.2 ± 1.4		152.9 ± 2.0		64.70 / 36
2.1	88.2 ± 1.1		144.8 ± 1.6		47.57 / 30
2.3	80.7 ± 0.9		138.7 ± 1.7		47.19 / 23
2.5	65.8 ± 0.9		123.9 ± 2.0		50.99 / 16
2.7	52.0 ± 2.1		114.5 ± 5.5		14.14 / 6
π^-					
y	$d\sigma/dy$ [barn]	$+w$	T_1 [MeV/c^2]	T_2 [MeV/c^2]	χ^2 / DOF
1.7	—	—	171.5 ± 4.5	—	32.18 / 31
1.9	—	—	—	—	—
2.1	115.1 ± 1.5	1.03 ± 0.37	196.5 ± 19.4	85.4 ± 7.6	18.49 / 28
2.3	103.5 ± 1.5	0.74 ± 0.19	170.3 ± 10.1	74.1 ± 6.1	20.80 / 21
K^+					
y	$d\sigma/dy$ [barn]		T_0 [MeV/c^2]		χ^2 / DOF
1.5	15.3 ± 0.7		218.7 ± 12.6		23.88 / 33
1.7	16.8 ± 0.9		235.1 ± 15.3		30.64 / 26
p					
y	$d\sigma/dy$ [barn]	$-w$	T_1 [MeV/c^2]	T_2 [MeV/c^2]	χ^2 / DOF
1.3	97.4 ± 5.5	0.56 ± 0.17	196.7 ± 18.6	167.3 ± 12.4	35.55 / 26
1.5	102.0 ± 1.2	0.25 ± 0.09	227.1 ± 9.2	123.4 ± 18.8	56.94 / 57
1.7	98.5 ± 2.0	0.21 ± 0.10	241.1 ± 15.9	112.6 ± 26.7	40.04 / 39
1.9	95.8 ± 5.9	0.57 ± 0.25	210.5 ± 21.2	170.5 ± 37.5	11.04 / 21

Table 6.4.1: The invariant cross sections $d\sigma/dy$, the enhancement/suppression factors w (π^- and protons only), and the inverse slope parameters T_0 (for π^+ and K^+) or T_1 and T_2 (for π^- and protons) of $\pi^\pm$, K^+, and protons in minimum-bias Au+Au collisions at 11 A GeV/c, with the χ^2 of the fitting. See text for the definitions of the parameters. Dashes in the table denote that the fitting did not converge for the variables.

Chapter 7

Discussions

7.1 Overview

In this chapter, we select some of the experimental results with our interest and give discussions. As well as existent data with lighter collision systems, microscopic cascade models of nucleus-nucleus collisions and a hydro-dynamical collective-flow model are referred and compared with the data, as tools to understand the mechanisms of particle production in relativistic heavy-ion collisions.

Section 7.2 compares central Au+Au collisions with lighter collision systems measured by the AGS-E802 experiment. The featured subjects include the rapidity and the transverse-mass distributions of protons, which were major goals of the Forward Spectrometer as noted in Section 1.2, and the yield ratio of K^+ to π^+ as a measure of strangeness production. In Section 7.3, simulations of central Au+Au collisions based on cascade models are introduced. A discussion on the *nuclear stopping* power is given in the section, based on the rapidity distributions of protons; it has an importance as a measure of the baryon density achieved in the collision system. Also discussed is the observed deviation of the transverse-mass spectra of protons from the single-exponential formula; collective effects are investigated as an origin of the deviation, utilizing the cascade models. To further investigate the deviation and the slopes of the transverse-mass spectra of various hadrons, a discussion based on a hydro-dynamical model is given in Section 7.4. Finally in Section 7.5, consideration on a picture to describe Au+Au collisions at the AGS energy is presented, standing on the discussions utilizing the models.

7.2 Comparison with Lighter Systems

7.2.1 Existing E802 Data

As a reference to examine the data from Au+Au collisions, let us take results of the E802 experiment, the ancestor of the E866. The E802 experiment measured single particle spectra of various hadrons with the proton (p), ^{16}O, and ^{28}Si beams at 14.6 A GeV/c and various targets [26, 28], in use of the Henry Higgins spectrometer. We used the data from the lightest collision system measured by the experiment, p+Be, and from another quasi-symmetric system of Si+Al, for the comparison with Au+Au. Data from p+Be collisions can be considered to be a reference as a substitute for p+p data, since the average number of collisions between an incident proton and target nucleons is as small as 1.4*.

7.2.2 Rapidity Distribution of Protons

Figure 7.2.1 compares the rapidity distributions of protons in p+Be collisions (E802), in peripheral and central Si+Al collisions (E802)†, and in central Au+Au collisions (E866). The ordinate represents the rapidity density dN/dy normalized to the initial number of protons in the collision systems, *i.e.* 5 for p+Be, 27 for Si+Al, and 158 for Au+Au collisions. Since the beam momenta were different for the two experiments, the abscissa is also normalized to the beam rapidity.

As seen in the figure, the proton distributions showed a strong dependence on size of the collision systems. In p+Be collisions and in peripheral Si+Al collisions, where most participant protons suffer only one collision, few protons were observed at the mid-rapidity region and the rapidity distribution had two peaks at the beam rapidity and at the target rapidity. With the light system of Si+Al, the distribution still showed two peaks even in central collisions, originating from the beam participants and from the target participants. The average rapidity loss δy for the beam protons was of the order of $\simeq 1.0$ in the case, while the center-

*This value was calculated based on the cross section of p+p collisions and averaged over the collision geometry.

†In the E802 experiment, central Si+Al collisions were defined as 7 % of the total interaction cross section, selected with a device measuring the multiplicity of charged particles in the mid-rapidity region. Peripheral Si+Al collisions were defined with the energy deposit in the zero-degree calorimeter so as to select peripheral 58 % of the total interaction cross section.

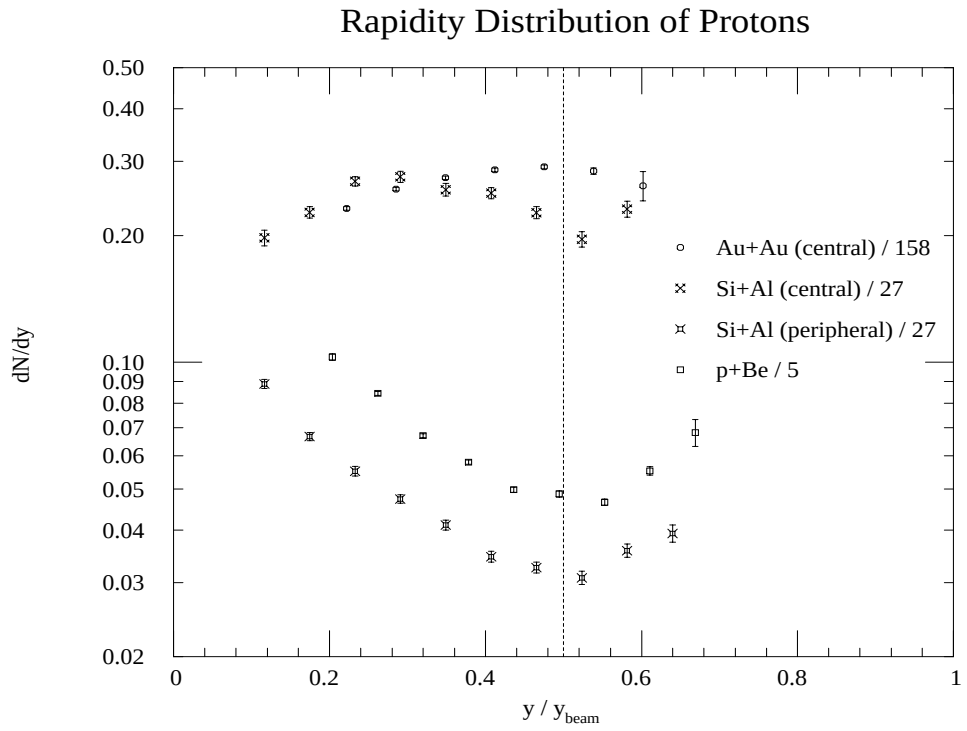

Figure 7.2.1: The rapidity distributions of protons in p+Be collisions at 14.6 GeV/c [26], in peripheral (58 %) and central (7 %) Si+Al collisions at 14.6 A GeV/c [28], and in central (4 %) Au+Au collisions at 11 A GeV/c. The abscissa is the rapidity normalized to the beam, and the ordinate is the rapidity density dN/dy divided by the initial number of protons in the collision system. The error bars indicate the statistical errors only.

of-mass rapidity was 1.72. On the other hand in central Au+Au collisions, the distribution displayed a single peak around the center of mass, with $\delta y \simeq 1.6$, suggesting that stronger and nearly complete nuclear stopping was achieved. It was the first observation of a single peak structure of the proton rapidity distribution around the center of mass in relativistic heavy-ion collisions at this high energy.

7.2.3 Transverse-Mass Spectra of Protons

In Figures 7.2.2 and 7.2.3, we present the transverse-mass spectra of protons in lighter collision systems, *i.e.* p+Be and central Si+Al, respectively, which were measured by the E802 experiment. It has been known but remained to be understood that the inverse slope parameter of protons increase with the mass of the system and the centrality of the collisions, though the spectra had stayed consistent with the single-exponential formula.

As shown in Figure 7.2.4 comparing the transverse-mass spectra of protons around the center-of-mass rapidity in three different collision systems, the proton spectra in the mid-rapidity region in central Au+Au collisions were found to be flatter than those from the lighter systems, showing a deviation from the single-exponential in the low transverse-kinetic-energy region. The solid lines indicated in the figure represent the results of fitting to the single-exponential formula (Equation 6.1.1) with the limited transverse-kinetic-energy range from 250 MeV/c^2 to 750 MeV/c^2. The corresponding inverse slope parameters are listed in Table 7.2.1. From the comparison, it can be concluded that the tendency of increasing flatness of the proton spectra has continued up to central Au+Au collisions. Besides, suppression in transverse-mass spectra of protons was found as a uniquely associated effect with the massive collision system.

7.2.3.1 Flatness of Proton Spectra

Already in p+A collisions, transverse-mass spectra of $K^{\pm}$ and protons were known to become flatter with increasing mass of the target nuclei [71, 26], but only slightly. The effect has been interpreted, for example, by a random-walk mechanism in which a particle generated or struck out inside the nuclei acquires the transverse momentum during random-walk collisions until it leaves the system

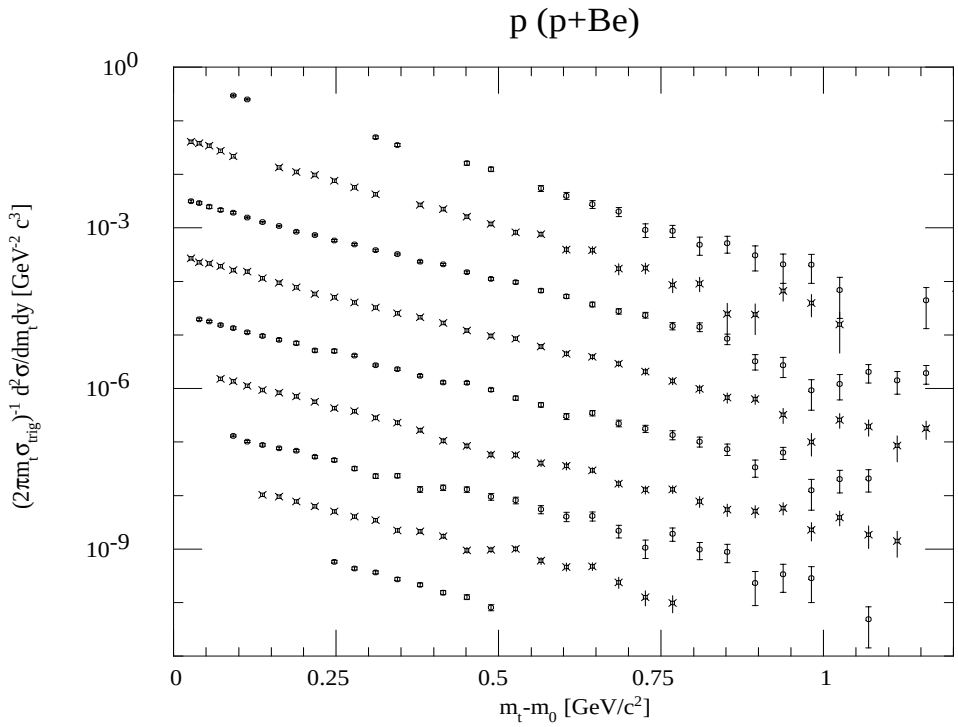

Figure 7.2.2: The invariant differential yield of protons in p+Be collisions at 14.6 GeV/c, as a function of transverse kinetic energy ($m_t - m_0$) [26]. Successive spectra are for different rapidity (y) bins, from $y = 0.7$ (top) to $y = 2.3$ with intervals of 0.2. Each successive spectrum is divided by 10. The error bars indicate the statistical errors only.

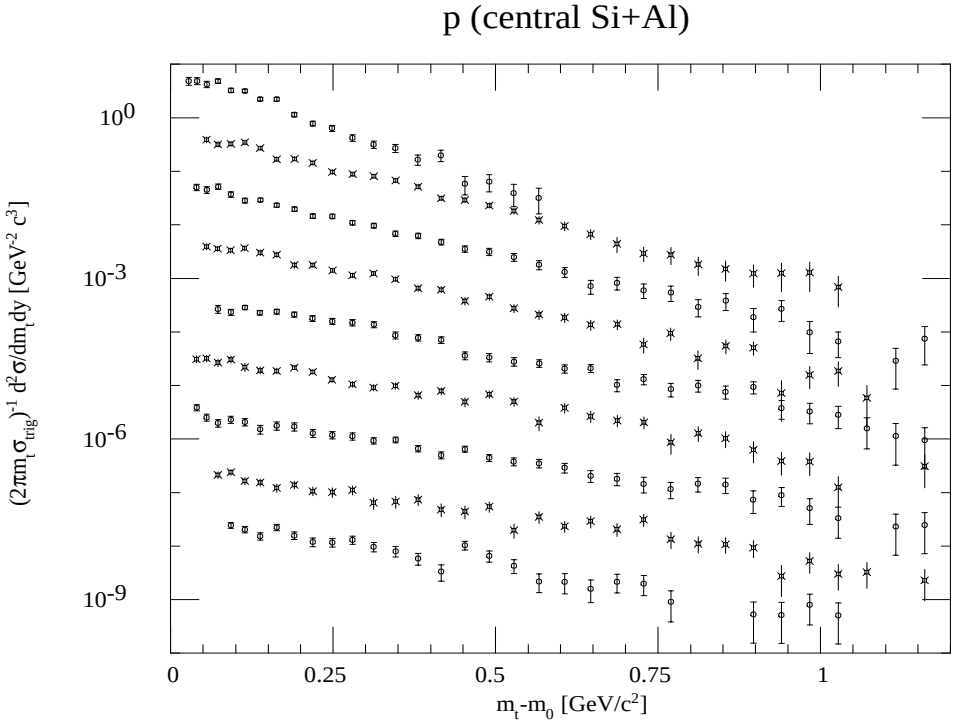

Figure 7.2.3: The invariant differential yield of protons in central (7 %) Si+Al collisions at 14.6 A GeV/c, as a function of transverse kinetic energy ($m_t - m_0$) [28]. Successive spectra are for different rapidity (y) bins, from $y = 0.4$ (top) to $y = 2.0$ with intervals of 0.2. Each successive spectrum is divided by 10. The error bars indicate the statistical errors only.

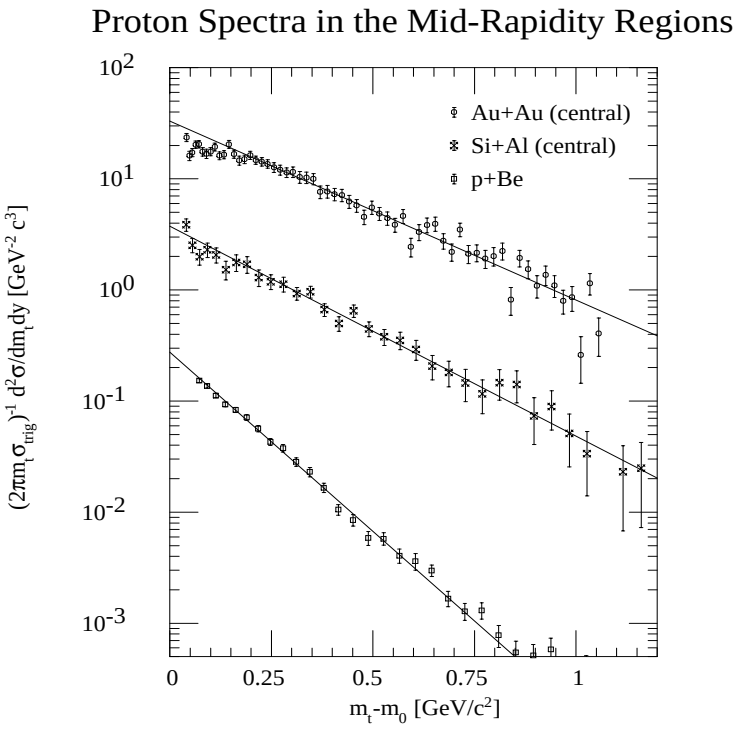

Figure 7.2.4: The invariant differential yields of protons around the center-of-mass rapidity in p+Be collisions at 14.6 GeV/c ($y = 1.7$) [26], in central (7 %) Si+Al collisions at 14.6 A GeV/c ($y = 1.6$) [28], and in central (4 %) Au+Au collisions at 11 A GeV/c ($y = 1.5$), as a function of transverse kinetic energy ($m_t - m_0$). The error bars indicate the statistical errors only. The solid lines represent the results of fitting to the single-exponential formula with the limited transverse-kinetic-energy range from 250 MeV/c^2 to 750 MeV/c^2.

Collision System	Inverse Slope Parameter [MeV]
p+Be	135 ± 9
Si+Al (central)	230 ± 26
Au+Au (central)	270 ± 18

Table 7.2.1: The inverse slope parameters of protons around the center-of-mass rapidity with the limited transverse-kinetic-energy range from 250 MeV/c^2 to 750 MeV/c^2, in p+Be collisions at 14.6 GeV/c ($y = 1.7$), in central (7 %) Si+Al collisions at 14.6 A GeV/c ($y = 1.6$), and in central (4 %) Au+Au collisions at 11 A GeV/c ($y = 1.5$). See also Figure 7.2.4. The errors listed are statistical only.

[72, 73]. The mechanism, however, cannot explain the fact that the variation of the slopes is much steeper in A+A collisions than in p+A collisions [74]. Since the cause of the flatness of the spectra of protons (and other heavy particles) in relativistic nucleus-nucleus collisions has remained open, various approaches have historically been tried. The rescattering by the spectator nucleons has turned out not to account for the effect, as well as the Fermi motion of the participants [75]. Another possible approach to understand the flatness is a collective-flow model [76, 77]. A discussion based on the model is presented in Section 7.4 to understand the flatness of the proton spectra, as well as the variation of the slopes of the spectra of hadrons with different masses, in Au+Au collisions.

7.2.3.2 Convex Shape of Proton Spectra

Here we point out an issue related to the convex shape of the proton spectra found in Au+Au collisions at 11 A GeV/c.

At the Bevalac energy of 0.8 A GeV/c, it has been known that the transverse-mass spectra of protons from nucleus-nucleus collisions show a *shoulder-arm* shape, which is similar to what we observed in Au+Au collisions at the AGS energy, as shown in Figure 7.2.5 [78]. The deviation was, however, observed even in lighter collision systems such as ^{12}C+^{12}C at the lower energy, and has been interpreted as a contribution of quasi-elastic scattering [79] which must be small at the AGS energy. In fact, the deviation from the single-exponential scaling

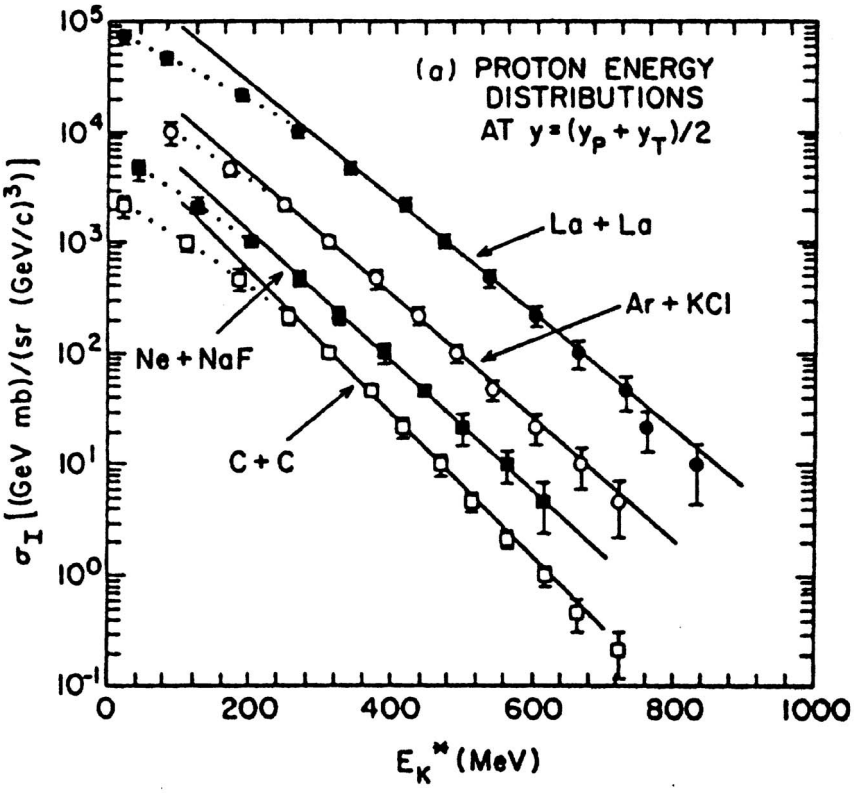

Figure 7.2.5: The invariant cross sections of protons around the center-of-mass rapidity in various collision systems at 0.8 A GeV/c [78]. The abscissa is transverse kinetic energy.

at the AGS energy was uniquely associated with massive collision systems, and should be considered to have a different origin from that at lower energies. See Sections 7.3 and 7.4 for further discussions on the convex shape of the transverse-mass spectra of protons.

7.2.4 Yield Ratio of K^+ to π^+

Enhancement of strangeness production has long been proposed to be a possible signature of formation of a quark-gluon plasma phase. Although the enhancement was reproduced in cascade models with rescattering of produced particles in hadronic matter [20, 80], it is still interesting to examine the behavior of the K^+/π^+ ratio with a heavier collision system such as Au+Au, since its evolution with the size of the system should provide information on the particle production

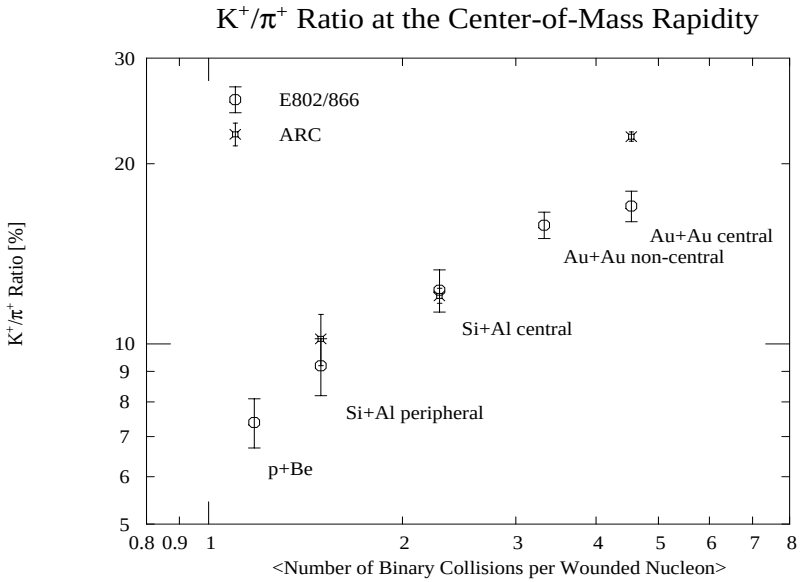

Figure 7.2.6: The yield ratios of K^+ to π^+ at the center-of-mass rapidity of nucleon-nucleon collisions in various collision systems, as a function of the average number of binary nucleon-nucleon collisions per wounded nucleon, which was calculated from the collision geometry. Plotted are data from quasi-symmetric systems of p+Be [26] and Si+Al [28] at 14.6 A GeV/c, and Au+Au at 11 A GeV/c. The error bars indicate the statistical errors only. See text for the definitions of their centrality. Results of cascade calculations with ARC are also shown.

mechanisms.

Here we again employ results of the E802 experiment for an examination of the data from Au+Au collisions. Figure 7.2.6 shows the yield ratios of K^+ to π^+ at the center-of-mass rapidity of nucleon-nucleon collisions in several collision systems and centrality. Also shown are calculations of a cascade model of nucleus-nucleus collisions, ARC[‡] [80], for peripheral and central Si+Al collisions and central Au+Au. See Appendix B for features of the model. The abscissa of the figure is the average number of binary nucleon-nucleon collisions per wounded nucleon in the system, which is equivalent to the *effective thickness* of the participants in the colliding nuclei and can be calculated from the collision geometry

[‡]A Relativistic Cascade. Version 1.95 of the code was used for discussions in this thesis.

as

$$\begin{aligned}&\langle\text{number of binary nucleon-nucleon collisions per wounded nucleon}\rangle \\ &= \frac{\langle\text{total number of binary nucleon-nucleon collisions}\rangle \times\ 2}{\langle\text{total number of wounded nucleons}\rangle}\ , \quad (7.2.1)\end{aligned}$$

where $\langle\rangle$ denotes the average over the ensemble and the impact parameter.

In light collision systems, the dependence of the ratio on the effective thickness of the participants was consistent with a power-law behavior [81], yet the experimental results from Au+Au collisions showed a tendency to saturate with increasing size of the collision system. Though this argument must not be considered conclusive because of the very limited kinematic coverage, it should be noted that a much higher K^+/π^+ ratio in central Au+Au collisions was predicted by ARC. The model was successful to reproduce the observed ratios in the lighter collision systems, but predicted a steeper increase of strangeness production which was consistent with the power-law behavior. It implies that the strangeness production and/or effects of rescattering in relativistic heavy-ion collisions have not been treated properly enough in the model, even though the cascade models were quite successful and promising with lighter collision systems, and that more theoretical examinations are required on the subject.

7.3 Microscopic Cascade Models

Let us introduce cascade models as microscopic simulators of relativistic heavy-ion collisions. Historically, many cascade simulation codes have been developed and used for comparisons with experimental data to study mechanisms of relativistic heavy-ion collisions. Some models are based on hadronic scattering and a string formation/fragmentation picture, and some are purely on a hadronic picture. The former type includes FRITIOF [40], HIJET [82], VENUS [21, 22, 83], and RQMD [39, 84]; ARC is one of the latter, treating low-mass resonances as its main ingredients. Comparisons are displayed between the experimental data and two of the cascade models, RQMD* and ARC here, since they have been developed to be applied in the energy region of the AGS while the others are for higher energies. A description on the two models can be found in Appendix B.

*Relativistic Quantum Molecular Dynamics. Version 1.08 of the code was used for discussions in this thesis.

7.3.1 Cascade Model Calculations

Data sets simulating central Au+Au collisions at the AGS energy were generated with RQMD [85] and ARC [86]. The beam momenta used in the simulations were slightly higher than that of the AGS operation in 1993: at 11.7 A GeV/c for RQMD and 11.6 A GeV/c for ARC[†]. The impact parameter was uniformly distributed in two dimensions within the maximum value of 4.0 fm. The total numbers of generated events were 809 for RQMD and 2,000 for ARC.

A centrality cut was performed for the data sets simulating the experimental method. The energy deposit in the zero-degree calorimeter, ZCAL, was approximately calculated for each event by summing up the kinetic energies of baryons and the total energies of mesons in the geometrical acceptance of ZCAL. The energy resolution of ZCAL of $\sim$ 100 % / GeV$^{-1/2}$ was taken into account. Figure 7.3.1 shows the correlation between the impact parameter and the energy deposit in ZCAL, for RQMD and ARC events; it can be seen that the energy emitted in the forward angle is a good measure of the centrality of the collisions.

The energy deposit for collisions with small impact parameters was larger in ARC than in RQMD by $\sim$ 8 %, suggesting stronger nuclear stopping in RQMD. As was done with the real data (Section 5.4), the threshold energy was set so as to select 4 % of the total interaction cross section, *i.e.* 0.21 barn, with the lowest energy deposit in ZCAL. The distributions of the impact parameters before and after the centrality cut are presented in Figure 7.3.2. The numbers of events selected and analyzed were 336 for RQMD and 837 for ARC.

Figures 7.3.3 – 7.3.6 show the transverse-mass spectra of $\pi^{\pm}$, K^{+}, and protons in the RQMD and ARC events, with the experimental data for a comparison. As seen in Figures 7.3.3 and 7.3.4, the both models reasonably well reproduced the spectra of $\pi^{\pm}$, except in the low transverse-kinetic-energy regions with $(m_t - m_0)$ less than $\sim$ 200 MeV/c^2. A brief discussion on pion spectra is given in the next subsection.

On the other hand for heavier particles (K^{+} and protons), both RQMD and ARC showed discrepancies from the experimental data in the mid-rapidity region. Around the center-of-mass rapidity, the models failed to reproduce the flatness of the spectra, overestimating the yields of K^{+} and protons at low transverse

[†]These momenta were based on the design value of the Au beam acceleration at the AGS.

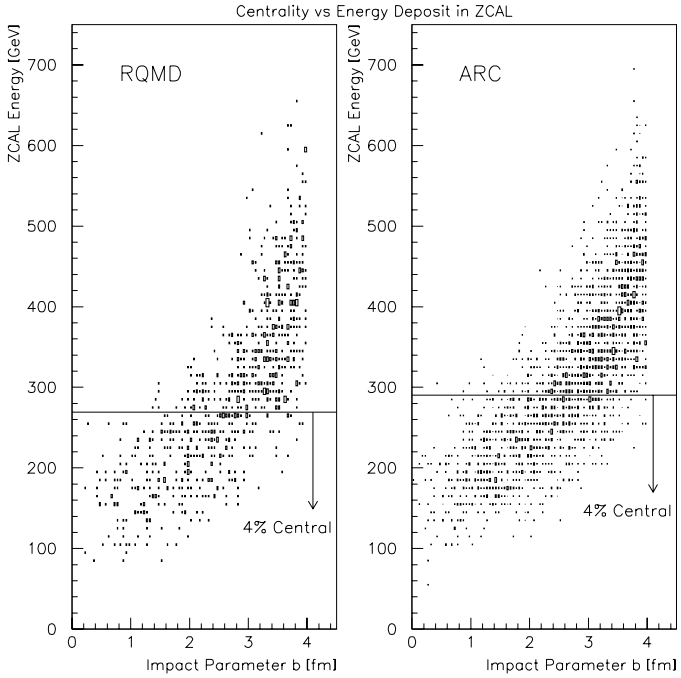

Figure 7.3.1: The correlation in cascade models between the impact parameter and the energy deposit in the zero-degree calorimeter, ZCAL. The centrality cut simulating the experimental method is also indicated.

kinetic energies. The models reproduced the experimental data much better in the rapidity region far from the center of mass. A brief discussion on yield of K^+ is presented in Section 7.2, based on the K^+/π^+ ratio at the center-of-mass rapidity where experimental data were available for both π^+ and K^+. For protons, detailed discussions are given on their rapidity distribution and on the shape and flatness of their transverse-mass spectra in following subsections.

7.3.2 Transverse-Mass Spectra of Pions

As mentioned above, the cascade models showed a reasonable agreement with the experimental data for $\pi^{\pm}$. Only in the low transverse-kinetic-energy regions with $(m_t - m_0)$ less than ~ 200 MeV/c^2, the models failed to reproduce the different behavior of π^+ and π^-. The enhancement of π^- in the regions has already been reported in Au+Au collisions [67] while spectra of π^+ and π^- in lighter collision systems did not show significant difference from each other at the AGS energy.

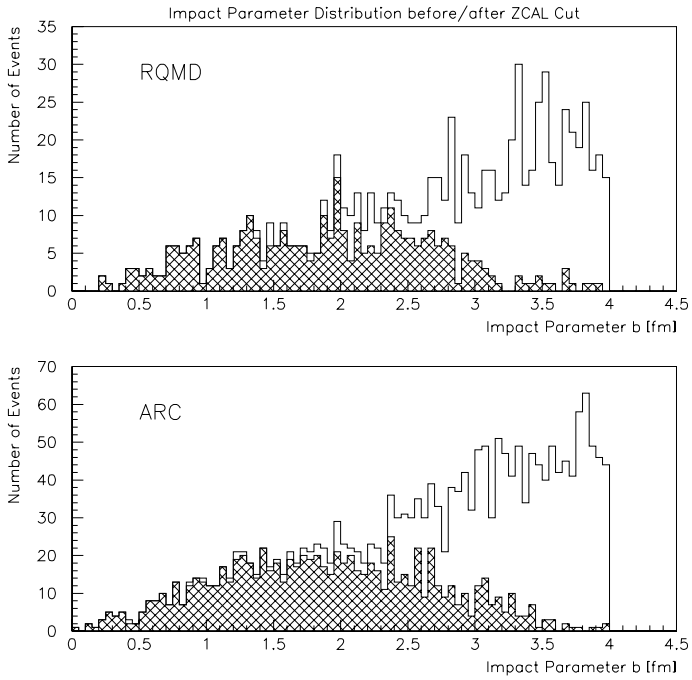

Figure 7.3.2: The impact parameter distributions in cascade models before and after the centrality cut using the energy deposit in the zero-degree calorimeter, ZCAL. The hatched areas represent the distributions after the cut at 4 % of the total interaction cross section.

Figure 7.3.7 shows the yield ratio of π^- to π^+ at rapidity $y = 2.1$, as a function of transverse kinetic energy, with the model calculations. The effect should be primarily due to the Coulomb effect[‡] [87, 88, 89], which has not been managed in the cascade models. The models therefore cannot reproduce the enhancement of π^-. The rapidity densities dN/dy and the inverse slope parameters T_0 of $\pi^\pm$ in the limited transverse-kinetic-energy range above 250 MeV/c^2 are tabulated in Tables 7.3.1 and 7.3.2. In the higher transverse-kinetic-energy regions, the both models globally agreed with the data, considering the systematic errors of the experimental results of $\pm \sim 10$ % (Section 5.7). It should be noted that RQMD predicted slightly higher yields of $\pi^\pm$ in the mid-rapidity region compared to ARC. That is consistent with a general tendency of RQMD, *i.e.* strong nuclear

[‡]There also exist efforts to understand the effect in terms of contributions of resonances (mostly Δ) originating from the asymmetry in the isospin space with neutron-rich heavy nucleus and of decay of hyperons [90, 91].

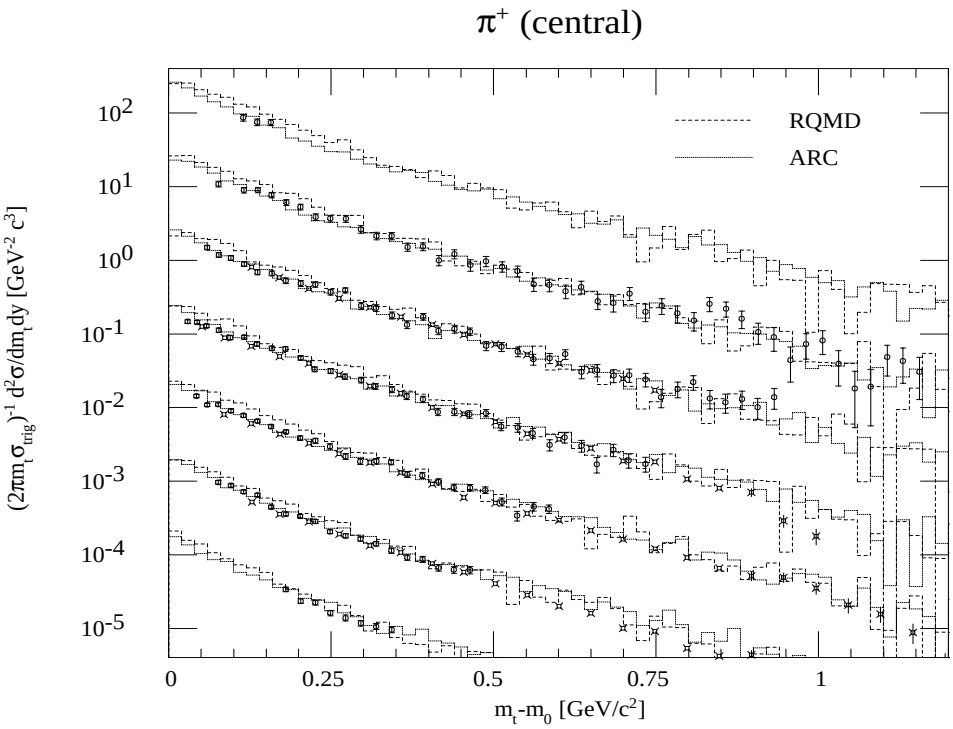

Figure 7.3.3: Model calculations of invariant differential yield of π^+ in central (4 %) Au+Au collisions at the AGS energy, as a function of transverse kinetic energy ($m_t - m_0$). Circles: data taken with the Forward Spectrometer. Frilled squares: data taken with the Henry Higgins spectrometer. Dashed histogram: RQMD. Dotted histogram: ARC. The successive spectra are for different rapidity (y) bins, from $y = 1.5$ (top) to $y = 2.7$ (bottom) with intervals of 0.2. Each successive spectrum is divided by 10.

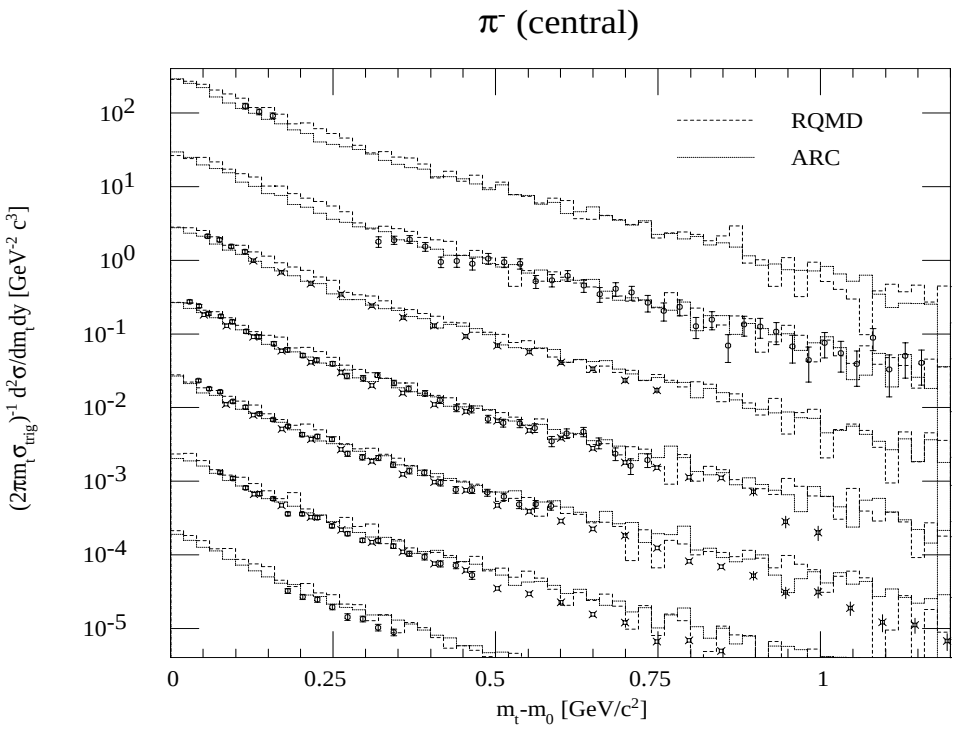

Figure 7.3.4: Model calculations of invariant differential yield of π^- in central (4 %) Au+Au collisions at the AGS energy, as a function of transverse kinetic energy ($m_t - m_0$). Circles: data taken with the Forward Spectrometer. Frilled squares: data taken with the Henry Higgins spectrometer. Dashed histogram: RQMD. Dotted histogram: ARC. The successive spectra are for different rapidity (y) bins, from $y = 1.5$ (top) to $y = 2.7$ (bottom) with intervals of 0.2. Each successive spectrum is divided by 10.

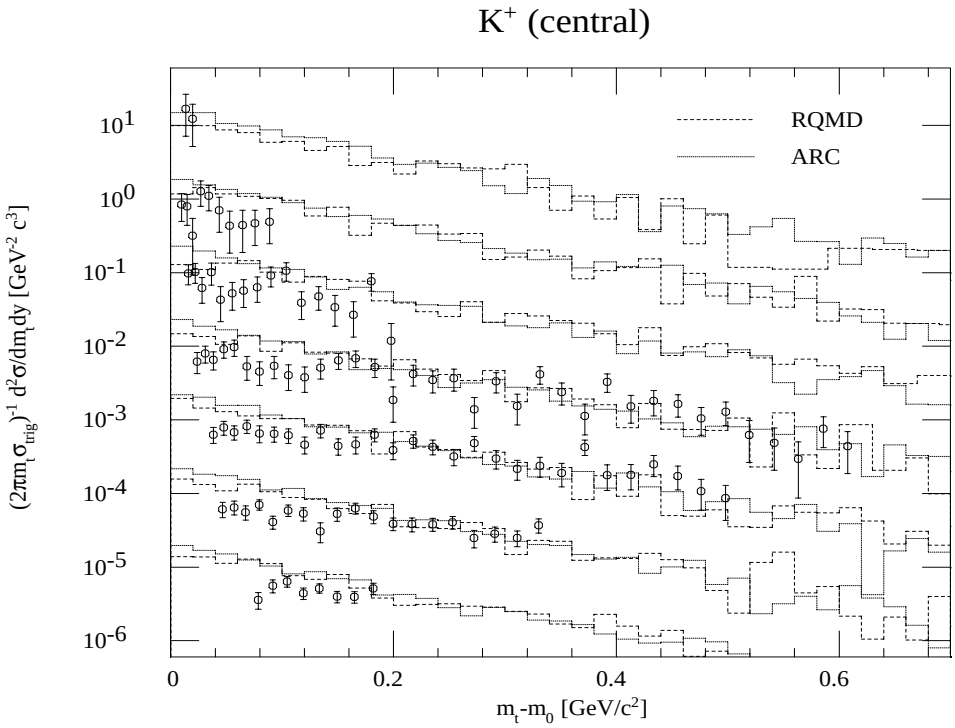

Figure 7.3.5: Model calculations of invariant differential yield of K^+ in central (4 %) Au+Au collisions at the AGS energy, as a function of transverse kinetic energy ($m_t - m_0$). Circles: data taken with the Forward Spectrometer. Dashed histogram: RQMD. Dotted histogram: ARC. The successive spectra are for different rapidity (y) bins, from $y = 0.9$ (top) to $y = 2.1$ (bottom) with intervals of 0.2. Each successive spectrum is divided by 10.

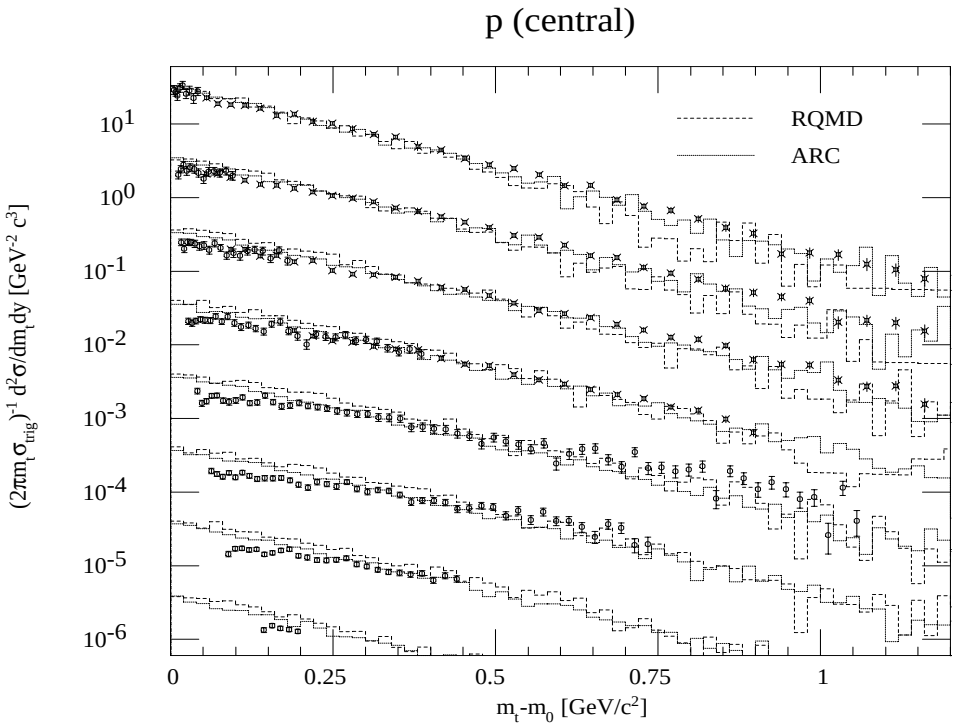

Figure 7.3.6: Model calculations of invariant differential yield of protons in central (4 %) Au+Au collisions at the AGS energy, as a function of transverse kinetic energy ($m_t - m_0$). Circles: data taken with the Forward Spectrometer. Frilled squares: data taken with the Henry Higgins spectrometer. Dashed histogram: RQMD. Dotted histogram: ARC. The successive spectra are for different rapidity (y) bins, from $y = 0.7$ (top) to $y = 2.1$ (bottom) with intervals of 0.2. Each successive spectrum is divided by 10.

π^+ ($m_t - m_0 > 250$ MeV/c^2)				
		dN/dy	T_0 [MeV/c^2]	χ^2 / DOF
$y = 1.7$	E866	21.51 ± 0.64	179.7 ± 5.1	38.67 / 37
	RQMD	22.62 ± 0.57	166.5 ± 4.1	88.77 / 65
	ARC	20.61 ± 0.35	179.4 ± 2.6	52.93 / 70
$y = 1.9$	E866	20.65 ± 0.56	170.1 ± 5.1	44.54 / 28
	RQMD	21.49 ± 0.56	157.7 ± 3.8	66.25 / 63
	ARC	19.06 ± 0.33	178.7 ± 2.7	89.26 / 69
$y = 2.1$	E866	16.77 ± 0.47	162.5 ± 4.9	16.80 / 20
	RQMD	20.70 ± 0.54	150.4 ± 3.7	58.59 / 55
	ARC	17.91 ± 0.32	172.4 ± 2.4	100.9 / 69
$y = 2.3$	E866	15.58 ± 0.51	161.5 ± 6.5	21.58 / 14
	RQMD	16.75 ± 0.49	155.5 ± 4.4	48.32 / 52
	ARC	16.12 ± 0.31	171.4 ± 2.7	62.36 / 62
$y = 2.5$	E866	11.35 ± 0.63	158.0 ± 9.6	4.345 / 8
	RQMD	12.77 ± 0.43	145.0 ± 4.5	58.35 / 46
	ARC	13.45 ± 0.28	167.9 ± 3.0	71.95 / 61
$y = 2.7$	E866	10.06 ± 2.61	178.5 ± 36.8	0.31 / 3
	RQMD	8.53 ± 0.35	142.1 ± 5.2	44.53 / 44
	ARC	10.11 ± 0.24	154.1 ± 2.9	82.30 / 55

Table 7.3.1: The rapidity densities dN/dy, the inverse slope parameters T_0, and the χ^2 of the fitting of π^+ with transverse kinetic energy $(m_t - m_0)$ above 250 MeV/c^2 in central Au+Au collisions at 11 A GeV/c (top rows) and in cascade calculations (middle and bottom rows). The errors listed are statistical only.

π^- ($m_t - m_0 > 250$ MeV/c^2)				
		dN/dy	T_0 [MeV/c^2]	χ^2 / DOF
$y = 1.7$	E866	21.37 ± 0.81	196.1 ± 6.9	30.61 / 33
	RQMD	27.18 ± 0.63	168.9 ± 3.6	81.77 / 66
	ARC	23.48 ± 0.37	182.8 ± 2.3	105.8 / 74
$y = 1.9$	E866	—	—	—
	RQMD	25.92 ± 0.61	168.0 ± 3.5	56.90 / 66
	ARC	22.87 ± 0.36	185.9 ± 2.5	49.14 / 69
$y = 2.1$	E866	19.79 ± 0.50	158.1 ± 4.4	25.70 / 20
	RQMD	23.35 ± 0.58	163.3 ± 3.8	45.79 / 57
	ARC	21.43 ± 0.35	178.6 ± 2.5	70.48 / 67
$y = 2.3$	E866	16.51 ± 0.51	156.2 ± 5.9	21.39 / 14
	RQMD	19.34 ± 0.53	156.7 ± 4.3	58.39 / 52
	ARC	19.46 ± 0.34	175.4 ± 2.6	71.12 / 65
$y = 2.5$	E866	11.95 ± 0.60	151.4 ± 8.7	4.871 / 8
	RQMD	16.14 ± 0.48	156.4 ± 4.2	60.96 / 54
	ARC	15.69 ± 0.30	173.6 ± 3.0	47.32 / 60
$y = 2.7$	E866	7.37 ± 1.16	123.0 ± 19.9	1.299 / 3
	RQMD	11.15 ± 0.40	136.4 ± 4.5	35.34 / 41
	ARC	12.49 ± 0.27	158.9 ± 2.8	50.19 / 54

Table 7.3.2: The rapidity densities dN/dy, the inverse slope parameters T_0, and the χ^2 of the fitting of π^- with transverse kinetic energy ($m_t - m_0$) above 250 MeV/c^2 in central Au+Au collisions at 11 A GeV/c (top rows) and in cascade calculations (middle and bottom rows). The errors listed are statistical only.

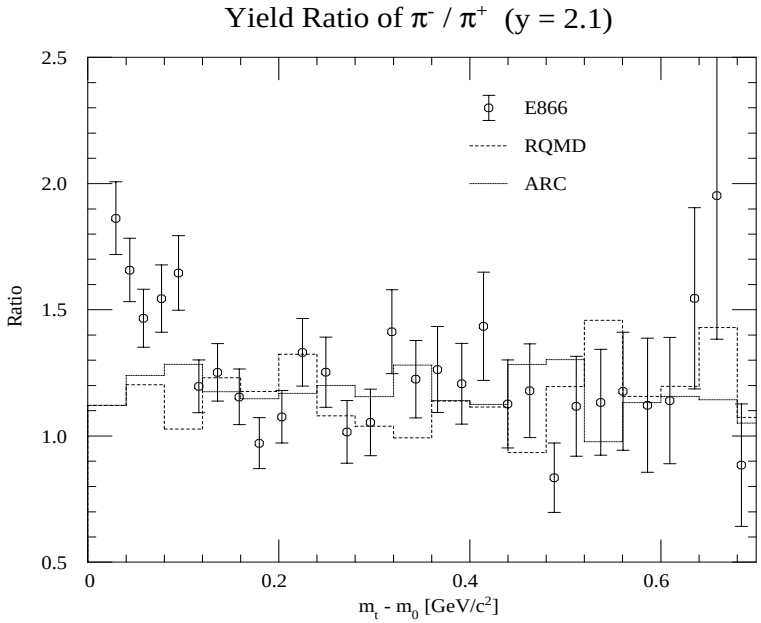

Figure 7.3.7: The yield ratio of π^- to π^+ in central (4 %) Au+Au collisions at rapidity $y = 2.1$, as a function of transverse kinetic energy, with model calculations. Circles: measurement by the E866 experiment. Dashed histogram: RQMD. Dotted histogram: ARC. The error bars of the data points indicate the statistical errors only.

stopping; a discussion on the topic is given in one of the following subsections based on the rapidity distribution of protons.

7.3.3 Nuclear Stopping Power

One of the major motivations for us to proceed to experiments with heavier collision systems was a theoretical prediction that the matter with an extremely high baryon density formed in the central part of the collision system develops both in size and lasting time [23, 39]. What really happens in the collisions, however, strongly depends on the nuclear stopping power, which would appear as the rapidity loss of the beam particles, and would be observable as the rapidity distribution of protons. Here we discuss the observed rapidity distribution of protons, comparing it with calculations of cascade models, to examine the nuclear stopping power in relativistic heavy-ion collisions and to obtain information on

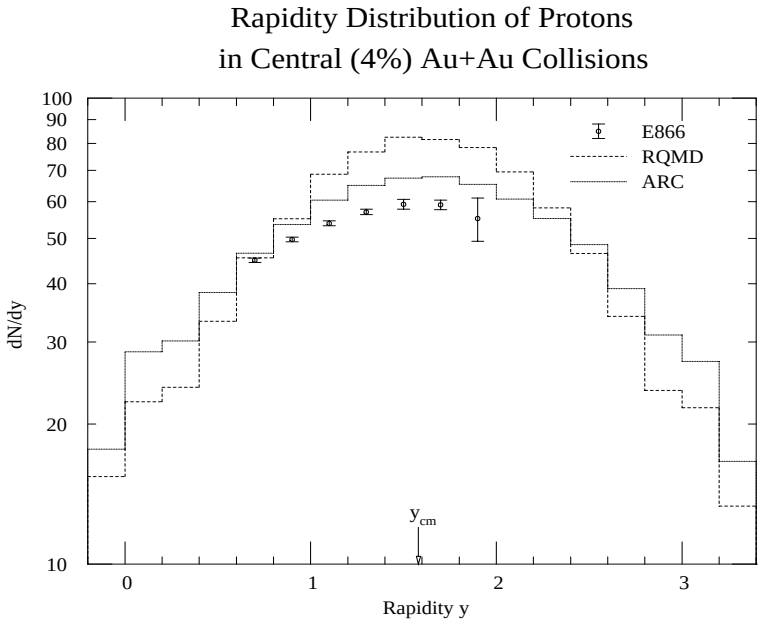

Figure 7.3.8: Model calculations of rapidity distribution of protons in central (4 %) Au+Au collisions at the AGS energy. Circles: measurement by the E866 experiment. Dashed histogram: RQMD. Dotted histogram: ARC. The error bars of the data points indicate the statistical errors only; the systematic errors of $\pm \sim 10$ % are not shown.

the baryon density achieved in the collision system.

Figure 7.3.8 shows the observed rapidity distribution of protons and calculations of RQMD and ARC. It is seen that RQMD overestimated the density of protons around the center-of-mass rapidity by ~ 40 %. ARC predicted a less sharp peak than RQMD, but still a discrepancy of ~ 14 % existed. It should be pointed out that the both cascade models did not include production of composites such as deuterons, which would decrease the yield of protons by 5 – 10 % if incorporated, but the discrepancy was too large to be explained by the effect.

As presented in Figure 7.3.9, it has been theoretically suggested that the rapidity distribution of protons may be a good probe of the nuclear stopping power, or equivalently the *transparency* [92]; according to a prediction by ARC, a proton distribution around the center-of-mass rapidity should be particularly sensitive to the stopping power. Despite the possible systematic error pointed out above, the experimental data implied that the nuclear stopping power assumed in

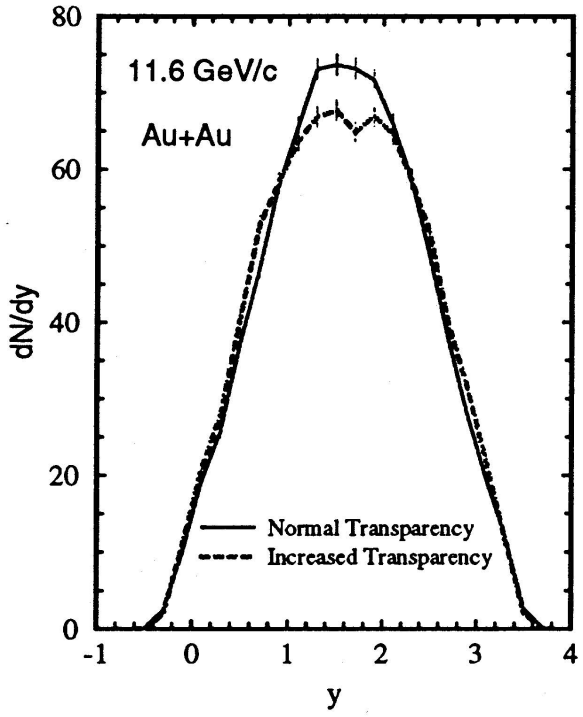

Figure 7.3.9: Rapidity distributions of protons calculated by ARC with different nuclear stopping power [92]. Solid line: calculation with the standard set of parameters. Broken line: calculation with increased transparency, or equivalently reduced nuclear stopping power.

the models was too strong, especially in RQMD, and that they may have thereby overestimated the highest achieved baryon density also. As thus expected, the highest baryon densities found in the central part of the collision system in the cascade calculations [18, 19] showed a negative correlation to the width of the rapidity distribution of protons σ_y^p, as shown in Figure 7.3.10. The baryon density achieved in central Au+Au collisions at 11 A GeV/c can be hence inferred to be somewhat lower than the predictions of the models, and can be estimated grounded on the cascade model calculations to be 1.2 – 1.3 fm^{-3}, or 7 – 8 times higher than the normal nucleus density, from the experimentally observed proton distribution with $\sigma_y^p = 1.20$.

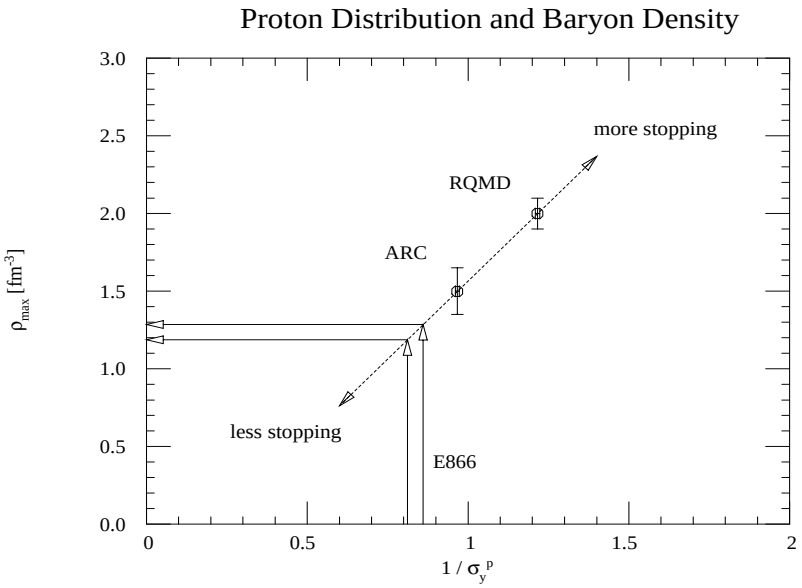

Figure 7.3.10: The r.m.s. width of the rapidity distributions of protons and the highest baryon densities found in cascade simulations of central (4 %) Au+Au collisions at the AGS energy [18, 19]. Also shown are the experimentally observed width of proton rapidity distribution and an estimate of the achieved baryon density.

7.3.4 Collective Effects

Another interesting phenomenon observed in relativistic Au+Au collisions was suppression in the transverse-mass spectra of protons in the low transverse-kinetic-energy regions, especially around the center-of-mass rapidity. It has been always a question with relativistic heavy-ion physics whether the system can be described as a superposition of p+p or p+A collisions. As presented in Section 7.2, the observation was uniquely associated with the heavy system of Au+Au, and hence could be regarded as a signature of collective effects[§], *e.g.* radial expansion of the collision system [76, 77]. The mechanism determining the shape of the proton spectra is investigated below, employing cascade model calculations.

[§]Here we use a technical term "collective" to denote regulated motion of a number of particles such as a hydro-dynamical flow, which can originate from, for example, multiple scattering. It has a different concept from the same term used in nuclear physics referring to a long-range correlation.

7.3.4.1 Proton Spectra in RQMD

As seen in Figure 7.3.6, both RQMD and ARC failed to reproduced the flat transverse-kinetic-energy distribution of protons around the center-of-mass rapidity; the flatness of proton spectra in nucleus-nucleus collisions has been an unsolved problem with cascade models even with lighter systems such as Si+A [74]. Though the predictions of the two cascade models are globally similar to each other, a notable difference was in the shapes of the spectra especially in the mid-rapidity region. RQMD qualitatively reproduced the convex shape of the transverse-mass spectra of protons suppressed at low transverse kinetic energies, while the spectra predicted by ARC were closer to the single-exponential form. Before discussions on the mechanism determining the shape of the proton spectra, let us compare the calculation of RQMD with the experimental data and discuss to what extent the model could reproduce the data.

The transverse-mass spectra of protons in the RQMD events were fitted with the double-exponential formula (Equation 6.2.2). The result is shown in Figure 7.3.11 to be compared with the experimental data in Figure 6.2.8. In the plot of the rapidity density dN/dy, the circles represent the results of fitting and the histogram is the actual number of protons in the calculation. Their agreement demonstrates the small systematic error ($\sim$ 1 %) originating from the parameterization and the fitting procedure. From the comparison, it can be seen that the reproduction of the spectra by RQMD was not on the quantitative level. The model could not predict the large values of inverse slope parameters obtained from the experimental data, *i.e.* the high fraction of particles with high transverse kinetic energy, as mentioned above. The values of w, representing the extent of deviation from the single-exponential formula, were also consistently smaller compared to the experimental result.

7.3.4.2 Mechanism to Deviate Proton Spectra

Cascade models, RQMD and ARC, were employed as tools to investigate the mechanism from which the deviation of proton spectra from the single-exponential formula originated. As noted above, RQMD reproduced the convex shape of the transverse-mass spectra of protons in the mid-rapidity region though only qualitatively, while ARC predicted spectra which were consistent with the single-

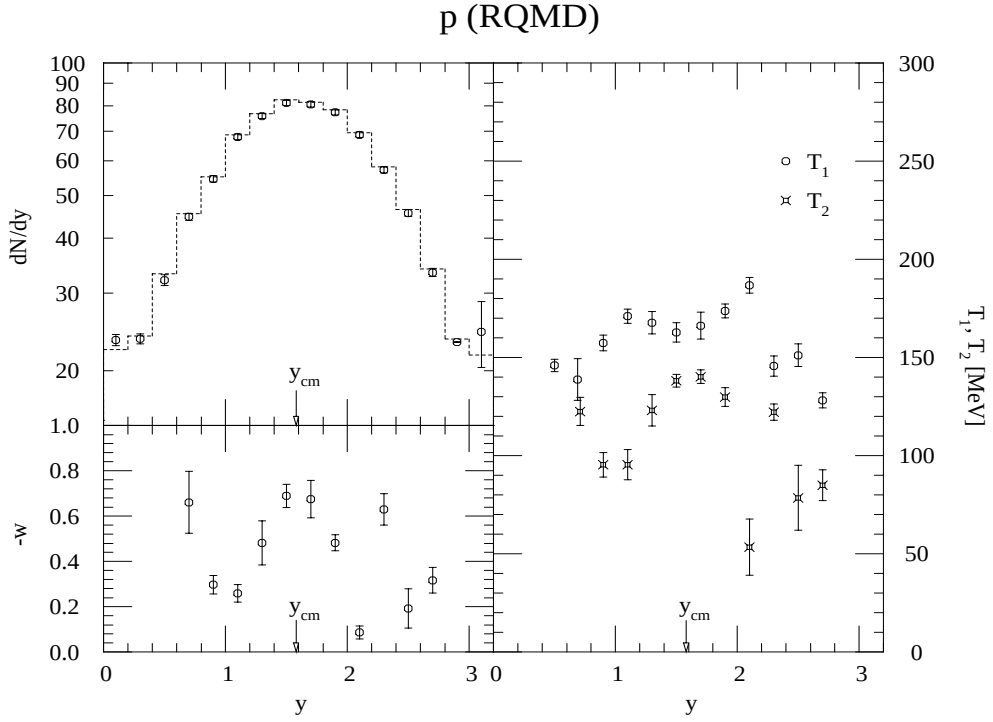

Figure 7.3.11: The rapidity distribution, suppression factor, and inverse slope parameter of protons in RQMD events simulating central (4 %) Au+Au collisions at 11.7 A GeV/c. The histogram in the plot of rapidity distribution dN/dy represents the actual number of protons in the calculation, while all the other points show the results of fitting (see text for details). The error bars indicate the statistical errors only. See Section 6.2 for the definitions of w, T_1, and T_2.

exponential formula. The different behavior of the two models may be a clue to understanding of the mechanism. To investigate what kind of collective effects affects and determines the shape of the proton spectra, the two cascade models were studied and were compared with each other.

In microscopic cascade models such as RQMD and ARC, collective effects have been incorporated primarily through rescattering of secondary particles, whose contribution should appear as so-called shadowing effect especially in massive (*i.e.* large) systems. Because of scattering with other existent hadrons, particles emitted from the peripheral region of a collision system are to be prevented from going toward the center of the system and be regulated to form an outward flow. The effect should appear as an angular correlation between transverse momentum p_t and emission point x with respect to the center of the collision, and be represented by a distribution of a correlation angle ϕ_{cor} which is defined as

$$\phi_{cor} \equiv \cos^{-1}\left(\frac{\vec{p_t}\cdot\vec{x}}{|p_t|\,r_t}\right) , \tag{7.3.1}$$

where r_t is the transverse distance from the beam axis to the emission point. Distributions of the correlation angle ϕ_{cor} are shown in Figure 7.3.12 for RQMD and ARC, demonstrating a strong shadowing effect and similarity of the two models.

Let us look into the collective effects in a more direct way. Figure 7.3.13 shows the distributions of outward transverse momentum p_{out} of protons in the mid-rapidity region in the cascade models, as a function of transverse distance r_t from the beam axis to the emission point. Here, p_{out} is defined as

$$p_{out} \equiv \cos\phi_{cor}\cdot p_t , \tag{7.3.2}$$

where ϕ_{cor} is the correlation angle defined above, and p_t is the transverse momentum. Particles emitted from the outer region of the collision system are observed to be more strongly boosted outwards, showing existence of a regulated flow, or in other words, radial expansion of the system. Moreover, the correlation between the emission point and the distribution of outward transverse momentum should be a measure of the extent of the radial flow. As shown in the figure, the two models displayed very similar correlations. ARC might be expected to show a less flow considering the behavior of the proton spectra, but it even had a slightly

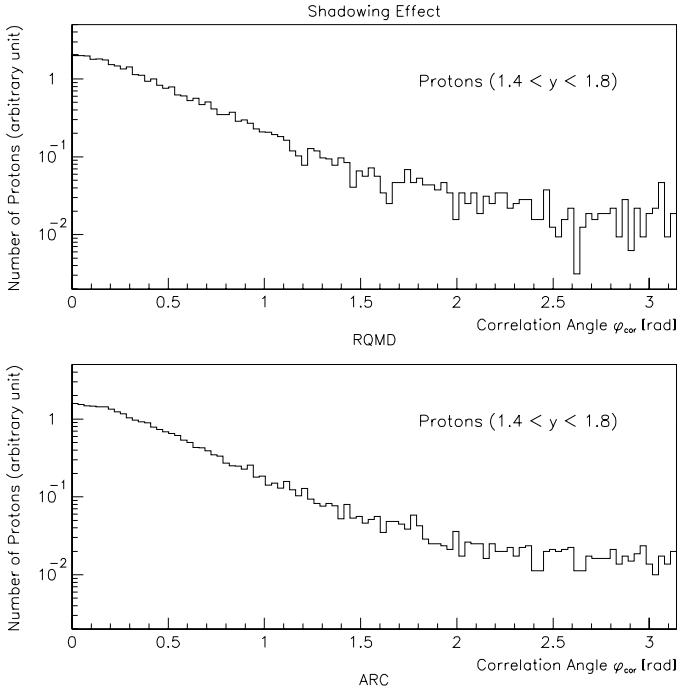

Figure 7.3.12: The angular correlations for protons in RQMD (upper) and ARC (lower) between transverse emission point and transverse momentum. The abscissa ϕ_{cor} represents the extent of the correlation; see text for its definition. A rapidity range of $(y_{cm} \pm 0.2)$ is selected.

stronger correlation than RQMD. The upshot is that the different shapes of the proton spectra predicted by RQMD and ARC did not originate from a difference in the extent of the shadowing effect nor of the radial flow built in the models.

Another observable which may reflect the collective effects in the cascade models is the distribution itself of transverse emission point of hadrons, which is defined in those models as where the *freeze-out* of the particle occured, *i.e.* the position of the last stochastic scattering or decay. If there occurs no rescattering, transverse distance from the beam axis to the emission point would distribute with a sharp edge with a maximum value corresponding to the initial size of the colliding nuclei. Figure 7.3.14 shows the distributions for protons in the mid-rapidity region in the cascade models. It can be seen that RQMD predicted more protons emitted from the outside of the initial volume of the collision system, compared to ARC.

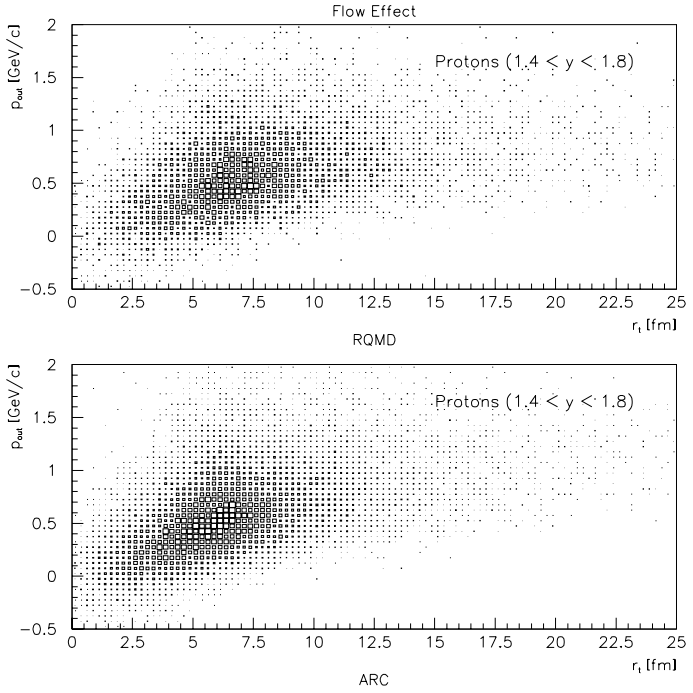

Figure 7.3.13: The correlations in RQMD (upper) and ARC (lower) between transverse distance r_t from the beam axis to the emission point of a proton and outward transverse momentum p_{out}, showing an effect of a radial flow of the collision system. A rapidity range of $(y_{cm} \pm 0.2)$ is selected.

As presented above, those protons emitted from the peripheral region, or *flare*, are to be more influenced by the radial flow of the system than those from the central region, or *core*. In the cascade models, protons from the flare actually showed spectra boosted outwards as shown in Figure 7.3.15, while those emitted from the inside of the core was well described with the single-exponential formula both in RQMD and ARC. Figure 7.3.15 also demonstrates the origin of the dissimilar proton spectra in the two models owing to different fractions of protons from the flare. While the contribution of the flare was too small in ARC to be observed in the final spectra of protons, it was $2-3$ times more in RQMD, enabling the model to reproduce the observed convex shape of the spectra at least qualitatively.

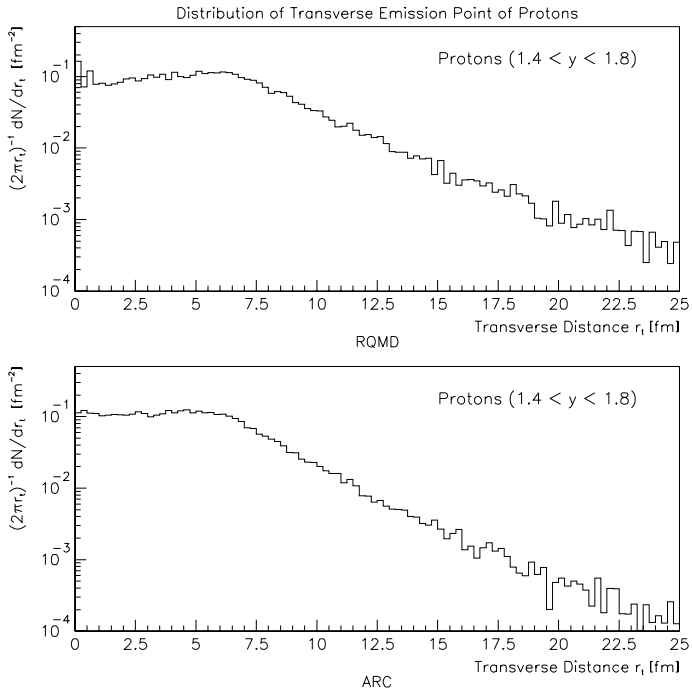

Figure 7.3.14: The distributions of transverse distances r_t from the beam axis to the emission (freeze-out) points of protons in RQMD (upper) and ARC (lower). A rapidity range of $(y_{cm} \pm 0.2)$ is selected.

7.3.4.3 Remarks

A comparison between two microscopic cascade models of relativistic nucleus-nucleus collisions, RQMD and ARC, exhibited that the contribution of particles boosted by a regulated outward flow, or radial expansion, of a collision system could give rise to the deviation of proton spectra from the single-exponential scaling. Since the experimentally observed deviation in the mid-rapidity region was even stronger than that in the cascade models, the effect of a radial flow is suggested to be important in description of the dynamics of relativistic heavy-ion collisions. A further discussion on the deviation is given in Section 7.4, employing a hydro-dynamical collective-flow model.

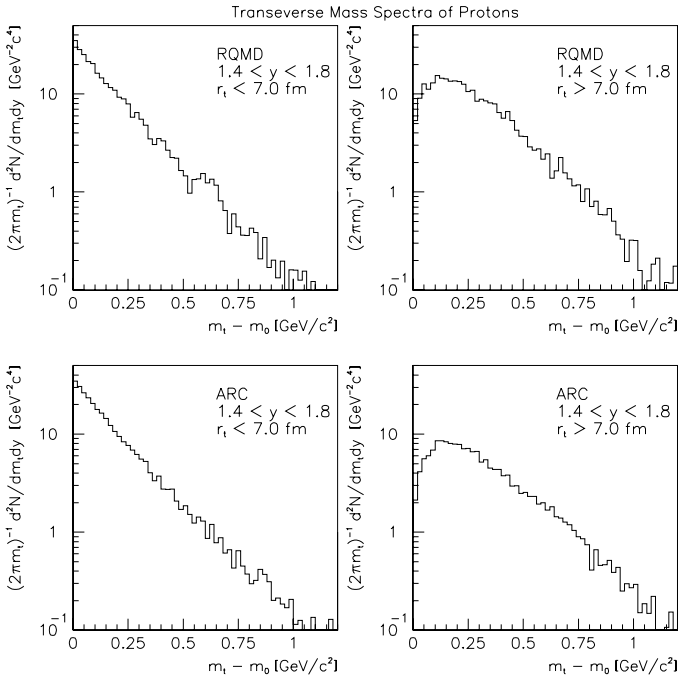

Figure 7.3.15: Model calculations of invariant differential yields of protons in central (4 %) Au+Au collisions at the AGS energy, with a cut on the transverse emission point, with RQMD (upper) and ARC (lower). The figures are shown as a function of transverse kinetic energy ($m_t - m_0$). Left two figures show spectra of protons emitted from the central region of the collision system, *i.e.* with the transverse distance r_t less than 7.0 fm; right two figures are for protons emitted from the outside of the initial nuclei, *i.e.* with r_t larger than 7.0 fm. A rapidity range of ($y_{cm} \pm 0.2$) is selected.

7.3.5 Conclusions

As discussed in the preceding subsections, there exist some aspects of Au+Au collisions at the AGS energy which cannot be reproduced by the present cascade models, even though the models are generally successful to describe the heavy collision system as well as lighter systems at the energy region. Further theoretical work is thereby awaited to elucidate the mechanism causing the effects which are associated with such massive collision systems. Here we summarize the discussions based on the cascade models.

Microscopic cascade models of nucleus-nucleus collisions, RQMD and ARC, reasonably well reproduced the distributions of $\pi^{\pm}$. Though RQMD overestimated their absolute yields, related to the strong nuclear stropping power in the model, the slopes of the transverse-mass spectra of $\pi^{\pm}$ and the shapes of their rapidity distributions were reproduced by the both models. In rapidity regions far from the center of mass, the models and the measurement agreed with each other also for heavier particles such as protons. From the rapidity distribution of protons, it was found that the nuclear stopping power assumed in the both models was too strong; it should be reflected in the future improvement of the models.

In the mid-rapidity region, the models failed to reproduce the flat spectra of K^+ and protons, as already known in Si-induced reactions [74]. Another fact which experimentally suggested existence of an additional effect to the simple cascade picture was a deviation from the single-exponential scaling of the transverse-mass spectra of mid-rapidity protons in central Au+Au collisions. The deviation, or a suppression in the low transverse-kinetic-energy regions, was not observed at the AGS energy with lighter collision systems. The cascade models supported a picture with a radial flow as a candidate to describe the massive collision system, by showing an outward flow built through rescattering of hadrons. One of the models, RQMD, actually gave rise to the deviation through the contribution of the expanding peripheries of the collision system, though the effect in the present models may not be enough to interpret the observation.

7.4 Hydro-Dynamical Collective-Flow Model

As discussed in Section 7.3, microscopic cascade models of relativistic nucleus-nucleus collisions could not reproduce the behavior of the transverse-mass spectra of heavy particles in the mid-rapidity region, while they were successful to describe $\pi^{\pm}$ and also protons in the rapidity region far from the center of mass. The question of the flatness of the spectra of protons in relativistic nucleus-nucleus collisions therefore has not been solved with the approach. In this section, we investigate the variation of the slopes of the transverse-mass spectra of hadrons with different masses, as well as the deviation of the proton spectra from the single-exponential scaling, in the mid-rapidity region of Au+Au collisions using a hydro-dynamical collective-flow model.

7.4.1 Basics of Hydro-Dynamical Model

A hydro-dynamical collective-flow model is an approach to understand the mechanisms of relativistic heavy-ion collisions as an expanding fireball, by use of thermodynamical parameters such as temperature and entropy. Let us employ a simple model assuming spherical expansion of a thermal source [77]. In the expansion stage of a collision, the evolution of the system can be described in terms of baryon number, energy, and entropy conservation. The profile of the flow velocity $\beta_f(r)$ is parameterized for the spherical expansion as a function of radial distance r from the center, with the power n, as

$$\beta_f(r) = \left(\frac{r}{R}\right)^n \beta_s \ , \tag{7.4.1}$$

where R is the time-dependent radius of the expanding fireball and β_s is the time-dependent surface velocity. The freeze-out of the system is assumed to occur when the mean collision time of the particles exceeds the time scale of the rarefaction. Then the general form of the transverse-mass spectra can be obtained as

$$\frac{dN}{m_t dm_t} \propto \int dy \int_0^R r^2 dr E e^{-\frac{\gamma_f E}{T}} \left\{ \frac{\sinh\alpha}{\alpha} + \frac{T}{\gamma_f E}\left(\frac{\sinh\alpha}{\alpha} - \cosh\alpha\right)\right\} \tag{7.4.2}$$

$$\gamma_f \equiv \frac{1}{\sqrt{1-\beta_f^2}} \tag{7.4.3}$$

$$\alpha \equiv \frac{\beta_f \gamma_f p}{T} , \tag{7.4.4}$$

where E and p are the total energy and the momentum of the particle, respectively, and T is the temperature of the thermal source at the freeze-out time.

It must be noted that the model can be applied to compare with experimental data only in the transverse direction in the center-of-mass frame, *i.e.* around the center-of-mass rapidity, since it assumes spherical expansion of the system, not cylindrical with a longitudinal component which is more realistic. In fact, the model is known not to be capable to reproduce rapidity distributions of produced particles [77]. We hence examine the particle spectra only around the center-of-mass rapidity with the model.

7.4.2 Analysis Results

Prior to looking into the experimental data using the hydro-dynamical collective-flow model, let us see a general tendency of spectra predicted by the model. Figure 7.4.1 shows the shapes of spectra of π^+, K^+, and protons calculated with the model with different values of the power n which determines the shape of the velocity profile. The other parameters, the temperature of the thermal source T and the surface velocity β_s, were fitted with the experimental data which are also shown in the figure.

The case with $n = 0.0$ corresponds to expansion with a uniform velocity across the entire volume, and $n = 1.0$ means a uniform expansion rate. The power n had been historically considered to be ~ 2.0, but $n = 2.0$ gives a concave spectrum for protons, as well as for lighter particle species. As seen in the figure, the power n must be less than 1.0 to reproduce the convex shape of the proton spectra.

The transverse-mass spectra of π^+, K^+, and protons around the center-of-mass rapidity in central Au+Au collisions at 11 A GeV/c were fit with the hydro-dynamical model (Equation 7.4.2) with three free parameters (T, β_s, and n) beside the normalization factors. The results are listed in Table 7.4.1 with the χ^2 of the fitting; the table also includes the results with fixed values of n. Figure 7.4.2 shows the best-fitted curves with the obtained power $n = 0.50 \pm 0.10$. As is seen, the hydro-dynamical collective-flow model successfully reproduced the different slopes of the particles with different masses, as well as the deviation of the proton spectra from the single-exponential scaling. The obtained temperature of the

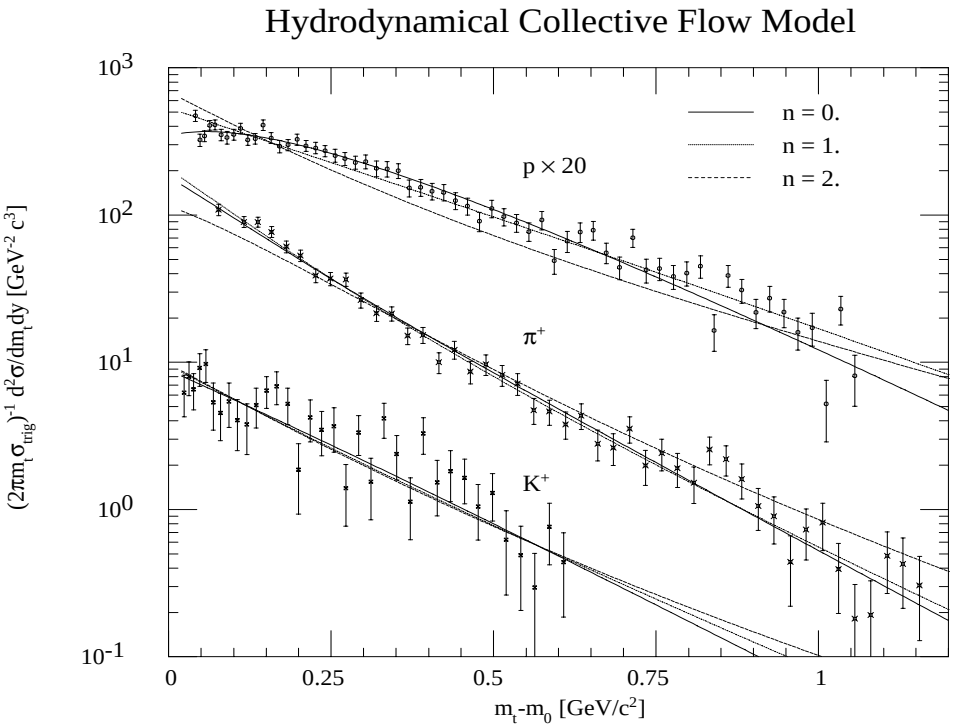

Figure 7.4.1: A tendency of spectra predicted by a hydro-dynamical collective-flow model with different velocity profiles represented by the power n. Fitting was performed with the transverse-mass spectra of π^+, K^+, and protons around the center-of-mass rapidity ($y = 1.7$ for π^+ and 1.5 for K^+ and protons) in central Au+Au collisions at 11 A GeV/c. See text for a description.

n	T [MeV]	β_s	χ^2 / DOF	Remarks
0.00	95.8 ± 2.0	0.580 ± 0.005	179.5 / 136	uniform velocity
0.50 ± 0.10	91.2 ± 2.6	0.689 ± 0.025	172.9 / 135	best fit of n
1.00	88.6 ± 2.5	0.798 ± 0.009	220.1 / 136	uniform expansion
2.00	116.2 ± 2.5	0.861 ± 0.015	508.5 / 136	historically used

Table 7.4.1: The results of fitting to a hydro-dynamical collective-flow model of the transverse-mass spectra of π^+, K^+, and protons around the center-of-mass rapidity (y = 1.7 for π^+ and 1.5 for K^+ and protons) in central Au+Au collisions at 11 A GeV/c. The errors listed are statistical only.

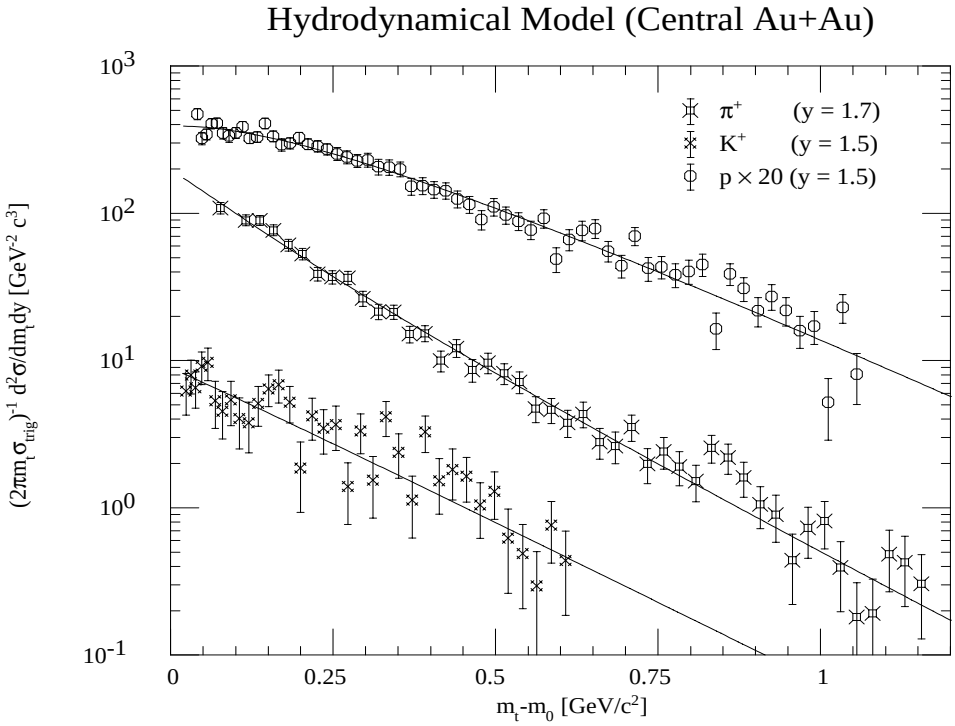

Figure 7.4.2: A fit with a hydro-dynamical collective-flow model of the transverse-mass spectra of π^+, K^+, and protons around the center-of-mass rapidity (y = 1.7 for π^+ and 1.5 for K^+ and protons) in central Au+Au collisions at 11 A GeV/c. The power n was also fitted as a parameter. See text for a description.

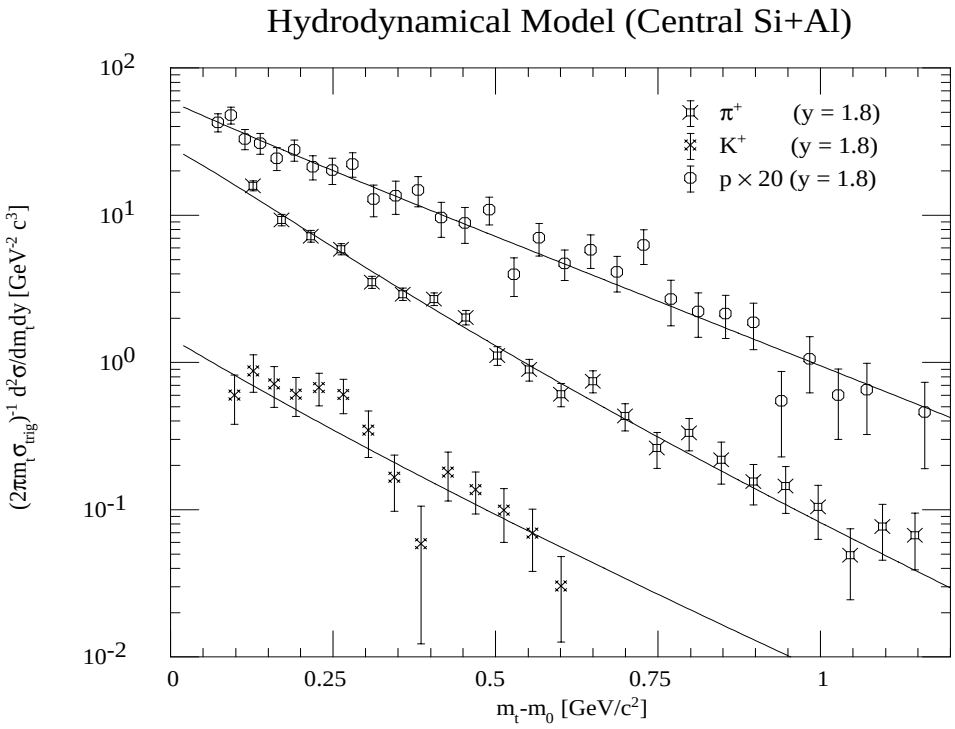

Figure 7.4.3: A fit with a hydro-dynamical collective-flow model of the transverse-mass spectra of π^+, K^+, and protons around the center-of-mass rapidity ($y = 1.8$) in central Si+Al collisions at 14.6 A GeV/c (data are taken from Reference [28]). The power n was also fitted as a parameter. See text for a description.

thermal source T was 91.2 ± 2.6 MeV, and the surface velocity β_s was 0.69 ± 0.03.

The model was also applied to analyze the data from central (7 %) Si+Al collisions at 14.6 A GeV/c measured by the E802 experiment. Figure 7.4.3 shows the spectra of π^+, K^+, and protons at $y = 1.8$ with the best-fitted curves. In the light collision system, the value of n was found to be 1.22 ± 0.31, *i.e.* consistent with 1.0 which corresponds to expansion with a uniform rate across the entire volume of the fireball. Table 7.4.2 lists the temperature and the surface velocity in central Si+Al and central Au+Au collisions, fitted with the same velocity profile with the power n fixed at 1.0. While the obtained values of T were consistent with each other, the Au+Au collisions led to a larger surface velocity β_s, which means a stronger outward flow based on the model.

	T [MeV]	β_s	χ^2 / DOF
Si+Al (central)	97.3 ± 4.3	0.706 ± 0.023	70.3 / 66
Au+Au (central)	88.6 ± 2.5	0.798 ± 0.009	220.1 / 136

Table 7.4.2: The results of fitting to a hydro-dynamical collective-flow model with the power $n = 1.0$, for central (7 %) Si+Al collisions at 14.6 A GeV/c (data are taken from Reference [28]) and for central (4 %) Au+Au collisions at 11 A GeV/c. The errors listed are statistical only.

7.4.3 Conclusions

The observed slopes of the transverse-mass spectra of various hadrons and the deviation of the proton spectra from the single-exponential scaling were examined using a hydro-dynamical collective-flow model, around the center-of-mass rapidity in central Au+Au collisions at 11 A GeV/c. The model well described the both aspects of observation, which microscopic cascade models could not reproduce. That supports the importance of collective effects in description of relativistic heavy-ion collisions, at least in the mid-rapidity region. Based on the model, the temperature of the thermal source obtained for Au+Au collisions and for a lighter system of Si+Al was consistent with each other ($\sim$ 90 MeV). It should be noted that the temperature does not directly represent the initial conditions of the fireball, but the freeze-out temperature of the hadrons. The flow velocity of the expanding surface of a fireball was implied to be larger in the heavier system.

7.5 Consideration and Remarks

Standing on the studies using microscopic cascade models and a hydro-dynamical collective-flow model, here we summarize a possible picture to describe Au+Au collisions at the AGS energy.

First of all, calculations of cascade models of nucleus-nucleus collisions reasonably agreed with the experimental data. Two cascade models which have been developed to be applied in the energy region, RQMD and ARC, globally reproduced hadron production in the massive collision system, as they have done with lighter systems. In other words, outlines of the collision dynamics can be

described in a cascade picture based primarily on nearly independent binary collisions of hadrons.

At the mid-rapidity region, however, the models could not reproduce the flat spectra of heavy particles, only through the cascade picture with rescattering. The slopes of the spectra of various hadrons around the center-of-mass rapidity were described in a unified way by a simple hydro-dynamical model with a collective flow, though the model is only applicable to the rapidity region. The hydro-dynamical model also succeeded to reproduce the deviation of the proton spectra from the single-exponential scaling by choosing an appropriate profile of the flow velocity. The success of the hydro-dynamical model may suggest existence of a collective effect beyond the simple multiple scattering treated in the cascade models, at least in the mid-rapidity region, in relativistic heavy-ion collisions.

The AGS-E877 experiment recently reported observation of unpredictably anisotropic energy emission in Au+Au collisions with *medium* centrality, through measurement of azimuthal distributions of forward and backward energy emission [93]. If a collective flow is formed on the reaction plane in semi-central collisions, the flow is intuitively expected to directed sideward, *i.e.* around the center-of-mass rapidity, in collisions with less impact parameters in which the reaction plane can no longer be well defined. The picture is consistent with the observation of the E866 experiment and the discussions given in this chapter. On the subject, yet, more experimental and theoretical studies are necessary to identify the origin of the effects.

Chapter 8

Summary and Concluding Remarks

Utilizing the newly available ^{197}Au beam at 11 – 12 A GeV/c at the Alternating Gradient Synchrotron (AGS) at Brookhaven National Laboratory, we performed the AGS-E866 experiment aiming at systematic studies of semi-inclusive spectra of various identified hadrons from relativistic heavy-ion collisions, extending the studies performed by the E802/859 experiments with the lighter beams to heavier collision systems such as ^{197}Au+^{197}Au. To deal with the experimental difficulties encountered with the Au beam, we constructed a new forward-angle spectrometer which was designed for operation under a high particle-density condition. Features of the experiment included

1. a wide kinematic coverage,
2. event characterization by the centrality of collisions,
3. high capability of particle identification.

The first data with the Forward Spectrometer were taken in October, 1993; the spectrometer was found well functioning even at the most forward angle of 6 degrees with respect to the incident beam.

With the Forward Spectrometer, production of various hadrons were studied for Au+Au collisions at 11 A GeV/c, in the angular range from 6 degrees to 25 degrees in the laboratory frame with respect to the incident beam. Single particle spectra were measured and analyzed in the momentum ranges above 0.45 GeV/c,

and up to 4.0 GeV/c for charged pions ($\pi^{\pm}$), 3.0 GeV/c for positively charged kaons (K^{+}), and 5.0 GeV/c for protons. Most importantly, proton spectra in the mid-rapidity region were measured for the first time in such a massive collision system as Au+Au at the AGS energy.

For central Au+Au collisions, the Forward Spectrometer data taken in October 1993 showed an agreement within $\pm$ 10 % with a preliminary analysis of the first Au beam data taken with another arm of magnetic spectrometer, the Henry Higgins. From the combined data set taken with the two spectrometer arms, the following results were obtained through comparisons with the experimental results of the E802 experiment with lighter collision systems:

1. The rapidity distribution of protons presented a single peak around the center-of-mass rapidity, which has not been observed in lighter collision systems such as ^{28}Si-induced reactions, suggesting strong nuclear stopping.

2. The single-exponential scaling of transverse-mass spectra, which has been found with secondary particles in p+p collisions and also has been regarded to be applicable to particles produced in p+A and A+A collisions, was no longer effective for all produced particle species. The transverse-mass spectra of protons showed a convex shape, or suppression at low transverse kinetic energies, while π^{-} showed enhancement in the similar transverse-kinetic-energy regions.

The latter observation in the proton spectra could be regarded as a result of collective effects, since it was uniquely associated with massive collision systems.

To examine the experimental results, we introduced two microscopic cascade simulators of nucleus-nucleus collisions, RQMD and ARC. From comparisons between our data and calculations of the cascade models, we found results as follows:

1. The both models generally reproduced the experimental data. In the mid-rapidity region, however, the flat spectra of heavy particles such as protons could not be reproduced.

2. The convex shape of the proton spectra was qualitatively reproduced by RQMD, while the behavior of ARC follows the single-exponential scaling.

3. The observed peak of the rapidity distribution of protons around the center of mass was wider than predicted by the cascade models by 15 – 45 %.

Among these, the last suggested that the nuclear stopping power being assumed in the cascade models was too strong. According to the models, the stopping power has a positive correlation to the baryon density achieved in the collision system. The actually achieved baryon density should be thereby expected to be lower than predicted by the models, and was estimated to be 7 – 8 times higher than the normal nucleus density grounded on the cascade models.

To understand the behavior of protons which are characteristic of massive collision systems, collective effects were investigated from the different behavior of the two cascade models. In the both models, a radial outward flow was built through rescattering of hadrons, and RQMD reproduced the observed convex spectra of protons at least qualitatively through the contribution of protons emitted from the expanding peripheries of the system. Considering that the experimental result showed an even stronger deviation from the single-exponential scaling, an effect of a radial flow is implied to contribute importantly in description of the collision dynamics.

As an approach to explain the flatness of the proton spectra in relativistic nucleus-nucleus collisions, we employed a hydro-dynamical collective-flow model. The model successfully described two aspects of the observation which could not be reproduced by the present cascade models: the variation of the slopes of the transverse-mass spectra of hadrons with different masses, and the shapes of the spectra. Based on the model, the temperature of the thermal source and the velocity of the expanding surface were estimated to be ~ 90 MeV and $\sim 0.7\ c$, respectively, at the freeze-out time. A comparison with a lighter system of Si+Al implied that the surface velocity is larger in the larger system.

As a conclusion, a cascade picture with rescattering is generally successful to describe the dynamics of relativistic heavy-ion collisions. Existence of a collective effect beyond the simple cascade with multiple scattering may be, however, suggested at least in the mid-rapidity region by the success of the hydro-dynamical collective-flow model. In order to identify the origin of such an effect, more experimental and theoretical studies are waited for.

With the invalidness of the single-exponential scaling of transverse-mass spectra, it should be stressed that a wide kinematic coverage is important in studies

of hadron production in relativistic heavy-ion collisions, especially with massive collision systems such as Au+Au or Pb+Pb. It encourages us to further proceed studies of single particle spectra with the two-arm spectrometer system of the E866 experiment, as well as studies of two particle correlations and resonances which are being planned and/or carried out. Also, the E866 experiment has recently been equipped with devices which can measure the azimuthal distributions of beam fragments and produced particles in the mid-rapidity region. The possible effect of a collective flow discussed in this thesis will be further investigated in conjunction with those devices, as a function of centrality and direction with respect to the reaction plane.

Acknowledgments

It is a great pleasure to express my sincere gratitude to Prof. R. S. Hayano. Without his introduction, I would not even have my teeth into relativistic heavy ion experiment. I thank him not only for having led me to the exciting field of physics, but for his persevering encouragement and appropriate advice. Special thanks are due to Dr. H. Hamagaki and Dr. Y. Akiba for their continuous guidance, fruitful discussions, and zealous support in many aspects. Dr. H. Hamagaki has led the Forward Spectrometer project as a co-spokesperson of the AGS-E866 experiment. His abundant knowledge has always stimulated and guided me. I am much obliged to Dr. Y. Akiba for his help in the data analysis and valuable advice, as well as for his earnest proof reading of my manuscript of this thesis.

I wish to acknowledge all the collaborators of the E866 experiment. My work would never be completed without their great efforts and collaboration. I especially thank the *Forwardians* for their help and friendship. I express my thanks to Mr. H. Sako with whom I have spent almost three years working on the time projection chambers and on off-line data analysis. I owe Dr. Z. Chen and Dr. F. Zhu, who constructed, maintained, and analyzed the forward drift chambers, for their help and useful advice. I am also grateful to Ms. S. Ueno-Hayashi for her extensive calibration of the time-of-flight wall. I appreciate Dr. K. Kurita and Mr. H. Kaneko, a half Forwardian, for discussions and their kind help, particularly in handling of an analysis tool for cross section evaluation. I would like to thank Prof. Y. Miake for his complicated but probably sincere encouragement, and to Dr. S. Hayashi for his hospitality and friendship during the first months of my stay at BNL. I would also like to say thanks to Dr. H. Sakurai, who made a prototype of the time projection chambers, for his guidance, advise, and being always happy, and to Dr. Y. Tanaka, the author of the cross section analysis tool, for his help and encouragement. I am under a special obligation to Dr. D. Beavis

for his efforts and arrangements as a *liaison physicist* of the experiment. I am also grateful to Dr. J. H. vanDijk for fruitful discussions and kind advice on tracking chambers.

I acknowledge Dr. C. Chasman, the leader of the heavy ion research group at BNL and a co-spokesperson of the experiment, for his hospitality, various arrangements for my activity at BNL, and hearty encouragement. My sincere thanks are also due to Ms. C. Feliciano, a very kind and able group secretary, for her hospitality and guidance for a stranger in the United States. I appreciate Dr. S. G. Steadman for his great effort to organize the collaboration as a co-spokesperson. I would also like to thank Prof. S. Nagamiya for his guidance, precious advice, and encouragement. The original idea of the E802/859/866 experiments owes him greatly. I am grateful to Prof. S. Homma for his support and encouragement, in particular during my stay at INS, the University of Tokyo, to complete this thesis. Special thank are due to Dr. K. Ashktorab, Dr. B. A. Cole, Dr. R. Debbe, Dr. J. H. Lee, Dr. B. Moskowitz, and Dr. F. Videbaek for their indispensable help, support, advice, and encouragement. I also thank Mr. and Mrs. A. Kumagai for their friendship.

I am obliged to Dr. O. Sasaki, who designed the readout modules for the time projection chambers, for his valuable advice and kind help. I would like to acknowledge Mr. K. Asselta, Mr. E. Baker, Mr. H. Diaz, Mr. J. Dioguardi, Ms. E. McBreen, Mr. R. A. Scheetz, and Mr. Y. Matsuyama, for their technical support, help, and kindness. I am also grateful to Dr. S. H. Kahana and Dr. D. Kahana, two of the authors of ARC, for fruitful discussions and precious comments, and to Dr. H. Sorge, the main author of RQMD, for his comments on my discussions based on the cascade models.

Here I acknowledge all the members of the nuclear experiment group at the University of Tokyo. I express my special thanks to Dr. H. Tamura for reading my manuscript of this thesis earnestly and giving me instructive and indispensable comments and advice. I am under a particular obligation to Prof. M. Ishihara and Prof. H. Sakai for their encouragement and truly relevant advice throughout my student days.

I wish to express my thanks to the staffs of the heavy ion accelerator facility at BNL, from the tandem to the AGS, for delivering the Au beam. I am under an obligation to the Japan Society for the Promotion of Science for a fellowship. The

E866 experiment is supported in part by the U.S. Department of Energy under contracts with ANL, BNL, the University of California at Riverside, Columbia University, LLNL, and MIT, in part by NASA under a contract with the University of California, and by the U.S.-Japan High Energy Physics Collaboration Treaty.

At last, but not least, I express my appreciation to my family members and members-to-be, especially to my parents and Miss H. Baba. It was entirely due to their support and encouragement that I could accomplish my aspiration. And among others, I cannot thank Miss H. Baba enough for her devoted moral support and her presence by my side.

Appendix A

Kinematic Variables

Here we describe the definitions and notations of kinematic variables used in this thesis.

Choosing the beam direction as the z-axis, the rapidity y of a particle with the total energy E and the momentum in the beam direction p_z is defined as

$$y \equiv \frac{1}{2}\ln\left(\frac{E+p_z}{E-p_z}\right) \tag{A.0.1}$$

$$= \tanh^{-1}\frac{p_z}{E}\ . \tag{A.0.2}$$

The rapidity is transformed under a boost in the z-direction with the velocity β as

$$y \rightarrow y + \tanh^{-1}\beta\ ; \tag{A.0.3}$$

the shape of a rapidity distribution is hence Lorentz invariant.

The transverse momentum p_t and transverse mass m_t are defined as

$$p_t^2 \equiv p_x^2 + p_y^2 \tag{A.0.4}$$

$$m_t^2 \equiv m_0^2 + p_t^2\ , \tag{A.0.5}$$

where m_0 is the rest mass of the particle. Rapidity y and transverse mass m_t also have relations as follows:

$$E = m_t \cosh y \tag{A.0.6}$$

$$p_z = m_t \sinh y\ . \tag{A.0.7}$$

Appendix B

Cascade Models of Nucleus-Nucleus Collisions

Features of two microscopic cascade models of relativistic nucleus-nucleus collisions, RQMD and ARC, are presented here. They can be used at the AGS energy and are used for discussions in this thesis. Their basic ideas and ingredients are summarized below.

B.1 RQMD

RQMD (Relativistic Quantum Molecular Dynamics) has been developed at Frankfurt University, to be applied in the energy range from the AGS to the CERN-SPS. The model is a combination of classical propagation of hadrons and quantum effects such as stochastic scattering, particle decay, and Pauli blocking in collisions. Color string formation and fragmentation are also used to describe particle production from decay of high-mass resonances (above 2 GeV/c^2 for non-strange baryons), mainly to handle the energy region of the SPS. A difference of RQMD from the non-relativistic QMD model is Lorentz invariance; instead of the propagation with a non-relativistic Hamiltonian in QMD, RQMD uses equations of motion which are Lorentz invariant.

As a principle, the model includes as input parameters as many experimental data as available on reaction cross sections and decay probabilities. For reactions whose parameters are experimentally undetermined, *e.g.* π-K collisions, the model assumes their cross sections following several guiding principles such as

isospin invariance, hadron universality in highly energetic collisions, the angular dependence of cross sections, time reversal invariance, and so on. It has, however, a few free parameters to be fixed yet. An example is the formation time of hadrons produced in the jets, *i.e.* the time duration after a string fragmentation till the secondary particles can rescatter, which is currently set at 1 fm/c regardless to the mass of the particle, while a heavier particle needs more time to be produced in the string decay philosophy. For more details of the model, see, for example, Reference [84].

B.2 ARC

ARC (A Relativistic Cascade) is a simulation code developed at BNL to describe nucleus-nucleus collisions at the AGS energy based only on a hadronic picture. Particle production in the model is achieved through low-mass resonances such as Δ and ρ. This is motivated by an examination of p+p collisions at 12 and 24 GeV/c in the laboratory frame [94], showing that a majority of inelastic collisions yields final states containing one or more such resonances. The finite lifetimes of the resonances effectively play the role of so-called formation time of secondary particles in other models. On the other hand, it is a possible cause of the less stopping of incident nucleons in the model compared to RQMD that ARC includes only low-mass resonances and hence cannot transform much kinetic energy into excitation energy. Input parameters of two-body reactions in the code are adjusted so that it reproduces experimental data of relevant cross sections and transverse-momentum distributions in p+p and p+A collisions at 12 – 24 GeV/c. For details of the model, see, for example, Reference [80].

Appendix C

Photographs of the Forward Spectrometer

Some photographs of the Forward Spectrometer and its subsystems are presented here.

Figure C.0.1 shows the Forward Spectrometer viewed from the upstream. Some of the collaborators of the AGS-E866 experiment are also seen. A side view of the spectrometer from the downstream is shown in Figure C.0.2. Figures C.0.3 and C.0.4 show closer looks of two of the detectors in the spectrometer, the second time projection chamber, TPC2, and the time-of-flight wall, FTOF.

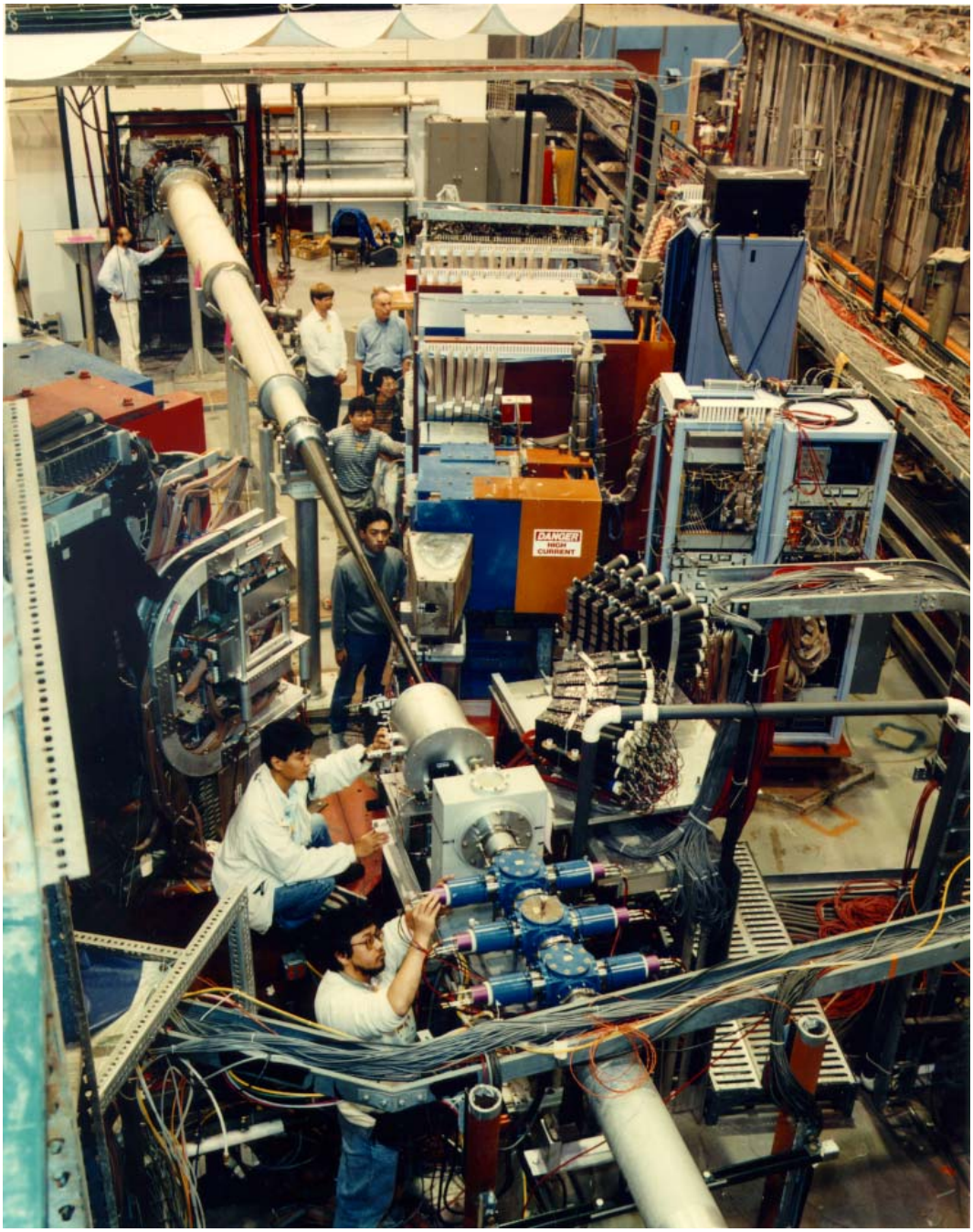

Figure C.0.1: A top view of the Forward Spectrometer, viewed from the upstream. Some of the collaborators of the AGS-E866 experiment are also seen.

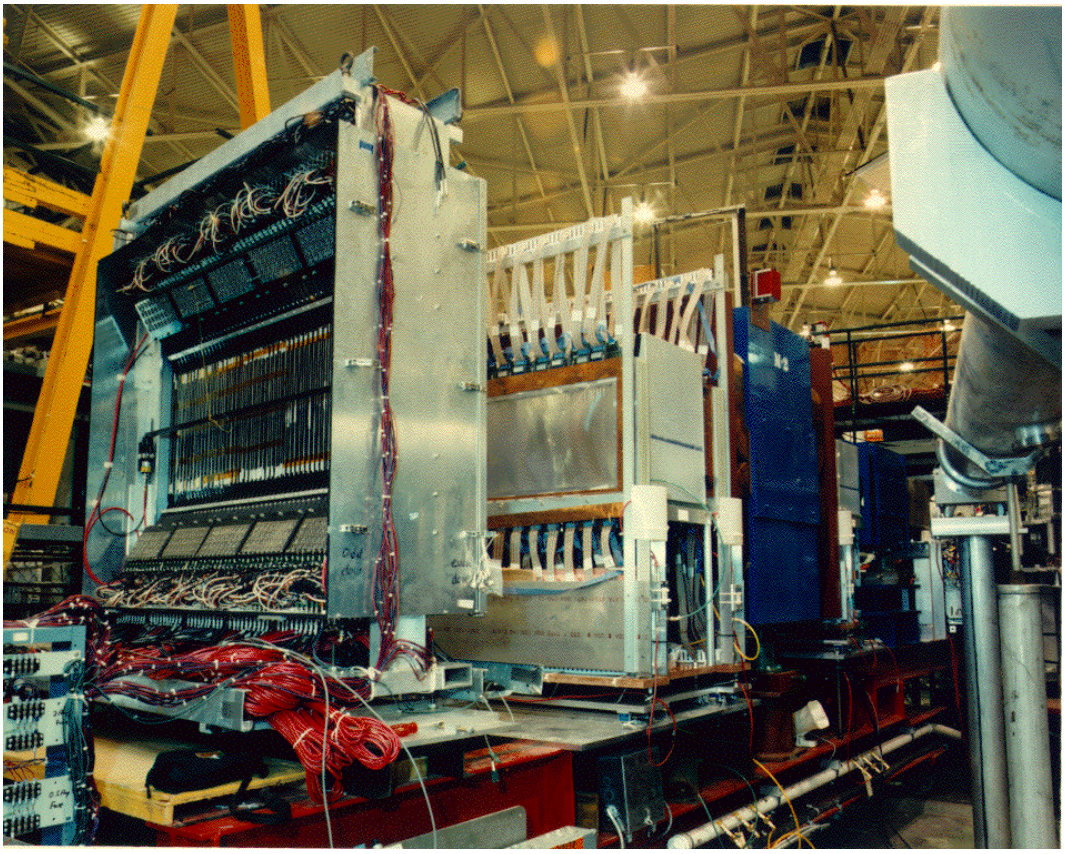

Figure C.0.2: A side view of the Forward Spectrometer, viewed from the downstream on the beam side. The time-of-flight wall (FTOF), the second tracking chamber complex (FTR2), and the analyzing magnet (FM2) are seen from the left to the right.

Figure C.0.3: A close look of the second time projection chamber, TPC2. All the tracking chambers were set on rails, and could slide out from the chamber complexes for maintenance, as seen in the photograph.

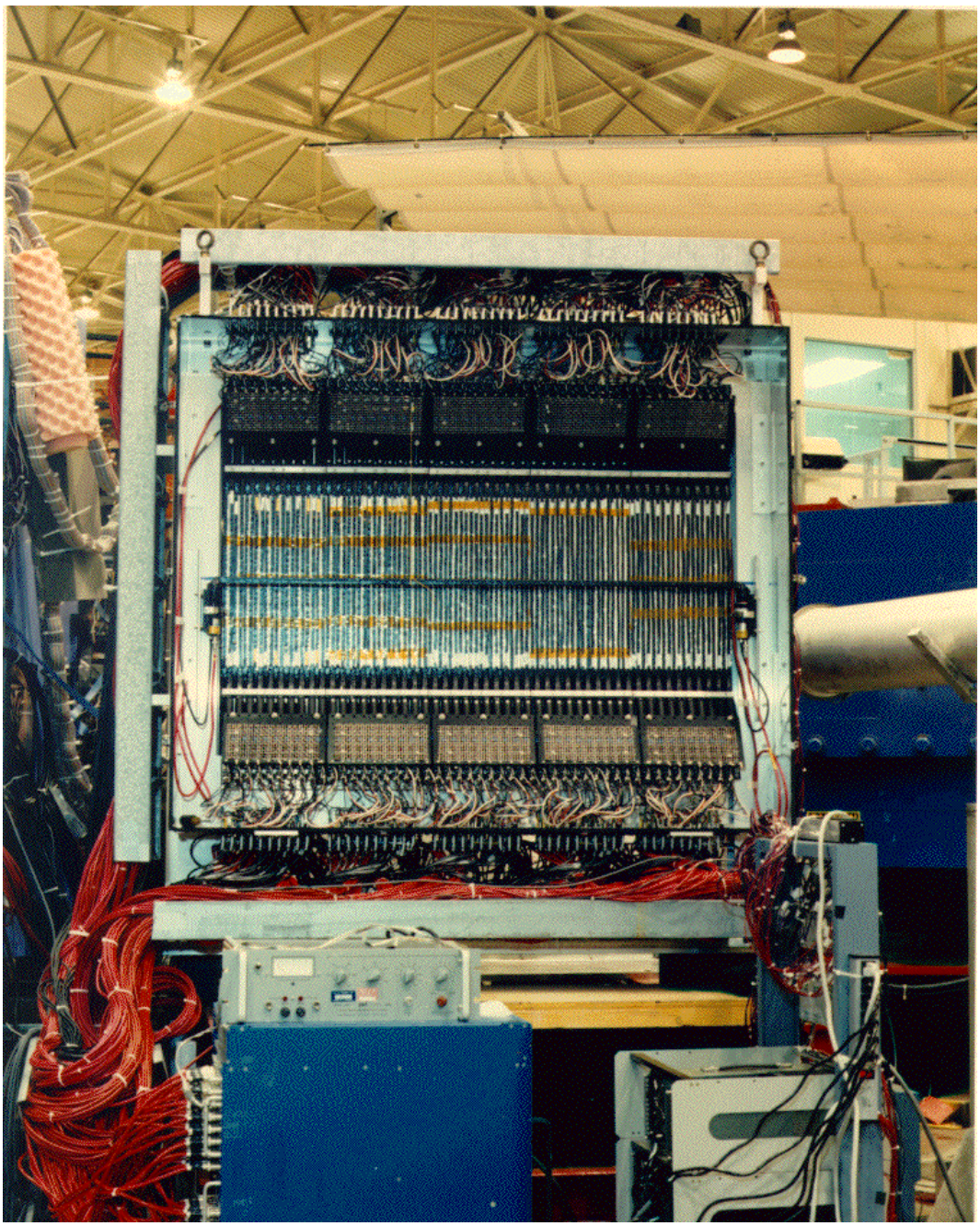

Figure C.0.4: A close look of the time-of-flight wall, FTOF, viewed from the downstream. An aluminum panel which covers the wall during its operation is removed to see the slats.

Bibliography

[1] N. H. Christ, *Nucl. Phys.* **A544** (1992) 81c.

[2] T. Hatsuda, *Nucl. Phys.* **A544** (1992) 27c.

[3] H. Satz, *Z. Phys.* **C62** (1994) 683.

[4] M. Gyulassy, *Nucl. Phys.* **A418** (1984) 59c.

[5] S. Nagamiya, *Nucl. Phys.* **A488** (1988) 3c.

[6] E802 Collaboration, T. Abbott *et al.*, *Nucl. Phys.* **A498** (1989) 67c.

[7] E802 Collaboration, T. Abbott *et al.*, *Phys. Rev. Lett.* **64** (1990) 847.

[8] E802 Collaboration, T. Abbott *et al.*, *Phys. Lett.* **B291** (1992) 341.

[9] NA35 Collaboration, J. Baechler *et al.*, *Nucl. Phys.* **A525** (1991) 221c.

[10] WA85 Collaboration, S. Abatzis *et al.*, *Phys. Lett.* **B270** (1991) 123.

[11] NA38 Collaboration, M. C. Abreu *et al.*, *Nucl. Phys.* **A498** (1989) 249c.

[12] NA35 Collaboration, J. Baechler *et al.*, *Nucl. Phys.* **A525** (1991) 327c.

[13] J. I. Kapusta *et al.*, *Nucl. Phys.* **A566** (1994) 45c.

[14] T. Hatsuda and S. H. Lee, *Phys. Rev.* **C46** (1992) R34.

[15] H. Shiomi and T. Hatsuda, *Phys. Let.* **B334** (1994) 281.

[16] NA38 Collaboration, C. Baglin *et al.*, *Phys. Lett.* **B270** (1991) 105.

[17] W. A. Zajc, *Nucl. Phys.* **A525** (1991) 315c.

[18] H. Sorge *et al.*, *Phys. Lett.* **B243** (1990) 7.

[19] S. H. Kahana *et al.*, *Proceedings of HIPAGS'93, BNL preprint* **48888** (1993).

[20] R. Mattiello *et al.*, *Phys. Rev. Lett.* **63** (1989) 1459.

[21] K. Werner, *Z. Phys.* **C42** (1989) 85.

[22] K. Werner and P. Koch, *Phys. Lett.* **B242** (1990) 251.

[23] H. Sorge *et al.*, *Z. Phys.* **C47** (1990) 629.

[24] *Conceptual Design of the Relativistic Heavy Ion Collider RHIC, BNL preprint* **51932** (1986) p.66.

[25] E802 Collaboration, T. Abbott *et al.*, *Phys. Lett.* **B271** (1991) 447.

[26] E802 Collaboration, T. Abbott *et al.*, *Phys. Rev.* **D45** (1992) 3906.

[27] E802 Collaboration, T. Abbott *et al.*, *Phys. Rev.* **C47** (1993) R1351.

[28] E802 Collaboration, T. Abbott *et al.*, *Phys. Rev.* **C50** (1994) 1024.

[29] E802 Collaboration, T. Abbott *et al.*, *Phys. Lett.* **B197** (1987) 285.

[30] E802 Collaboration, T. Abbott *et al.*, *Phys. Rev.* **C44** (1991) 1611.

[31] E802 Collaboration, T. Abbott *et al.*, *Phys. Rev.* **C45** (1992) 2933.

[32] E802 Collaboration, T. Abbott *et al.*, *Phys. Rev. Lett.* **69** (1992) 1030.

[33] E802 Collaboration, T. Abbott *et al.*, *Phys. Rev. Lett.* **70** (1993) 1393.

[34] E802 Collaboration, T. Abbott *et al.*, *Phys. Lett.* **B337** (1994) 254.

[35] E802 Collaboration, T. Abbott *et al.*, *Z. Phys.* **C38** (1988) 135.

[36] E802 Collaboration, T. Abbott *et al.*, *Nucl. Inst. and Methods* **A290** (1990) 41.

[37] C. Chasman, H. Hamagaki *et al.*, *Proposal submitted to the AGS Program Committee* (1990).

[38] E814 Collaboration, J. Barrette *et al.*, *Nucl. Phys.* **A544** (1992) 137c.

[39] H. Sorge *et al.*, *Nucl. Phys.* **A498** (1989) 567c.

[40] B. Anderson *et al.*, *Nucl. Phys.* **B281** (1987) 289.

[41] C. Chasman and P. Thieberger, *Nucl. Inst. and Methods* **B10/11** (1985) 347.

[42] T. Roser, *Proceedings of EPAC'94, BNL preprint* **49700** (1994).

[43] P. Braun-Munzinger *et al.*, *E877 Note* **1**, BNL (1994).

[44] R. Debbe, private communication.

[45] C. Chasman and H. Hamagaki, *Internal Report*, BNL (1990).

[46] K. Shigaki, *Master's thesis*, University of Tokyo (1992).

[47] P. Némethy *et al.*, *Nucl. Inst. and Methods* **212** (1983) 273.

[48] D. Friedrich *et al.*, *Nucl. Inst. and Methods* **158** (1979) 81.

[49] F. Sauli, *Z. Phys.* **C38** (1988) 339.

[50] V. Palladino and B. Sadoulet, *Nucl. Inst. and Methods* **128** (1975) 323.

[51] C. R. Gruhn *et al.*, *Proposal submitted to the CERN SPSC* **84-13** (1984).

[52] C. R. Gruhn, *Nucl. Phys.* **A461** (1987) 391c.

[53] E810 Collaboration, B. E. Bonner *et al.*, *Nucl. Phys.* **A498** (1989) 523c.

[54] T. Zimmerman, *Internal Report*, FNAL (1986).

[55] T. Fukuda *et al.*, submitted to *Nucl. Inst. and Methods.*

[56] K. Shigaki *et al.*, *E866 Memo* **5**, BNL (1992).

[57] H. Sako, *Master's thesis*, University of Tokyo (1993).

[58] A. Kumagai, *Master's thesis* (in Japanese), University of Tsukuba (1994).

[59] R. A. Scheetz and M. J. LeVine, *IEEE Trans. Nucl. Sci.* **NS-34** (1987) 1033.

[60] R. A. Scheetz and M. J. LeVine, *IEEE Trans. Nucl. Sci.* **NS-34** (1987) 1036.

[61] B. Wadsworth, *IEEE Trans. Nucl. Sci.* **NS-34** (1987) 980.

[62] G. Schultz, *Thesis*, Universitè de Strasbourg (1976).

[63] H. Sako, private communication.

[64] Particle Data Group, *Phys. Rev.* **D45** (1992).

[65] CERN Application Software Group, *CERN Program Library* **W5013** (1992).

[66] E802/866 Collaboration, H. Hamagaki *et al.*, *Nucl. Phys.* **A566** (1994) 27c.

[67] E802/866 Collaboration, M. Gonin *et al.*, *Nucl. Phys.* **A566** (1994) 601c.

[68] H. Bøggild *et al.*, *Nucl. Phys.* **B57** (1974) 77.

[69] V. Blobel *et al.*, *Nucl. Phys.* **B69** (1974) 454.

[70] M. Gonin, private communication.

[71] J. W. Cronin, *et al.*, *Phys. Rev.* **D11** (1975) 3105.

[72] S. Gavin and M. Gyulassy, *Phys. Lett.* **B214** (1988) 241.

[73] J.-P. Blaizot and J.-Y. Ollitrault, *Phys. Lett.* **B217** (1989) 392.

[74] Y. Tanaka, *Doctor thesis*, Kyushu University (1992).

[75] S. Hayashi, *Doctor thesis*, University of Tokyo (1990).

[76] P. J. Siemens and J. O. Rasmussen, *Phys. Rev. Lett.* **42** (1979) 880.

[77] K. S. Lee *et al.*, *Z. Phys.* **C48** (1990) 525.

[78] S. Hayashi *et al.*, *Phys. Rev.* **C38** (1988) 1229.

[79] Y. Kitazoe *et al.*, *Phys. Rev.* **C29** (1984) 828.

[80] Y. Pang *et al.*, *Phys. Rev. Lett.* **68** (1992) 2743.

[81] S. Fredriksson *et al.*, *Phys. Rep.* **144** (1987) 187.

[82] A. Sho and R. Longacre, *Phys. Lett.* **B218** (1989) 100.

[83] K. Werner and P. Koch, *Z. Phys.* **C47** (1990) 255.

[84] H. Sorge *et al.*, *Ann. Phys.* **192** (1989) 266.

[85] B. A. Cole, private communication.

[86] T. J. Schlagel, private communication.

[87] W. Benenson *et al.*, *Phys. Rev. Lett.* **43** (1979) 683, **44** (1980) 54 (E).

[88] J. P. Sullivan *et al.*, *Phys. Rev.* **C25** (1982) 1499.

[89] O. Hashimoto *et al.*, *Phys. Rev.* **C49** (1994) 420.

[90] E802/866 Collaboration, H. Kaneko *et al.*, contribution to Quark Matter '95 (1995).

[91] M. Hofmann *et al.*, *Nucl. Phys.* **A566** (1994) 15c.

[92] S. H. Kahana *et al.*, *Nucl. Phys.* **A566** (1994) 465c.

[93] E877 Collaboration, J. Berrette *et al.*, *Phys. Rev. Lett.* **73** (1994) 2532.

[94] V. Blobel *et al.*, *Nucl. Phys.* **B111** (1976) 397.